

Collective Swimming Dynamics of Motile Micro-Algae

Technische Universiteit Delft

Cell-Wall and Cell-Cell Interactions

K. Muller

Collective Swimming Dynamics of Motile Micro-Algae

Cell-Wall and Cell-Cell Interactions

by

K. Muller

to obtain the degree of Master of Science
at the Delft University of Technology,
to be defended publicly on Monday 14th November, 2016 at 14:00 hours
P&E number 2793

Student number:	4021177
Project duration:	January 14, 2016 – November 14, 2016
Thesis committee:	Prof. Dr. ir. J. Westerweel, TU Delft Prof. Dr. ir. W. vd Water, TU Eindhoven Dr. ir. D. Tam, TU Delft Dr. ir. B. Eral, TU Delft Dr. ir. A. Sciacchitano, TU Delft

An electronic version of this thesis is available at <http://repository.tudelft.nl/>.

Acknowledgments

When I started this masters project, I remember having only a blackbox in front of me that would connect multiple cameras. Now, 10 months later, I will continue to remember this kick-off as very illustrative to the hands on approach that was needed during this work, as I have enjoyed to great extent. However I could not have completed this work to its current state without the help of the following people. I would like thank Edwin Overmars for much help and accommodation to build the experimental setup, as well as giving fruitful advise how to improve and tweak its performance. As well I am very grateful to both Greta Quaranta and Da Wei for supplying the many carefully conditioned cell cultures to perform experiments on. For all the help of the preparations of many flow-chambers, and as well their careful surface treatment, I would like to thank Roland Kieffer. I would like to thank Franka Veltman for helping me understand different the concepts of the optimization methods as used in this thesis, and Lex te Loo who proposed to help me with the cover design of this thesis. It is without question that I am very grateful to my family and friends for support during my work.

At last but not least I would like to thank Daniel Tam for proposing and supervising this master project on the study of many tiny collective swimming micro-algae, and giving much freedom with good tips and careful advise to keep direction during this work.

K. Muller
Delft, November 2016

Summary

Collective behavior is abundant in nature, from flocks of birds down to the coherent motion of microbes. At the small scale, microbes such as algae swim at low Reynolds number $Re \sim \mathcal{O}(10^{-3})$, that is in an environment dominated by viscosity. Due the highly viscous environment the hydrodynamic forces imposed by the organism span over relative long range, therefore the collective behavior of microbes is with increasing interest to the fluid mechanics community. Understanding how microbes interact with different environments and each other has much relevance new lab-on chip applications, bio-film formation, and promising value to emergent microfluidic technologies.

This thesis is an experimental study that focuses on the motile algae *C. reinhardtii* that is of length scale of $l_b = 10[\mu\text{m}]$ and propels its body by beating two flagella. We track multiple of these microorganisms in 3 dimensions for sufficient long times using a 4 camera system to study their motility in an unconfined geometry of size $l \sim 1[\text{mm}]$. Based on imposed flow signature imposed by the algae there is interest two strains, the wild-type (cc125) that pulls it surrounding fluid in, and a mutant (mbo-1) with reverse swimming gait that pushes fluid out. The main goal of this thesis study the detailed motion and interaction of cells with planar physical boundaries as well as with each other. To do this we study the motility of individual cells at varying density in relative dilute regime, with as well interest to possible phase transition of the cell suspension as a collective system.

To track the position of the algae as physical object in the fluid domain we use recent advances in the literature on the tracking of birds and insects, rather than performing a full tomographic reconstruction from the camera plane by the commercial software LAVISION DAVIS. Using a integer optimization technique (ILP) we match different paths of the particle images among the camera planes by a recursive divide and conquer strategy in MATLAB to reconstruct trajectories made by the algae. We justify the performance of the experimental reconstruction towards the Pareto frontier, and quantify the algorithm of the tracking towards the available resources in the different camera planes. After having reconstructed the time positional information in the object domain, we study the motion of the microorganisms by the dynamics along their trajectories using the Frenet-Serret framework.

In our results we find unexpected behavior of the wild-type (cc125) algae mostly swimming up and down the fluid domain. In case of the mutant (mbo-1) cells we find they mostly crowd the surface, which they remain immobile and therefore of less interest. For the motile wild-type algae we find a non-uniform concentration profile over the height of the domain, which a significant portion remains at the boundary. For the algae that freely explore the bulk we find that they move along helical trajectories with a tendency to left-handed chirality. For the algae that are motile at the surface the majority is found to circle clockwise over the surface. Based on the concentration profile over the height of the domain, we define a boundary region that extends up to $l_b = 100[\mu\text{m}]$. In this region we find that most algae touch the boundary and swim either co-planar to the boundary or reflect of the boundary. For the reflecting cells there is strong correspondence between in incident and outgoing orientation of the cell along its trajectory with respect to the boundary. The cell-cell interaction have a much wider range of complex behavior, due the high degrees of freedom as the cell are freely suspended in the bulk. Therefore we only touch upon the complexity of these events in light of the cell-wall interactions. We find that the algae do not significantly reorient when coming close together as they tend to conserve their relative angle along the trajectories. This is not necessarily a trivial consequence of cells ignoring each other as they can perform complex motion during these events.

We discuss the dynamics that are obtained towards the current literature. Our method is unique in the sense that the 4 camera system allows higher cell densities in the fluid domain than many single camera methods. We find that our study to sheds new light on the boundary action in comparison to studies in the confined geometry. We conclude that we can explain the up and down swimming in the domain by the boundary action as a fixed point operation due the geometric aspect ratio of the flow domain. For the cell-cell interaction we conclude that we have not yet studied the right metric to study their complexity in detail. We end this thesis with recommendation for further for improvement of the developed algorithm as well as for the carried out experiments. Further we propose that future work should include different unconfined flow geometries as an engineering outlook. At last it would be very interesting to study the algae suspended in visco-elastic fluids widely found in biology, whereas they remain largely unexplored in experiments.

Contents

1	Introduction	1
1.1	Literature Review	2
2	Methodology	5
2.1	Flow Chamber and Cell Cultures	5
2.2	Experimental Setup	6
2.2.1	Calibration.	7
2.2.2	Lighting Conditions	7
2.3	Image Processing	7
2.3.1	Image Filtering.	8
2.3.2	Particle Image Midpoint Finding Routine	8
2.4	3D Lagrangian Particle Tracking Algorithm.	9
2.4.1	2D Particle Tracking Algorithm.	10
2.4.2	Track Matching Algorithm	10
2.4.3	Divide and Conquer Algorithm	13
2.4.4	Triangulation	14
2.5	Post Processing	14
2.5.1	Curve Fitting.	15
2.5.2	Bounding Domain	15
2.5.3	Trajectory Kinematics	15
2.6	Algorithm Performance and Synthetic Data Validation.	16
2.6.1	Synthetic Data	17
2.6.2	Experimental Data	18
3	Results	21
3.1	Experimental Reconstruction in the Eulerian Reference Frame	21
3.2	Swimming Kinematics in the Lagrangian Frame	24
3.3	Cell-Wall Interactions	26
3.3.1	Wall-Bound	28
3.3.2	Reflection	28
3.4	Cell-Cell Interactions	31
4	Discussion	35
4.1	Individual Swimming Dynamics	35
4.2	Cell-Wall Interactions	36
4.3	Cell-Cell Events	39
5	Conclusions	41
6	Outlook and Recommendations	43
A	Stokesian Background Flow	45
B	Triangulation of the Mutant Experiments	47
C	Complex Cell-Cell Interactions	49
	Bibliography	51

Introduction

In his letter to the Philosophical Transactions of the Royal Society of London in 1676, Antoni Leewenhoeck [53] first reported the existence of small "dierkens" or animalcules swimming in the canals of Delft using his first invented microscope. Nowadays such animalcules are called microorganisms and vary in length scale from 1 to 100 microns of which many are motile and propelled by flagella and cilia. These microorganisms include bacteria [50], algae [35], spermatozoa [32], plankton [37], which move around to explore their environment by imposing stress to the surrounding fluid [51]. Due their smallness microbes swim at low-Reynolds number, i.e. $Re \sim \mathcal{O}(10^{-3})$. Here the Reynolds number is defined as $Re = \rho U l / \mu$, with U and l the velocity and length-scale of the organism, and ρ and μ the density and dynamic viscosity of the fluid. Since Reynolds number is very small ($Re \ll 1$) microorganisms swim in an environment dominated by viscosity. Life at low-Reynolds number yields a very different physical intuition than common fluid mechanics. In the seminal work by E.M. Purcell [71] "one would best picture to cit as being stuck in a basing of molasses". In absence of inertia the hydrodynamics are governed by the time reversal Stokes equations. As consequence microbes can only propel by non-reciprocal shape transition, with an overall swimming gait being force and torque free. Such non-reciprocal deformations of microorganisms as mechanism of propulsion where first recognized by G.I.Taylor [83] who described the action of a waving sheet and J.Lighthill [58] who discussed the squirming of spherical body and later the role of flagella and cilia [57]. Despite the time dependent geometric deformation of micro-swimmers [75, 76], the relative far-field flow of fluid can be simplified to a characteristic flow either pulling or pushing on the fluid with a velocities that decays as $\sim 1/r^2$, with r the radial coordinate away from the organism. Force and torque free, microorganisms do impose an active stress to the fluid with forces associated to the fluid flow that span relative long range. Therefore, within the fluid mechanics community, there is increasing interest in how microorganisms influence the motion of each other, and how they interact with physical boundaries.

Suspensions of living organisms display a rich set of self-organized collective behavior, which the motion of many organisms is correlated over length-scales much larger than the organism itself, including the formation complex vortex states [19, 60, 74, 90], with features found at many scales [85]. On the mesoscopic scale, i.e. the scale between the microscopic size and macroscopic environment, such active suspensions or living fluids [47, 73] have attracted high levels of interest and form a new class of multiphase flows and complex fluids. Contrary to what would be expected in the viscous Stokes regime, active suspensions of *E. Coli* have been reported to break down in vortical structures [30, 88], reminiscent of large scale turbulence in the inertial regime. There is much interest how to understand such critical phase transitions in large assemblies of microorganisms as active particles [86]. This new class of active materials raises new questions : can one manipulate such active fluids with control parameters such as the type of swimmer (pusher vs. puller), the cell density, and the surrounding geometry. The role of active fluids has promising value to emergent microfluidic technologies, e.g. phase sorting and navigation [20, 23, 31, 33, 67], enhanced tracer diffusion [42, 55], novel means of micro-scale transport [21, 45, 77], artificial propulsion [29, 81], the problem of microfluidic mixing [78] as well as new insight to bio-film formation [68].

The aim of this master thesis is to experimentally study the motility of the green algae *Chlamydomonas reinhardtii* of characteristic length scale $l = 10[\mu\text{m}]$ as a model micro-swimmer [1, 35]. In particular there is interest to characterize how the motile algae interact with physical boundaries such as walls, and how the algae interact with each other in an unconfined geometry (≥ 100 body-lengths). These areas remain largely

unanswered in the literature. Additionally there is interest how the cells collectively swim at varying cell density, and whether the suspension undergoes critical phase transition from incoherent to coherent motion. Two different phenotypes are studied, the wildtype (cc125) which pulls on the fluid, and its backward swimming mutant (mbo-1) which pushes the fluid out. We study the algae by 3D micro particle tracking methods using a 4 camera system. We study algae suspension of increasing cell density up to a point which a full tomographic reconstruction would be needed, which is beyond the scope of this work. The structure of this thesis is twofold. First we introduce the methodology developed in this thesis to reconstruct the 3 dimensional trajectories made by individual algae in chapter 2. Secondly, starting from the results in chapter 3 we focus for most part on the physics of the freely swimming cells, which are discussed towards the current literature in chapter 4. We end this thesis to summarize our main conclusions in chapter 5 and present outlook and recommendation for future work in chapter 6. Any supplementary information can be found in the appendices.

1.1. Literature Review

Algae are dual-flagellated microorganisms that belong to the unicellular eukaryote. Algae are autotrophic micro-organisms that harvest energy from inorganic material by performing photosynthesis. Algae adjust their motility to control their trajectories in search of light to gradients in light intensity, formally known as phototaxis [1]. As motile microorganisms beat their flagella at frequency $f = 60[\text{Hz}]$ to exploit the environment, they create substantial flow. From low-Reynolds number hydrodynamics, the time averaged flow field around *C. reinhardtii* can be understood in term of a three-component assembly of singularity solutions to the Stokes equations and classified as a puller [27]. In the near field on the other hand the flow is highly time dependent [36], and can oscillate between a puller and pusher type flow signature [46].

In the analysis of single trajectories the algae do not swim along straight lines as they constantly revolve around and reorient their longitudinal axis which results in spiraling trajectories, a common feature among many microorganisms. A first mathematical treatment of this motion of trajectories of microorganisms was discussed by Crenshaw [13] using the Frenet-Serret differential geometry of curves. This methodology [13, 15] was further used in subsequent studies including algae [14, 16–18], which the resulting trajectories of the organism was found to be influenced by external stimuli of light. Recently this framework has been used to characterize the swimming dynamics of the like-wise dual flagellated micro-swimmer *P. minimum* (dinoflagellate) by Lee et al. [52]. In their work they followed several organisms for long times in the bulk and as well near boundaries, and found increased speed near the boundary that could be well explained of hydrodynamic cause [51]. Like with the presence of a boundary, algae as well have been reported to respond the shear flow in of the suspending fluid [9], which they align along the vorticity vector. Such response to surrounding fluid of the organism has as well been reported in the presence of another organisms, as it has been reported that the flagella synchronize true the hydrodynamics [8], which could lead to non-trivial hydrodynamic interactions between freely suspended cells.

Bacteria are widely known to get attracted to, and circle clockwise above solid boundaries. The clockwise circling can be well explained by a hydrodynamic force balance between the head and tail [48], whereas the attraction is thought to be dominated hydrodynamics mediated by collision with the wall [7, 56]. Such boundary interaction can yield subtle differences as for example bacteria swim counterclockwise near free fluid interfaces [22, 54]. In a quasi 2D geometry Kantsler et al. [43] studied near field interactions of wild-type algae (cc125) and mutant backward swimming phenotype (mbo-1) cells with solid walls. The wild-type cells were found to be able to bounce off solid boundaries with loss of information of approach, whereas the mutant cells hardly escaped the solid boundary. A recent study by Contino et al. [11] show that wild-type algae scatter off small pillars due combination of contact and hydrodynamic lubrication forces. However these experiments have been carried out in Hele-Shaw cells of two closely packed plates at separation length δ of $\delta = 25[\mu\text{m}]$, i.e. at size of the organism including its flagella. In comparison much richer boundary interactions have been reported for the larger ciliated *Volvox* ($l = 300[\mu\text{m}]$) in the unconfined geometry [26], with existence of hydro-dynamically bound states as waltzing limit-cycles.

Critical phase transitions in collective behavior of microorganisms remain largely unexplained, and a complete description of the interactions between individual organisms is of wide interest. Ishikawa et al. [41] conducted extensive numerical and analytic study on the hydrodynamic interaction between two spherical squirmers with imposed tangential velocity along the cell surface. Based on the computational results they conclude that the cells first attract each other, then reorient dramatically when withing near reach, and depart again. To verify the results of the imposed tangential surface velocity profile along the surface, another paper by Ishikawa and Hota [40] compared two interacting paramecia of ellipsoidal shape at length-scale

of $l \sim 200[\mu\text{m}]$ with their numerical method, with much agreement and verified their model is accurate. However due experimental reasons they limit their study to a quasi 2D Hele-Shaw cell at separation distance $\delta = 70[\mu\text{m}]$, whereas in the first paper [41] they conclude that 2D restriction can lead to misleading results by over simplification. Despite the possible over simplification, two theoretical studies by Alexander et al. [3], Pooley et al. [70] focus on plane dynamics of two interacting three-link swimmers modelled as 3 dimensional bodies. Based on shape transition of three-link swimmer, they find that certain types of swimming yield a conservation of relative angle of approach and departure. However the results on the three-link swimmers are hard to generalize to physical microorganisms, which have much more advanced swimming gaits. Another rigorous analytic treatment on long-time hydrodynamic interactions was presented by Michelin and Lauga [62] for pushers and pullers, which investigated the long time hydrodynamics of two orbiting organisms. A recent study by Drescher et al. [28] addressed the mechanisms of inter-cellular interactions and boundary action for much smaller E-Coli ($l \sim 2[\mu\text{m}]$). They conclude that the hydrodynamic domain of interaction extends up to two body-length where after it is destroyed by Brownian noise and thermal fluctuation. In case of algae Brownian motion is not expected to play a large role due its larger size $l = 10[\mu\text{m}]$, which mechanisms of hydrodynamic interactions remain largely unknown.

Tracking of motile microorganisms in 3D was first conducted by Berg [6] on single 1 micron E-coli. Many 3D microscopic imaging methods have been developed later. Several single camera methods have been used such as total internal reflection microscopy [87], defocussing microscopy [93, 94], single camera holography [38, 39, 63], scanning microscopy [12], lens free on chip holography [79], phase contrast microscopy [10, 82]. As single camera methods are problematic at increasing density due occlusions, only few studies have used a stereoscopic 2 camera system [5, 25, 84] to track micro-organisms in 3 dimensions. In this work we make use of a 4 camera system to track and reconstruct the position of motile algae in a 3D object for long times using Lagrangian particle tracking (LPT). LPT has long been of interest to the fluid dynamics community to study tracers dynamics [61, 65, 89], and is as well referred to as 3D particle tracking velocimetry (3D-PTV). The idea of this method is to identify particle image midpoints in the individual camera planes and then triangulate and track the position in a calibrated object domain. At the heart of this method lies consistent tracking and matching of particle images in different camera planes, which the consistent matching [61] is often seen as the most difficult part. To integrate the matching with the time tracking of the object position many approaches have been proposed, such as genetic algorithms [24], neural networks [34], self organized maps [64] and ant colony optimization [66]. In a study of tracking bats, Wu et al. [95] first put to question whether it is better to first track multiple positions in the individual camera plane and then match the trajectories among the different camera's, or first match multiple particle images among the camera planes and then track the particles as triangulated objects. In this study it was found that first finding trajectories of particle images in the different camera planes is more robust to ambiguities in the stereoscopic matching. The method of Wu et al. [95] solves a combinatoric problem of candidate matches of camera tracks formulating it as a discrete optimization problem. This discrete optimization is then efficiently solved using integer linear programming (ILP) to certain constraints that grant a unique reconstruction of the object position. Their method was further improved in [96, 97] relaxing some of the constraints to deal occlusions in the camera plane, with similar techniques proposed by [59, 91, 92, 98] on fruit flies. The most recent advances on LPT have been made by Attanasi et al. [4] on the tracking of birds and insects. In their work they reduce the computational complexity of the combinatoric problem by an efficient recursive divide and conquer strategy. As well do they evaluate the performance of their algorithm by use of the Pareto frontier in the "number of objects vs. tracked number of frames"-plane to quantify the efficiency of the algorithm to the available resources in the different camera planes.

2

Methodology

To simultaneously track multiple microorganisms freely swimming three dimensional fluid domain, we adopted the experimental setup previously developed to perform flow measurements in a thin immersion droplet [44]. In this study [44] the fluid was seeded with passive tracers particles and flow velocities were measured using tomographic micro particle image velocimetry (μ PIV). In this study we track algae swimming in a suspension as active moving particles to do this we developed a Lagrangian particle tracking (LPT) algorithm inspired by recent work of Attanasi et al. [4] on birds and insects, that makes use of integer linear programming (ILP). Our method is implemented in MATLAB, several reasons motivated the decision to develop our own tracking algorithm rather than using available commercial imaging software LAVISION DAVIS. First the available particle tracking velocimetry (PTV) license in DAVIS aims to combine PIV with PTV to reconstruct an instantaneous velocity field, and does not guarantee tracking for long times which is the objective here. Secondly, here we explore cell concentrations starting with the dilute regime, which implies extending recording times to gather the required experimental data. In case of long recording times available license for tomographic reconstruction would require unrealistic amount of 3D image files, of which most data would be trashed.

2.1. Flow Chamber and Cell Cultures

We conduct experiments on the green algae *C. reinhardtii*. This microorganism has a cell body of size $l_b = 10[\mu\text{m}]$ and swims by beating two flagella of as well $l_f \sim 10[\mu\text{m}]$ and is slightly bottom heavy [1]. We have special interest in the wildtype (cc125) (Figure 2.1a) which pulls fluid inward, and its mutant backward swimming phenotype (mbo-1) (Figure 2.1b), which pushes fluid out by a reversed flagella stroke. All cell cultures used for experiments have been carefully grown and counted following well established methods (see for example Quaranta et al. [72]). To conduct experiments the cell suspensions are diluted to the desired concentration in the buffer Tris-hydroxymethyl-aminomethane (Tris). The algae solution is then loaded into a flow chamber (Figure 2.1c) using an extra wide pipette to minimize any de-flagellation. The flow chambers are made of 1.5[mm] thick laser-cutted acrylic sheet with outer dimensions of $26 \times 76[\text{mm}]$ and a 15[mm] diameter center hole as the reservoir for the cell-suspensions. The bottom surface of the flow chamber is sealed by a 0.1[mm] thick glued Danzig Dekglazer glassware of $20 \times 40[\text{mm}]$, and once the cells are loaded into they are covered with the same glassware on top, held by capillary forces. To prevent the cells from sticking/adhering to the flow chamber its exposed surface, the flow chambers are treated with a protein solution of 1[mg] bovine serum albumin (BSA) (Aldrich A7906-50G) and 1[mg] premixed salts PBS (in lab-stock) at 100[ml], based on the saturation of the contact line [80]. After the mixture is prepared, the glassware is cleaned for 25 minutes in an ultrasonic chamber with a surfactant solution (Hellmanex III 0.5 [vol.%]), rinsed $5 \times$ with DI-water, again put in the ultrasonic with DI-water only and as well rinsed $5 \times$ with DI-water. The laser cut acrylic sheet is only cleaned $5 \times$ with ethanol and rinsed with DI-water, since the exposed surface is much less and out of field of view in the experiment. Both the glassware and acrylics are dried with pressurized dry-air to remove the cleaning liquids. After cleaning the bottom glassware is glued to the flow chambers using Norland optical adhesive 81 with 4 minutes UV curing. Once the flow chambers are assembled, both the flow chamber and the cleaned cover glassware are put into an oxygen-plasma for 30 seconds to charge and further clean the surface such that the BSA-PBS solution will adhere to the surface. The BSA-PBS solution and cleaned flow-chamber

and glass covers are put into contact for 1 hour, where after they are rinsed with DI-water and cleaned with pressurized dry-air. When the flow chamber is filled with a specific suspension an additional 30 minutes is waited before experiments are conducted to make sure that the algae have regrown most of their flagella, and are well adjusted to the environment of the flow chamber.

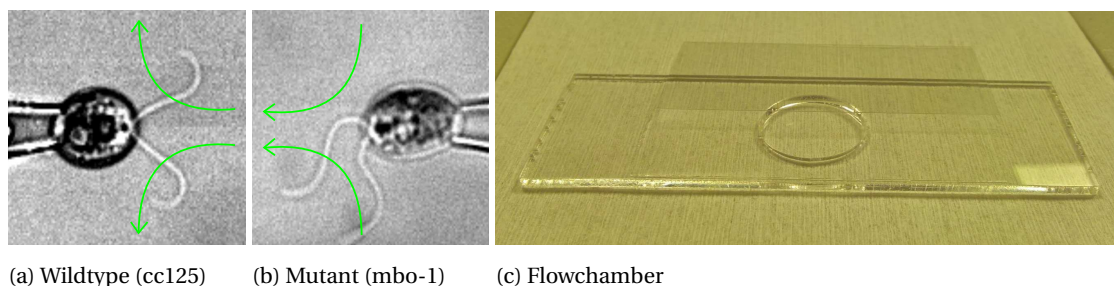


Figure 2.1: Materials as used. a) Wildtype algae (cc125), with a swimming stroke that pulls fluid in. b) Mutant backward swimming phenotype (mbo-1), that pushes fluid out. (Courtesy of Greta Quaranta) c) Fully functional flow-chamber before cells are supplied.

2.2. Experimental Setup

The experimental setup in Figure 2.2b consist of 4 CCD camera's (LAVISION IMAGER PRO 4M) imaging at 15.4[fps]. Using the depth of field, each camera films an projected object volume, which can be used for stereoscopic reconstruction as in Figure 2.2a. A LAVISION WINDOWS XP machine with a DAVIS 7.2 acquisition system to trigger and read the camera's. The recording time t_{rec} for the based suspension was set to 1000 frames, i.e. $t_{rec} \sim 60[s]$, and was doubled when the cells density was halved up to 8000 frames, i.e. $t_{rec} \sim 8[min]$. To position the flow chamber in the object volume, a tens micron precision x, y, z stage is mounted on top of the setup (see Figure 2.2b).

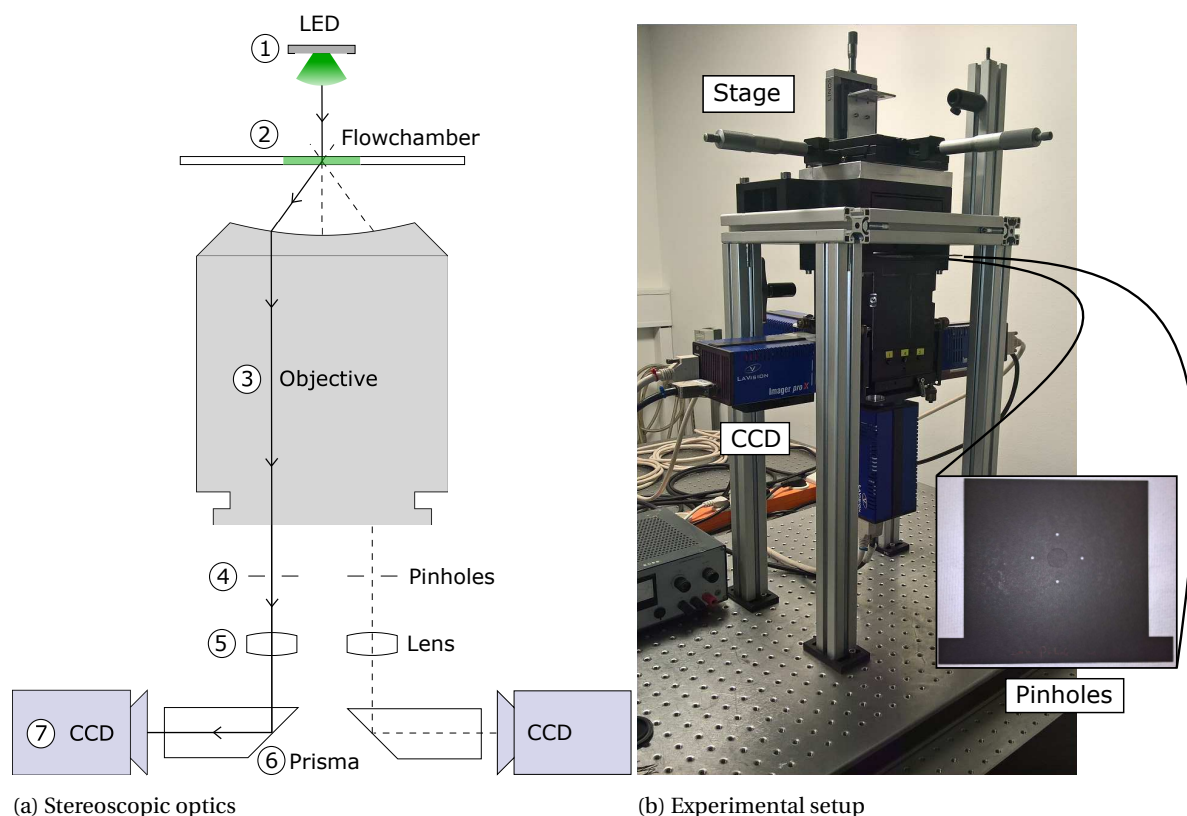


Figure 2.2: Experimental setup. a) Stereoscopic representation of the optical path, (1) LED source, (2) positioned flow-chamber, (3) objective, (4) pinhole, (5) lens (6) prisma, (7) CCD camera. b) Physical setup, with pinhole card as inset.

All camera's have a likewise train of optics. From the top we flash a LED panel to illuminate flow domain which the algae which scatter the light forward (more details in subsection 2.2.2). The forward scattered light enter a lens objective that combines all camera's in one point under an absolute angle of 10° , with a magnification of $M = 1.5$. Passing the objective the light rays cross a pinhole and lens system. Here the depth of field is increased by a laser-cutted pinhole card (inset Figure 2.2b) with respect to the original configuration [44]. The pinhole card shrinks the original pinhole diameter $d_o = 7[\text{mm}]$ to $d_p = 2[\text{mm}]$. Using a scaling derived from [44] for the depth of field $z_o \propto d^{-2}$, we successfully increase the depth of field by $(d_o/d_p)^2 \sim \mathcal{O}(10\times)$, and extend its experimental value of $200[\mu\text{m}]$ to a depth of field of $2[\text{mm}]$, as consistently found in the experiments. At last, with exclusion of the upward positioned camera (bottom Figure 2.2b), the optical path is deflected 90° to the side by a mirror prism into the CCD camera's.

2.2.1. Calibration

To relate the coordinates of a physical object $\mathbf{x}_o = [x, y, z]^T \in \mathbb{R}^3$ to the camera planes $\mathbf{x}_m = [x, y]^T \in \mathbb{R}^2$ including any magnification and optical distortion, a calibration procedure is carried out. Using the installed stage (Figure 2.3a) we place a LAVISION MP 100 $[\mu\text{m}]$ flat calibration grid (Figure 2.3b) at position of the flow chamber holder. First all camera's are made co-planar imaging the calibration without pinhole card, using the narrow depth of field this allows to reduce the Scheimflug effect by mechanically adjusting the orientation of each camera [2]. Then the CCD chip is trimmed to a section of approximately $400 \times 400[\text{px}]$ with the calibration grid centered, representing approximately a $2 \times 2[\text{mm}]$ centered plane. Installing the pinhole card the calibration grid is imposed at 21 planes spaced $100[\mu\text{m}]$ apart to impose a $100[\mu\text{m}^3]$ cubic grid along the height of the domain z . The bounding box to the object domain under these setting is $2 \times 2 \times 2[\text{mm}]$, with a significant cut-off along the sides of object domain as the CCD cameras are oriented under a 10° absolute angle (see Figure 2.5a). Having carried out the calibration, we fit an analytic calibration mapping $\mathbf{x}_m = \mathbf{f}_m^{\text{cal}}(\mathbf{x}_o)$ that maps the physical object space to the camera image plane $\mathbf{f}^{\text{cal}} : \mathbb{R}^3 \rightarrow \mathbb{R}^2$. First we use the commercial software DAVIS to construct a 3rd order polynomial mapping [2] in each x, y object plane imposing the calibration target at fixed height z , then the coefficient returned by DAVIS are fit in the object domain height z using a 2nd order polynomial in MATLAB.

$$\begin{aligned} \mathbf{f}^{\text{cal}}(\mathbf{x}_o) \equiv & \mathbf{c}_0(z) + \mathbf{c}_1(z)x + \mathbf{c}_2(z)y \\ & + \mathbf{c}_3(z)xy + \mathbf{c}_4(z)x^2 + \mathbf{c}_5(z)y^2 \\ & + \mathbf{c}_6(z)x^2y + \mathbf{c}_7(z)y^2x + \mathbf{c}_8(z)x^3 + \mathbf{c}_9(z)y^3 \end{aligned}$$

The calibration procedure has been carried out before and after a set of experiments, such that any mechanical misalignment during the experiments can be compensated for.

2.2.2. Lighting Conditions

The algae are illuminated by a green LED panel at wavelength of $\lambda = 527[\text{nm}]$ flashed from the top using a DC source @ $3.5[\text{V}]$ and $1[\text{A}]$. All experiments have been carried out at room temperature $T \sim 25^\circ\text{C}$ and at moderate light intensity of $I \leq 200[\mu\text{mol}/\text{m}^2\text{s}]$ with no measurable light intensity gradient. Under these setting no photo-taxis or bleaching of the cells has been reported to take place [1]. The light of the LED is scattered forward into the direction of the camera by the algae (Mie scattering) and the cells appear as bright spots or particles on the CCD chip Figure 2.4a. To reduce the background light produced by the LED, the flow chamber is masked by a punched black card installed below (Figure 2.3c) and above the flow chamber (Figure 2.3c). During experiments the camera's where triggered at a frame rate of $15.4[\text{fps}]$ with an exposure time of $t_{\text{exp}} = 10^4[\mu\text{s}]$.

2.3. Image Processing

The raw DAVIS .im7 image files (Figure 2.4a from the multiple camera planes delivered by the acquisition system are read into MATLAB using the LAVISION code `readimx.m`). Starting with the raw image in the camera plane the algae appear as bright spots up to diameter $d \sim 5[\text{px}]$. In the upcoming sections we will refer to the algae as particles, and their scattered light that appear as bright spots in the camera plane as particle images. Using image processing tools we wish to find the midpoints of the particle images by estimating the location of their local midpoints. There are several experimental artifacts that need to be eliminated to find the correct particle image midpoint. These artifacts include pixel noise, image background, and blinking of the particle images, i.e. intensity level of the particle images is not constant in time. The particle image blinking is likely

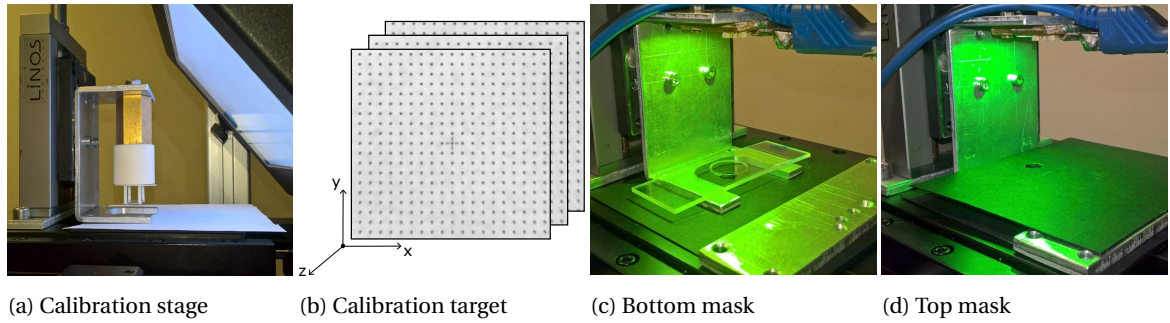


Figure 2.3: Calibration and stage. a) Calibration stage with installed target. b) Calibration target in camera plane in several planes along the domain height z . c) Flow chamber with bottom mask and LED illumination installed. d) Addition of the top mask before conducting experiments.

due the rotation of the algae, it is possible that certain organelles scatter more light than others and that the periodic rotation of the cell results in periodic variation of the light intensity. Our image processing algorithm extract the midpoint positions from the individual camera planes by loading in a time sliding queue of image frames for each individual camera over prescribed time span. Using multiple time frames in the queue for each separate camera in time, we hope to cope with the experimental artifact taking into account for time varying information of the particle images in the camera planes. We make extensive use of the mean $\mu(\bullet)$ and standard deviation $\sigma(\bullet)$ of the light intensity levels from the image files in the time sliding queue to define threshold and segmentation levels with user defined weights that can be tweaked to process the image files for each experiment separately.

2.3.1. Image Filtering

First, to suppress pixel noise in the image, a linear Gaussian convolution is performed in the camera plane by `imgaussfilt.m`, with the width of the Gaussian matched to the expected particle shape. This filter can both be thought of as a weighted noise filter, or as a particle shape detection by convolution of a predefined shape with the image. A second artifact that needs to be removed is that the particle images appear to blink in time. To suppress this blinking a nonlinear Min-Max filter is implemented, to correct the large contrast variation of the particle images in time. Here we use a modified version of `pwMinMax.m` from the PIVware toolbox by the group of J. Westerweel. Instead of locally windowing the minimum and maximum of the image using `ordfilt2.m`, we use optimized routines for the grayscale dilation (`imdilate.m`) and erosion (`imerode.m`) with identical prescribed input and results, however with reduced computational cost. As well slight improvement is achieved as the gray scale dilation and erosion allow to prescribe a circular window / neighborhood (`getnhood.m` & `strel.m`), which is fit slightly larger to the particle diameter at $d = 7[\text{px}]$, and better captures its shape. An example of a filtered image in the camera plane can be found in Figure 2.4b. In all image processing routines we have used symmetric image borders to reduce the domain of boundary influence, which the reduced boundary influence is masked out in the final filtered image.

2.3.2. Particle Image Midpoint Finding Routine

First, as can be recognize by careful inspection of Figure 2.4b, a small portion of the particle images are not corrected in contrast by the min-max filter and remain in the background as less bright grey spots. As these particle images can reappear in later image frames we designed a procedure that tries to include a portion of the particle images that remain in the background. First we count the particle images that appear bright enough to be detected by assigning a segmentation level to the MATLAB local maxima finder of the computer vision toolbox by `step.m` in combination with `vision.LocalMaximaFinder`. This combination of MATLAB routines deals well with partially overlapping particle images, by searching for local intensity value maxima in the image. By estimating the number of particle images in each camera frame we use to image queue to as well find the variation of that number in time. Then to include the particles that remained in the background, we impose an expected number of particle images to find in the camera plane including the variation in time by the previous step, and return this to the `vision.LocalMaximaFinder` routine. Doing so we hope to count as well the particle images that where blinking and remained in the background as grey spots. The found particle image maxima are stored as a binary map which we thicken to a binary mask using `bwmorph.m`, this operation conserves the number of particles as it allows no overlap. An example of the binary mask

can be found in Figure 2.4c. We then introduce this mask together with the raw images from the camera to `regionprops.m` to estimate the particle image midpoints based on a intensity value weighted midpoint as marked in Figure 2.4d. The particle image midpoint are then stored in some list.

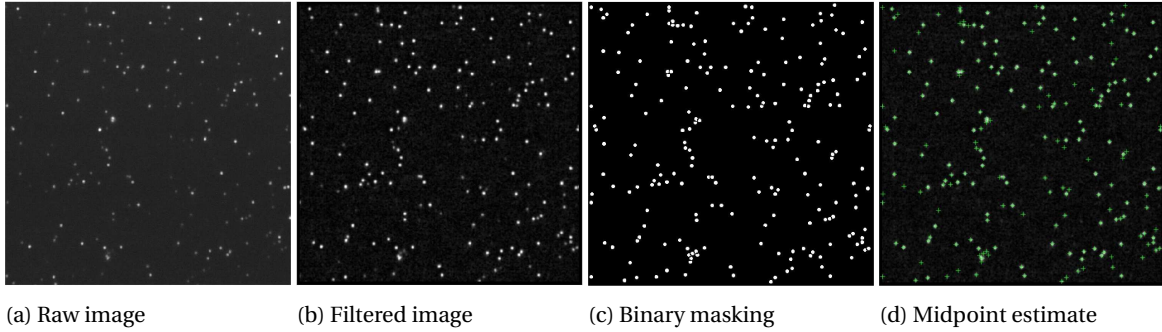


Figure 2.4: Consecutive image processing. a) Raw image from the camera plane. b) Min-Max filtering to compensate for contrast variation and remove the background. c) The binary mask obtained by the peak finding routine. d) Weighted midpoints estimate to define the particle image midpoint.

2.4. 3D Lagrangian Particle Tracking Algorithm

In this section we explain how we track multiple particle as physical objects moving true the 3 dimensional object domain for sufficient long times by information from multiple camera planes. As is sketched in Figure 2.5a the 3D position of an particle, here the micro-algae, can be reconstructed by information from multiple camera's in the object domain, this we refer as triangulation. The object triangulation can achieved by formulating a least squares problem to the calibration mapping to solve the best fitting object position to the particle image midpoints in different camera planes. However, since we have multiple object moving true the object domain, we first need to find which particle images in the different camera's belong to the same physical object, this is referred as matching [61]. Matching can be achieved by projecting a particle image midpoint true the object space and projecting is back on another camera which it ideally crosses another particle on its so-called epipolar line [89] as is sketched in Figure 2.5b for a 4 camera system. Both the correspondence matching for particle images among different camera planes, and the tracking of the particle as physical object in time is sensitive to mismatching, hence we need a robust approach. To efficiently track and reconstruct the object position we follow the work by Attanasi et al. [4], and as well references therein. First we track particle image midpoints in time in the different camera planes separate up to a point which we cannot track, e.g. by occlusion or disappearance. Then we find a consistent correspondence matching between the different trajectories that have been formed in the camera plane to later triangulate a tracked object. As reported by Wu et al. [95] this matching of trajectories is robust against possible mismatching in the correspondence among the different camera plane. The matching of trajectories among multiple camera views can be formulated as a integer optimization problem that is of combinatoric origin, which in this case can be efficiently solved using linear integer programming (ILP). To further reduce the computational complexity of this combinatoric problem, we implement a recursive divide and conquer strategy that first matches long tracks among the different camera views, with much inspiration by the more recent work of Attanasi et al. [4]. Unlike the work by [4], we do not deal with occluding particle images during the track matching. Here, to simplify the algorithm, we only deal with short term occlusions during the triangulation of the position of the physical object. With the upcoming subsections we will define the trajectory of a physical object as γ_o^l [4], here with l a tracking index and subscript o to indicate the object. This trajectory contains its projections in the camera plane, which yet have to be matched, as $\gamma_o^l = \{\gamma_m^l\}$ with m the camera index. First we explain how we track particle image midpoints in the different camera planes to create unmatched indexed tracks γ_m^l in the separate camera planes. Second we explain how the integer optimization problem matches the 2D trajectories among different camera planes to form a complete object trajectory γ_o^l that can then be triangulated after. To solve this optimization problem efficiently to find all the physical object, we explain how we implement a recursive divide and conquer strategy, starting with long tracks first. At last we end this section how we triangulate the object position, and how the triangulation unlike the matching algorithm deals with occlusions.

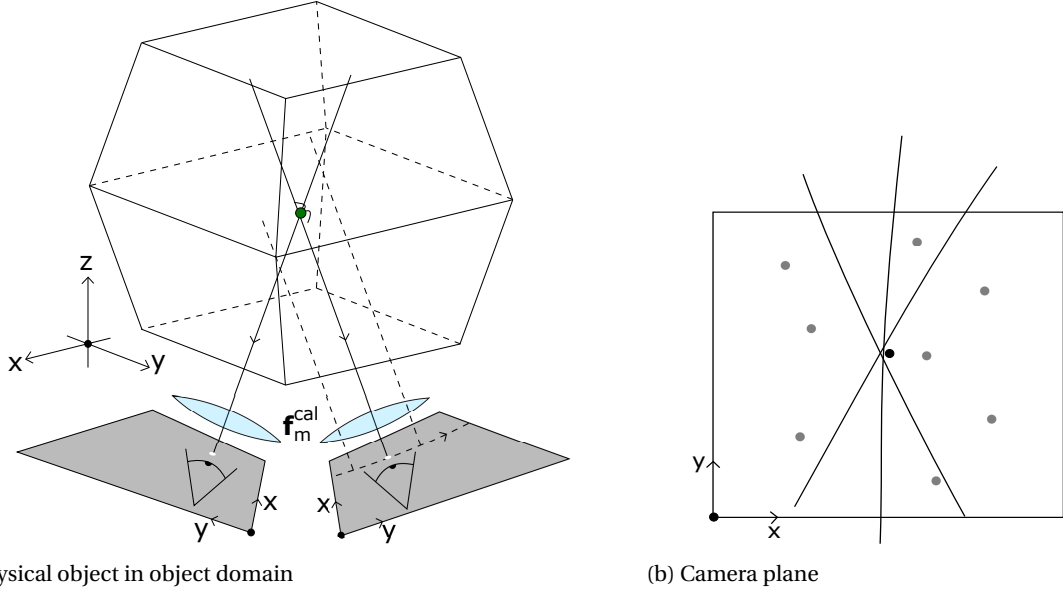


Figure 2.5: Triangulation and matching. a) Sketch of the physical object in relation to the different camera planes from the object domain. b) Each camera has multiple epipolar lines projected from the other camera views where we need to match which epipolar line correspond to which particle image midpoint indicated by the dots.

2.4.1. 2D Particle Tracking Algorithm

First we restrict to the individual camera plane, which contains a list of particle image midpoints as extracted from the camera plane in subsection 2.3.2. We aim to track the multiple midpoints in the camera plane up to a degree allowed by occlusion and disappearance from the field of view or by shortly blinking. Here we start to define a track as a single particle image midpoint that was moving in the consecutive image frames as γ_m^l . Here m denotes the index of the camera of interest and l a specific index that is assigned to a certain track in that camera. These indices are of vital importance as they will later be used to compare different formed tracks among different camera planes. We can create these tracks up to a point that the displacement between the consecutive particle image midpoints in a certain camera m is uniquely defined within a prescribe as a search radius around the particle image midpoint in time. We use a search radius since the actively moving particle can rapidly change its direction. This search radius is set a expected spatial displacement is based on the average displacement between two consecutive image frames with user defined confidence bound, using a consistent time forward and backward nearest neighbor search. When the algorithm measures no unique displacement for a certain particle image midpoint within this search range between the consecutive images frames it raises the index l and continues to define a new track. The unique correspondence in the consecutive image frames is a vital part of the algorithm as we cannot match tracks between multiple cameras when the motion of the tracks is inconsistent. A typical result of this algorithm can be found in Figure 2.6. During this reorganization of the particle image midpoints list from subsection 2.3.2 there is no loss of data.

2.4.2. Track Matching Algorithm

The previous defined tracks γ_m^l in the different camera planes that are yet unmatched among different camera planes, the matching of these tracks is the goal of this section. We start with the definition of a discrete cost function c that we will use to formulate an integer optimization problem. This cost function measures the overall average distance d (see Figure 2.7a) between a track indexed as l in camera m and the epipolar line of a possible candidate track match indexed as h projected from another camera s with $m \neq s$. This cost function is therefore only defined between a track γ_m^l and a candidate match γ_s^h whenever they intersect in the same time frames n . We express this cost function formally as,

$$c_{ms}^{lh} \equiv \mu \left\langle d \left(\gamma_m^l, \gamma_s^h \right) \right\rangle_n \text{ with } \gamma_m^l \cap \gamma_s^h \notin \emptyset.$$

The cost function is positive definite and convex as it measures the a distance between point and the epipolar line projected from another camera, and ideally yields a true minimum at zero, i.e. no disparity between the calibration and experiment. However several sources of disparity are present, e.g. mechanical misaligned

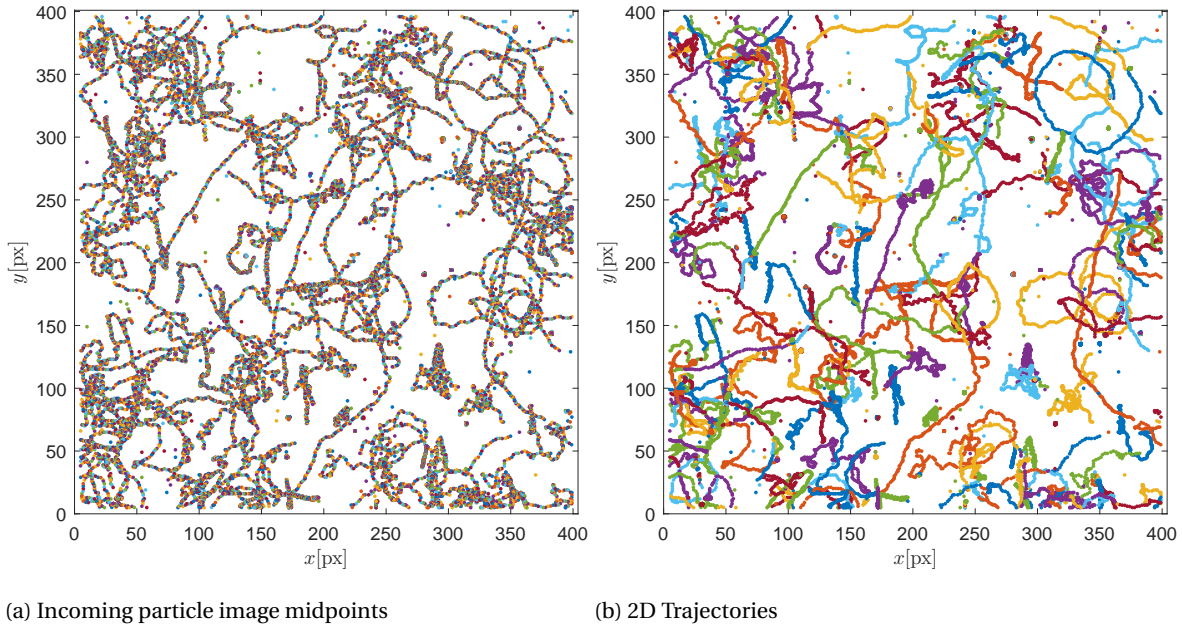
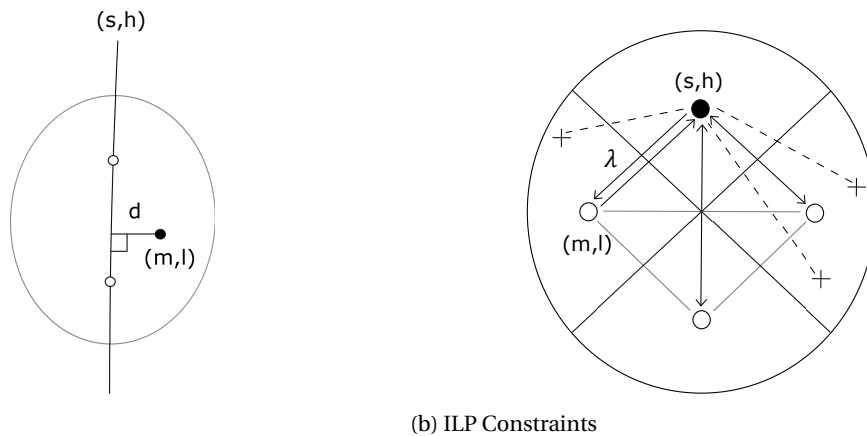


Figure 2.6: 2D Particle tracking. a) Incoming data from the midpoints estimates. b) Different formed trajectories γ_m^l in the camera plane.

in the stage after the calibration and differences in the optical path due additional refraction e.g. due the glassware and the water, and at approximately pixel level a cumulative error of the particle midpoint estimate and uncertainty in the calibration mapping.

We limit the spatial domain of possible candidate matches between tracks in the different camera planes to keep the number of combinations of candidates matches comprehensive. To explain how, we continue to the graphic interpretation of Figure 2.7a. The black dot in Figure 2.7a denotes a particle image midpoint of a indexed track γ_m^l , and the line an epipolar line from another particle image midpoint from a different camera with track γ_s^h and $m \neq s$. We take only into account possible candidate matches which the black dot remains in reach of the white dots on the epipolar line, denoted by the ellipse surrounding them. This decreases the number of possible matches and works well for long tracks in the different camera's. In addition we demand that the point and epipolar line travel in the same direction by limiting the standard deviation of their relative distance d , which the two compared tracks are limited to diverge their relative motion. In this way we continue to limit possible matched of short time intersection. Doing so this greatly reduces the computational complexity limiting the amount of possible candidate matches.



(a) Cost function

(b) ILP Constraints

Figure 2.7: Structure of the integer optimization problem. a) Geometric picture of the discrete cost function as the distance between the selected coordinate (m, l) and candidate epipolar line (s, h) , the ellipse indicates a spatial threshold b) Constraints for the integer optimization as described in the text.

To match the tracks among different camera's, we want to find the minimal value of the discrete cost function between the tracks and candidate matches, as being the best possible match. This can be done by formulation a integer minimization to this cost function, subjected to certain constraints that define a unique basis of tracks that we can triangulate later on. To formulate this problem, the indexed cost function is vectorized as $c_{ms}^{lh} \rightarrow c_i$, and we introduce a binary integer $\lambda_i \in [0 \vee 1]$ that selects components of the vectorized cost function to match two tracks together in different camera planes. Here λ_i is yet unknown, and this variable will need to be solved by the minimization problem. As the cost function is vectorized, we store the track and camera indexing as $(l_i, m_i) \& (h_i, s_i)$ for the candidates, and as well store the initial frame of time intersection n_i^{ini} the end frame of time intersection n_i^{end} for the candidate match. Hence every λ_i has a specific set of corresponding indices that define relations between camera planes and identify the time span of intersection. These will be used to construct certain constraints to the optimization. We start with the full mathematical problem statement as is presented below.

$$c(\lambda) = \min_{\lambda_i} c_i \lambda_i$$

s.t.

$$0 \leq \lambda_i \leq 1 \quad (2.1)$$

$$(S_{ij} - \delta_{ij}) \lambda_j = 0 \quad (2.2)$$

$$(A_{ij} - N\delta_{ij}) \lambda_j \geq 0 \quad (2.3)$$

$$B_{ij} \lambda_j \leq 1 \quad (2.4)$$

$$\sum_i \lambda_i = N \quad (2.5)$$

On top we find the global minimization statement, that sums over all components of c_i factorized with the solution vector λ_i that is either $0 \vee 1$, which we use the Einstein summation convention. This problem definition is linear and can be efficiently solved using integer linear programming (ILP) with the MATLAB solver `intlinprog.m`. Then in Equation 2.1 to Equation 2.5 several equilibrium and in-equilibrium constraint follow, which the solver needs to comply with. The first constraint in Equation 2.1 well illustrates this concept as the integer to solve, i.e. λ_i , is forced to a binary integer $\in [0 \vee 1]$. The other constraint of Equation 2.2 to Equation 2.5 are more involved, therefore we turn to a schematic representation in Figure 2.7b. In Figure 2.7b we have schematized a track in a camera as the index pair (m_i, l_i) and another camera as (s_i, h_i) that will be matched by λ_i to triangulate later on. The 4 quartiles of the circle in Figure 2.7b represent the four different cameras in our setup, where the arrows between the quartiles represent the solution vector λ_i matching the pair (m_i, l_i) and (s_i, h_i) by minimizing the cost c_i between these pairs.

We start with the first constraint of Equation 2.2. This constraint we will refer to as the symmetry constraint. In Figure 2.7b this symmetry constraint is visualized by the back and forth arrows between the index pair (m_i, l_i) and (s_i, h_i) , and demands two links of λ_i to co-exist both ways. We express this constraint formally by using a matrix S_{ij} that operates on a specific link λ_j to map it onto its symmetric counterpart λ_i as $\lambda_i = S_{ij} \lambda_j$. This matrix if formally constructed using the stored indexing as,

$$S_{ij} \equiv [(l_i = h_j) \wedge (h_i = l_j) \wedge (m_i = s_j) \wedge (s_i = m_j)].$$

This mean if a component of λ_i with index pairs $(m_i, l_i) \& (s_i, h_i)$ along the rows of S_{ij} has an unique symmetric counterpart λ_j with index pairs $(m_j, l_j) \& (s_j, h_j)$ along column of S_{ij} then $S_{ij} = 1$, which can be used to map λ_j on to λ_i . In Equation 2.2 we subtract the solution vector λ_i from mapped vector $S_{ij} \lambda_j$, which can only add up zero if the symmetric index pairs are both selected or none.

Next we continue with the first in-equilibrium constraint of Equation 2.3, which is indicated by the three arrows that approach the black dot in Figure 2.7b. This constraints demand at least $N = 3$ links to exist to the index pair (s_i, h_i) for our 4 camera system in some time frame. In such in-equilibrium constraint the minimization will choose the least number needed. To formalize this statement, we create a matrix A_{ij} that performs a summation over λ_j and maps it onto λ_i .

$$A_{ij} \equiv [(h_i = h_j) \wedge (s_i = s_j) \wedge (n_i^{\text{ini}} \leq n_j^{\text{end}}) \wedge (n_i^{\text{end}} \geq n_j^{\text{ini}})]$$

This matrix means if a component of λ_i with (h_i, s_i) along the columns of S_{ij} , has a similar link λ_j with $\{h_j, s_j\}$ along the rows of A_{ij} then $A_{ij} = 1$, and can be used to sum over the number of found similar links λ_j and map is onto λ_i . Here in addition we need to use the information of the start n_i^{ini} and end n_i^{end} of the intersection, as

all the track matches need to intersect in time together. As A_{ij} sums over the components of λ_j we subtract the solution vector λ_i times $N = 3$, which forces a minimum of $N = 3$ links to approach (h_i, s_i) in Figure 2.7b.

We continue with the second in-equilibrium constraint of Equation 2.3. Demanding a minimum number links to approach (h_i, s_i) in Figure 2.7b, still allow multiple links to come from 1 camera as indicated by the dashed lines in Figure 2.7b, thus need to be forced out. These links are excluded as we demand that each link to (h_i, s_i) from a camera is unique. This uniqueness can be forced by further restriction to matrix A_{ij} which we define as B_{ij}

$$B_{ij} \equiv [A_{ij} \wedge (m_i = m_j)].$$

Additional in B_{ij} to A_{ij} each component of λ_i and λ_j need to share camera m . As $B_{ij}\lambda_j$ performs a summation of the selected components in λ_j we demand uniqueness by a maximum of 1 in the summation by Equation 2.4. Together the constraint Equation 2.2 and Equation 2.4 guarantee a unique basis

At last we need to force the minimization to not select the trivial minimal solution to the cost of $\lambda_i = 0$, as our constraints still allow, which would match nothing. Therefore we end with the last constraint of Equation 2.5 to ask the solver to match at least a complete basis of tracks γ_o^l . We find a complete basis by demanding a total number of at least $N = 3$ links. By the other constraints this will add up to 12 links to be formed which define a basis that can be triangulated, for our 4 camera system. Since it is our goal to find more than 1 trajectory, the next section is devoted to introduce an efficient solution strategy to increase the number of tracks to be found. The described matrices in this section are relatively sparse and therefore are efficiently constructed in MATLAB using `bsxfun.m` exploiting the sparsity.

2.4.3. Divide and Conquer Algorithm

The full combinatoric optimization problem gets increasingly computational complex with multiple camera planes, number of tracked particle midpoints, increasing disparity between the calibration and experiment, and the number of time frames to be processed. As well do we not know how many physical object can be tracked in among the different camera's. So far with the end of the last section track the matching algorithm only solves 1 basis, in this section we increase this number. We increase the number of tracks that can be matched in an iterative procedure that finds the maximum number of correct possible trajectories γ_o^l . However solving the complete optimization problem for every iteration as a search for a new tracks to match is very inefficient and time consuming, therefore we make some crucial observations similar to the work by Attanasi et al. [4]. First we define feasible solution set F that contains all possible combination of trajectories allowed by the candidate matches. We observe that we need to find the correct solution set $\Lambda \subseteq F$ that matches only the correct tracks γ_o^l together that comply with the integer optimization constraints. This implies that there exist as well an exclusion set $E = (\Lambda)^c \subseteq F$. This we can use during an iterative procedure, since the current number of matched tracks in the iteration rules out certain other links that have created as possible candidate matches by conflict in constraints.

To design a iterate procedure we first define the current solution set as L that contains correctly matched tracks γ_o^l , and exclusion set E that contains candidate matches that are ruled out by L . Additional we define a feasible match set as $G \equiv (L \cup E)^c \subseteq F$. Then we want to further decrease the computational complexity of G by selecting some sub-problem $G^* \subseteq G$ of choose, which we solve first. We identify the following criteria that can be used.

1. Match tracks that have a large intersection in time, and are therefore more likely to be correct matches denoted as G^{int} .
2. Branch from the current solution L to find remaining links that complete the current solution L denoted as G^{bran} .
3. Select time frames to find to find tracks that can we matched, denoted by G^{time} .
4. Further reduce the computational complexity by considering cost values to expectation by the solution set L , denoted as G^{exp} .

We implement these criteria in a recursive "Divide and Conquer" strategy. First we implement criteria 1 – 2 as a recursive subdivision G^* and conquer by the solution and exclusion set L, E . Then, since there can still remain links λ_i that can yield possible correct matches between tracks, we sweep true the time frames by a recursive division of 3 – 2 in similar fashion. As we select the set G^* some constraint can not be met a priory,

hence can be used to further shrink G^* in advance. Whenever the selected sub-problem G^* is still to large we use criterion 4 to limit the selected sub-problem G^* further by considering only expected cost values.

Practically this recursive divide and conquer strategy can implemented in the optimization of the previous section by defining a the current solution vector λ_i^n and a next one λ_i^{n+1} . From the current solution vector one can compute the current exclusion vector e_i for example by the constraints as $e_i = ((S_{ij} + \delta_{ij})(B_{ij} - \delta_{ij})\lambda_j < 1)$. The current solution vector λ_i^n and exclusion vector e_i can be used to redefine the upper and lower bound to the next solution vector λ_i^{n+1} of Equation 2.2 as,

$$\lambda_i^n \leq \lambda_i^{n+1} \leq e_i.$$

Then we force new matches by increasing the minimal number of solutions to find of Equation 2.5 as,

$$\sum_i \lambda_i^{n+1} = \sum_i \lambda_i^n + N.$$

In addition to the recursive divide and conquer strategy, we define as well a vector d_i^n that measures the overall disparity between combinations of camera's as the average cost of the the solution set L , for each combination of camera views separately. During the iterative divide and conquer algorithm we compensate for the expected disparity between camera views as,

$$c(\lambda) = \min_{\lambda_i} |c_i - d_i^n| \lambda_i^{n+1}$$

This compensation for the cost function can be seen as some form of machine learning.

2.4.4. Triangulation

Having matched segments of tracks among different camera's we are now able to define a complete the triangulation. We reconstruct the physical object position \mathbf{x}_o by use of a create a least squares problem to invert the calibration mapping. To partially deal with disappearance and occlusion of particles in different camera's, we allow the least squares problem to be incomplete, which it at least need two camera's. To do this we introduce a integer weight $w_m \in [0 \vee 1]$.

$$R(\mathbf{x}_o) = \sum_m w_m \left\| \mathbf{x}_m - \mathbf{f}_m^{\text{cal}}(\mathbf{x}_o) \right\|_2$$

We wish to minimize this residual R to find the best object location. Such problem can either be solved naively in MATLAB using `fminunc.m` / `fmincon.m` which is robust, or more time efficient by user defined Newton-Raphson routine. Since the mapping function is of polynomial form, we expect the Newton-Raphson scheme to converge as the derivatives are well behaved and non-vanishing, and implement the following iterative scheme.

$$\begin{aligned} \text{Newton-Raphson Scheme : } \nabla \nabla R(\mathbf{x}_o^n) \mathbf{v}^n + \nabla R(\mathbf{x}_o^n) &= \mathbf{0} \\ \mathbf{x}_o^{n+1} &= \mathbf{x}_o^n + \mathbf{v}^n \end{aligned}$$

We can easily create this problem by the MATLAB symbolic toolbox using `gradient.m` and `hessian.m` to find analytic expressions for the gradient and hessian matrix, and functionalize them by `matlabFunction.m`. We iterate the Newton-Raphson scheme at sufficient sub-pixel accuracy with relative error of $\epsilon_{\text{res}} = \|\mathbf{v}^n\|_2 < \mathcal{O}(10^{-3})$, which defines the numeric precision of the code.

2.5. Post Processing

Up so far we have discussed the pre processing steps that includes all procedures to track and triangulate the time-positional information of the micro-swimmers in the object space. In this section we continue to post process and retrieve properties to interest of the individual trajectories by the micro-swimmers, and as well define the boundaries to the fluid domain they swim in. Several methods are discussed and motivated to refine the data. We start to discuss how we parametrize, smooth and differentiate the obtained 3D time positional information by curve fitting and interpolation. Secondly we discuss how we define the boundaries of the top and bottom glassware by the fitting of planes to an independent triangulation of algae that remain immobile. After we discuss how this information can be used to find desirable properties of trajectories to quantify their dynamics.

2.5.1. Curve Fitting

As will be explained in subsection 2.5.3 we need up to the 3rd order time derivative of the time parametrized trajectory $\mathbf{r}(t)$ to study the kinematics of the microorganisms along their trajectory. Since numeric differences, e.g. central differences, are sensitive to the discretization and noise from the experiment we aim to use a curve fitting procedure to the raw object data \mathbf{x}_0 to discard noise and find the time derivatives by analytic means [18]. In this work we choose to least squares fit a polynomial curve to the raw object data \mathbf{x}_0 in time. Such a curve has desirable properties which it can well describe oscillatory behavior for short times, and it decouples the least squares problem wherefore it allows to fit a polynomial in time to each coordinate separately. We prescribe this as a smoothing procedure on a time sliding stencil that can as well find the time derivative by analytic means. Smoothing a signal by a polynomial is a widely used method and is formally known as a Savitzky-Golay filter. Such filter is known to best preserve the dynamics while rejecting noise by the polynomial smoothness requirement. We functionalize a user defined the Savitzky-Golay filter using the functions `polyfit.m` and `polyder.m` to simultaneously smooth and differentiate (which not available in the matlab routine `smooth.m`). Our user defined script as well allows a non-uniform time stencil to take into account time positions of the physical object that could non be triangulated but where continued to be matched in later frames. As well is special care taken to the ends of a trajectory, which it was either started to be tracked or was not tracked anymore. At the ends we grow and destroy the prescribed stencil size N_{stn} , and smooth at reduces the polynomial order N_{ord} to allowed level $N_{\text{ord}} < N_{\text{stn}}$. Since we need up to the 3rd order derivative in subsection 2.5.3, we aim to fit at least $N_{\text{ord}} = 3$ order polynomials.

2.5.2. Bounding Domain

To study how the algae interact with physical boundaries we independently define the upper and lower boundary of the glassware, by a separate triangulation of immobile algae. We do this by a stripped down version of the explained tracking algorithm, which reconstructs the position of immobile algae that are stuck to the top and bottom of the flow-chamber. To find the immobile algae we use a time averaged image in each camera. Using the reconstructed object coordinates of the immobile algae we fit a plane up to 1st order to include any inclination of the flow chamber using the MATLAB fitting toolbox `fit.m`. At last we compensate for the size of the algae shifting the top plane 1/2 body-length up and the bottom plane 1/2 body-length down. Since the immobile algae have a slight negative buoyancy they presumably sink to the bottom of the flow chamber which is better sampled, therefore the top boundary is not included in any quantitative results.

2.5.3. Trajectory Kinematics

The filtered time-positional information of the algae in the fluid domain used to compute their local frame of reference by the Frenet-Serret framework [13]. In this section we keep the notation to practical insight and elaborate the details of this framework up to the degree that is needed. The Frenet-Serret framework defines a local frame by use of the local tangent \mathbf{t} , normal \mathbf{n} , and bi-normal vector \mathbf{b} to the trajectory position vector $\mathbf{r}(t)$ known as the Frenet trihedron $\{\mathbf{t}, \mathbf{n}, \mathbf{b}\}$.

$$\mathbf{t}(t) \equiv \frac{\mathbf{r}'(t)}{\|\mathbf{r}'(t)\|_2}, \quad \mathbf{n}(t) \equiv \frac{\mathbf{t}'(t)}{\|\mathbf{t}'(t)\|_2}, \quad \mathbf{b}(t) = \mathbf{t}(t) \times \mathbf{n}(t).$$

Here $(\bullet)' = \frac{d}{dt}$ denotes the time derivative. These vectors can be computed by the analytic differentiation of the fitted curves in subsection 2.5.1. This right-handed orthogonal basis is sketched in Figure 2.8, and is assumed to follow the organisms instantaneously in the absence of inertial forces. Therefore the dynamic evolution of this frame along a curve is therefore of great interest, as it much relates to the kinematics imposed by the algae. The dynamics of the trihedron along the trajectory can be understood by the curvature κ and torsion τ which describe evolution of the trihedron along its paths as,

$$\begin{bmatrix} \mathbf{t} \\ \mathbf{n} \\ \mathbf{b} \end{bmatrix}_{,s} = \begin{bmatrix} 0 & \kappa \mathbf{I} & 0 \\ -\kappa \mathbf{I} & 0 & \tau \mathbf{I} \\ 0 & -\tau \mathbf{I} & 0 \end{bmatrix} \begin{bmatrix} \mathbf{t} \\ \mathbf{n} \\ \mathbf{b} \end{bmatrix}$$

where $,s$ denotes the differentiation with respect to the arc-length,

$$s(t) = \int_0^t \|\mathbf{r}'(\xi)\| d\xi.$$

The curvature $\kappa \sim [\text{m}^{-1}]$ quantifies how much a trajectory is bend, and can be understood as an inverse radius of bending r^{-1} . Likewise the torsion $\tau \sim [\text{m}^{-1}]$ can be understood as a measure how much the trajectory twist

and fails to be co-planar. Therefore the trihedron is constantly reorienting with respect to its Darboux vector $\boldsymbol{\omega}$,

$$\boldsymbol{\omega} = \tau \mathbf{t} + \kappa \mathbf{b}.$$

The curvature and torsion can as well directly be computed from the analytic differentiation of the fitted curves in subsection 2.5.1.

$$\kappa(t) = \frac{\|\mathbf{r}'(t) \times \mathbf{r}''(t)\|_2}{\|\mathbf{r}'(t)\|_2^3}, \quad \tau(t) = \frac{[\mathbf{r}'(t), \mathbf{r}''(t), \mathbf{r}'''(t)]}{\|\mathbf{r}'(t) \times \mathbf{r}''(t)\|_2^2}$$

It is clear these entities are now time dependent, which they dependent up to the 3rd order derivative, hence sensitive to noise. Therefore they are smoothed by a moving average filter since these should be slowly changing variables by the motile organisms. The trajectories of micro-algae and likewise organisms have been reported to be of helical nature [18, 52]. A helix can be better understood in terms of its radius R , pitch P , and as well the angular velocity magnitude Ω in addition to the velocity magnitude V of the organisms. We compute these quantities using the information from the curvature and torsion by,

$$R = \frac{\kappa}{\kappa^2 + \tau^2}, \quad P = \frac{2\pi\tau}{\kappa^2 + \tau^2}, \quad \Omega = \text{sgn}(\tau)V\sqrt{\kappa^2 + \tau^2}.$$

These measures will be used to quantify the kinematics of the trajectories that are made by the micro-algae.

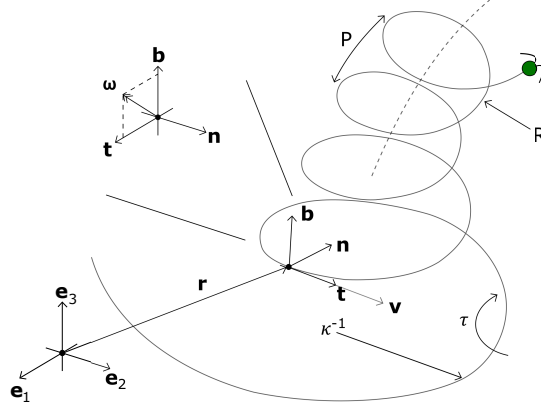


Figure 2.8: Trajectory kinematics. Local position $\mathbf{r}(t)$ of the Frenet trihedron $\{\mathbf{t}, \mathbf{n}, \mathbf{b}\}$ with respect to a fixed Cartesian reference $\{\mathbf{e}_1, \mathbf{e}_2, \mathbf{e}_3\}$. The Frenet trihedron travels along trajectory $\gamma(t)$ with position vector $\mathbf{r}(t)$, curvature $\kappa(t)$ and torsion $\tau(t)$. The inset show specific interpretation to the Darboux vector $\boldsymbol{\omega}$.

2.6. Algorithm Performance and Synthetic Data Validation

Before we continue to the results of chapter 3, we end this chapter by an evaluation of the Lagrangian particle tracking (LPT) algorithm by comparing the experimental reconstruction to results obtained by self generated synthetic data. This section is only of exploratory origins to quantify the overall quality of the processed data, and not to do a detailed study the performance of the LPT algorithm by different setting. We evaluate the quality of the algorithm by use of the Pareto frontier in line with the work by Attanasi et al. [4]. The Pareto frontier marks the distribution of available resources, here the spatio-temporal sampling in the TN -plane. The Pareto frontier can be seen as an efficiency boundary, with T the temporal sampling as the number of time frames, and N the maximum possible number of tracked object. The available resources are identified as the number of particles in the camera views N_{cam} and the maximum available number of frames in the post-processing T_{max} . It is clear that this yields a boundary to the available resources and cannot be crossed in the reconstruction for each individual experiment. However this definition does not take into account that particles can leave the domain, hence would limit the tracked number of frames without having a performance drop. Therefore we as well define a truncation to the Pareto frontier, which the temporal sampling is truncated by the residence time in the domain ($\sim 400 \times 400[\text{px}]$) by the expected particle image displacement ($\sim 4[\text{px}/\text{frm}]$), here $T_{\text{max}} \sim 150$ frames. We rationalize the number of reconstruction objects N_{obj} and the tracked number of frames T_{obj} towards both the Pareto frontier and its truncation to quantify the behavior

of the algorithmic reconstruction of the experiment. We identify a quantitative efficiency of the algorithmic reconstruction η_{rec} as,

$$\eta_{\text{rec}} = \frac{N_{\text{obj}}}{N_{\text{cam}}}.$$

The experimental data was processed on both a dual core i7 laptop with 16 GB RAM and local clusters with either 8 cores and 24 GB RAM running 2 jobs in parallel or 12 cores with 65 GB running 4 jobs in parallel. Using MATLAB the code was not compiled to match maximum efficiency, we found the run-time lasted 2-3 days on average. To fit the memory capacity of the used machines the experiments were subdivided into either 4 or 8 separate time series.

2.6.1. Synthetic Data

We start to test the algorithm by using synthetic data that we designed to mimic to extreme case of the experiment. First, we model the active swimmers as helical trajectories, expected from the literature [16, 18, 52]. Second we aim to mimic immobile algae as small circular orbits having no net displacement over long times. Using the synthetic data there is interest whether we rule out or identify any source of directional bias in the object tracking and reconstruction at varying density. The synthetic data is created by randomly imposing the described trajectories in the domain with periodic boundary conditions. The number of imposed time frames T_{imp} and objects N_{obj} , as well as the object domain size and overall displacement of the objects are sampled to what is observed in the experiments of the next section. The settings and results for the synthetic data experiments summarized in Table 2.1a for the helical trajectories, and Table 2.1b for the circular orbits. For both types of trajectories it is found that most imposed object were reconstructed at a quantified overall reconstruction efficiency of $\eta_{\text{rec}} \sim 98\%$. In addition there was no qualitative indication for sources of directional bias, and therefore can be assumed to be ruled out under these conditions. In Figure 2.9a we plot the reconstruction in the TN -plane for the synthetic data experiments. It is clear that the helical trajectory (blue marks) follow the truncation to the Pareto frontier as they can leave the domain. In contrast the circular orbits (green marks) are tracked up to the available resources as they do not leave the domain, and therefore mark the Pareto frontier [4]. Exploring these two extreme cases we conclude that the algorithm can achieve a high reconstruction efficiency. We expect a proper experimental tracking of the reconstructed object to lie within the Pareto frontier and its truncation, as the experiment have both motile and immobile algae in the flow domain.

dilution	$T_{\text{imp}}[\#]$	$N_{\text{imp}}[\#]$	$N_{\text{obj}}[\#]$	$T_{\text{obj}}[\#]$	$\eta_{\text{rec}}[\%]$	$d[\text{px}]$
1:base	0×125	800	-	-	-	-
2	0×250	400	-	-	-	-
4	2×500	200	196.62 ± 2.32	73.59 ± 79.41	98.31	$2.09 \pm 84.86 \cdot 10^{-3}$
8	2×1000	100	98.63 ± 1.20	69.02 ± 102.76	98.63	$5.73 \pm 173.46 \cdot 10^{-3}$
16	1×2000	50	49.72 ± 0.60	101.56 ± 119.91	99.43	$0.24 \pm 0.22 \cdot 10^{-3}$
32	2×2000	25	24.84 ± 0.42	75.52 ± 125.17	99.35	$0.55 \pm 20.27 \cdot 10^{-3}$

(a) Helix trajectories

dilution	$T_{\text{imp}}[\#]$	$N_{\text{imp}}[\#]$	$N_{\text{obj}}[\#]$	$T_{\text{obj}}[\#]$	$\eta_{\text{rec}}[\%]$	$d[\text{px}]$
1:base	0×125	800	-	-	-	-
2	2×250	400	390.09 ± 0.33	218.66 ± 81.20	97.52	$0.20 \pm 0.21 \cdot 10^{-3}$
4	3×500	200	196.10 ± 0.54	221.74 ± 244.71	98.05	$0.25 \pm 0.25 \cdot 10^{-3}$
8	1×1000	100	98.00 ± 0	1000.00 ± 0.00	98.00	$0.20 \pm 0.19 \cdot 10^{-3}$
16	2×2000	50	49.23 ± 0.35	1437.48 ± 699.19	98.44	$0.14 \pm 0.18 \cdot 10^{-3}$
32	1×2000	25	25.00 ± 0.00	2000.00 ± 0.00	100.00	$0.23 \pm 0.25 \cdot 10^{-3}$

(b) Circular orbits

Table 2.1: Results for the synthetic data reconstruction. a) Imposed helix trajectories. b) Imposed circular orbits. Both have T_{imp} the imposed number of frames, N_{imp} the imposed number of objects, N_{obj} the reconstructed number of object, T_{obj} the tracked number of frames in the object, η_{rec} the reconstruction efficiency, and d the disparity between the camera's (here at numeric precision of the code, see subsection 2.4.4).

2.6.2. Experimental Data

We vary the cell density in the performed experiments by diluting the cell suspensions halving the density each time the suspension is diluted, with the methods described in section 2.1. We refer to each experiment by its dilution steps taken toward the base suspension. In addition, as the experiment is diluted, the recorded number of frames is doubled, up to $T_{\text{frm}} = 8000$ frames, therefore the available resources in the TN -plane are expected to scale as $T \sim N^{-1}$. In Table 2.2a we present the reconstruction results for the wild-type (cc125), and in Table 2.2b for mutant (mbo-1) cells, which for both we will present the results in chapter 3. The base suspensions for both the types was found to be to computationally involved to triangulate due their high density, and are therefore excluded. For the wild-type (cc125) cells the average reconstruction efficiency was found to be around $\eta_{\text{rec}} \sim 70\%$. Part of this efficiency can be explained by the edges that are lost in the relative orientation of the camera's under absolute angle of 10° . Other sources include disparity, partially-identified particles images, occlusions, mismatching, wrongly identified noise, and increasing computational complexity by cell density. In Figure 2.9a we find that the reconstruction for the wild-type cells (blue) does not mark the Pareto frontier [4], but do follow its expected scaling of $T \sim N^{-1}$. Part of the discrepancy between the reconstruction and frontier can be explained due the non-ideal reconstruction efficiency $\eta_{\text{rec}} \sim 70\%$. However a more significant influence can be identified as some part of the motile algae can leave the domain within the time-span of the experiment, whereas only immobilized algae can be tracked for the whole experiment. Therefore the expected reconstruction performance in the TN -plane should lie within the Pareto frontier and its truncation, as explained in the previous subsection. This expectation is indeed found in Figure 2.9a, which the highest density falls below the truncation but remain within order of the synthetic tracking experiments. As we continue to the mutant (mbo-1) cells we found that the algorithmic reconstruction was more computationally involved since most of the algae crowd the glassware (see chapter 3), and therefore had high localized cell densities in the fluid domain. As can be found in Table 2.2b, we did not triangulate all time frames of the experimental data for reason that will be explained in chapter 3, and reduced the computational complex by limiting the number of time frames to process. In overall we found a reconstruction efficiency of $\eta_{\text{rec}} \sim 50\%$, which be due the high localized density at the surface as many algae cannot consistently be found among the different camera views. In Figure 2.9b we find that the mutant experiments (marked green), do not follow the Pareto frontier as defined, since they where processed as reduced time frames. Taking into account that less frames where processed, the tracking of the objects seem to be about half the available resources, which presumably is as well due the high localized density at the surface. In overall we find that the tracking of the object in the flow domain is at expected reconstruction quality, which the physical object are tracked for sufficient long times. In addition we find that the reconstruction achieved here yields comparable result to the literature e.g. [91, 95–98], but does not outperform the recent work of Attanasi et al. [4].

dilution	$T_{\text{cap}}[\#]$	$T_{\text{proc}}[\#]$	$N_{\text{obj}}[\#]$	$T_{\text{obj}}[\#]$	$\eta_{\text{rec}}[\%]$	$d[\text{px}]$
1:base	1000	0×125	-	-	-	-
2	2000	8×250	543.70 ± 21.43	57.04 ± 58.78	60.82	1.59 ± 0.78
4	4000	8×500	278.66 ± 9.02	141.10 ± 140.74	75.36	1.59 ± 0.76
8	8000	8×1000	143.96 ± 5.95	232.94 ± 260.19	74.31	1.61 ± 0.89
16	8000	4×2000	72.31 ± 5.72	332.91 ± 453.93	73.75	1.56 ± 0.78
32	8000	4×2000	52.46 ± 3.88	605.96 ± 718.30	64.39	1.71 ± 1.04

(a) Wild-type (cc125)

dilution	$T_{\text{cap}}[\#]$	$T_{\text{proc}}[\#]$	$N_{\text{obj}}[\#]$	$T_{\text{obj}}[\#]$	$\eta_{\text{rec}}[\%]$	$d[\text{px}]$
1:base	1000	0×125	-	-	-	-
2	2000	0×250	-	-	-	-
4	4000	1×500	337.72 ± 5.95	237.50 ± 195.67	71.84	1.53 ± 0.82
8	8000	2×1000	162.05 ± 4.44	347.85 ± 376.42	57.74	1.55 ± 0.81
16	8000	2×500	97.62 ± 3.36	223.98 ± 206.77	42.69	1.60 ± 0.87
32	8000	2×500	53.53 ± 2.83	215.95 ± 215.71	41.13	1.56 ± 0.87

(b) Mutant (mbo-1)

Table 2.2: Results for the experimental data reconstruction. a) Wild-type (cc125) experiment, actively exploring the fluid domain. b) Mutant (mbo-1) experiments, mostly crowding the bottom glassware. Both have T_{cap} the captured number of frames, T_{proc} the processed number of frames, N_{obj} the reconstructed number of object, T_{obj} the tracked number of frames in the object, η_{rec} the reconstruction efficiency, and d the disparity between the camera's.

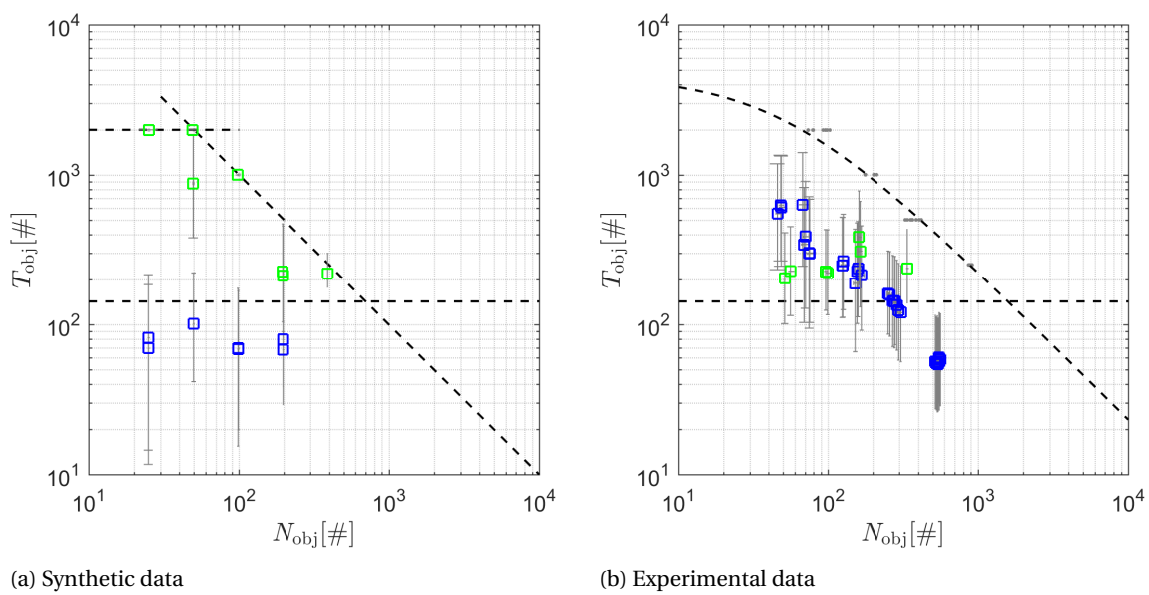


Figure 2.9: Reconstruction performance in the TN -plane, the dashed lines marks the identified to the Pareto frontier and its truncation. a) Synthetic data reconstruction with the imposed helical trajectories (blue) flowing the truncation and the circular orbits (green) marking the Pareto frontier. b) Experimental data reconstruction with the wild-type (cc125) cells following the expected scaling $T \sim N^{-1}$ and the mutants (green) are at reduced data processing (see text).

3

Results

We continue to the results obtained from the experimental reconstruction discussed in section 2.6. The goal of this chapter is to explore the physics of the swimming algae to as much detail as allowed by the experimental accuracy. This chapter is outlined as follows. First we introduce the triangulation of the tracked physical object (algae), on the experiments carried out with the wildtype (cc125) cells and explain why we withdraw attention from the experiments on the mutant (mbo-1) cells. Secondly we continue to study the geometry of the trajectories made by the individual organisms by using the methods introduced in subsection 2.5.3. With the first two sections we hope to give a good understanding how the algae explore and move true the fluid domain. We end this chapter with the main goals of this research which is to study interactions of cells with physical boundaries and with each other. We aim to focus much on the cell-wall interactions, since they are of less complexity. For the cell-cell interactions we only touch upon the complexity in light of the cell-wall interactions, since the dynamics of the cell-cell interactions have much more degrees of freedom, which a full study remains beyond the scope of this thesis. We aim to present the results in a descriptive nature, the discussion and conclusion on our results will be left for the following chapters.

3.1. Experimental Reconstruction in the Eulerian Reference Frame

We start with the classical fluids point of view, i.e. the Eulerian frame, and fix our frame of reference to the calibrated object domain. In Figure 3.2a to Figure 3.2e a 10 seconds time-shot is presented of the object reconstruction for the wildtype (cc125) cells together with the bottom boundary definition as they explore the domain. In Figure 3.2f we present a single experiment for the mutant (mbo-1) backward swimming phenotype. We will refer to each specific experiments by the amount of dilution to the base suspension. As can be found in Table 3.1 we were able to reconstruct the experiments done with the $2 - 32\times$ diluted base suspension, whereas the base suspension was too computationally involved. We successfully reconstruct a cell density ϕ_d ranging from $\phi_d = \mathcal{O}(10^4 - 10^5)$ [cells/ml] in agreement with expectations that can be drawn from the density of the base suspension. Based on the disparity between the triangulation of the physical objects and particle images in the camera plane, the triangulation of the physical objects yields an overall precision is within the tens micron range $\varepsilon_o \sim 3[\mu\text{m}]$. As trivial consequence a similar accuracy for the plane fit $\varepsilon_s \sim 5[\mu\text{m}]$ is found, here based on the plane fit residual from the triangulated boundary points. Therefore the overall accuracy of the experiment lies within the length scale of the organism $l_b = 10[\mu\text{m}]$. The overall reconstructed height h of the object domain was found to be $h = 1.2[\text{mm}]$, and is consistently found among the different experiments. However this object height is 20% smaller than expected from the used $1.5[\text{mm}]$ thick acrylic sheet. This could be either explained due a cumulative error from the tens micron precision z -stage or due bending stresses in the glued glassware, and need to be taken care of in the discussion of the results when applicable. The overall xy -span of the object domain was found to be in range of $2 \times 2[\text{mm}]$ loosing some edges to expectation by the relative orientation of the cameras (see subsection 2.2.1). This domain is sufficient unbounded for the algae as it extends up to ~ 200 body lengths. Our curve fitting procedure of subsection 2.5.1 to the time-positional information of the tracking algorithm, was found to perform best at prescribed stencil of $N_{\text{stn}} = 15$ points fitting a $N_{\text{ord}} = 6$ th order polynomial.

First we focus our attention to the $2 - 16\times$ diluted experiments in Figure 3.2a to Figure 3.2d done with the wild-type cells (cc125). We find unexpected behavior as the algae explore the domain, which they mostly

swim up and down the top and bottom glassware at equal pace. The color scheme in Figure 3.2 indicates this behavior by the orientation θ of tangent vector \mathbf{t} of the organism towards the z -direction \mathbf{e}_3 of the calibrated object domain as $\theta \equiv 90^\circ - \angle(\mathbf{t}, \mathbf{e}_3) \in [-90^\circ, +90^\circ]$, shifted to clarify up at $\theta \rightarrow +90^\circ$ and down $\rightarrow -90^\circ$. Using the color scheme the cells swim down (blue) at $\theta \sim -70^\circ$ and up at $\theta \sim +70^\circ$ (yellow), as the direction naturally follows. Much different behavior is found near the reconstructed boundary which the algae remain to circle clockwise or wobble co-planar $\theta \sim 0^\circ$ to the surface (cyan), as will be studied in more depth in section 3.3. In Figure 3.1a to Figure 3.1d we compute a overall cell count averaged in time over the height h of the domain for the $2 - 16\times$ diluted experiments. This count can be seen as a cell concentration profile, where it is found that a significant proportion remains at the boundary. First we note that the sharp peak just above the surface in the different figures is due to immobile cells that remain at the surface, as the size of this count corresponds well to the number of cells used to define the bottom boundary definition. Then, ignoring this peak by visual inspection, a similar decaying trend can be found from the boundary to the bulk. We use this trend to rationalize a finite length scale $l_{\text{bnd}} = 100[\mu\text{m}]$ which the algae are found to remain near the boundary for all the experiments together. This length scale indicates an domain of influence by the surface up to 10 body-length of the organism, and can as well be found on top of the domain. From now on we will refer to the boundary region as up to l_{bnd} away from any physical boundary, and the bulk region as the remaining domain outside this layer. We continue our attention to the most diluted suspension done with the wild-type (cc125) cells in Figure 3.2e and find only few algae that explore the bulk. This experiment can as well be use to verify that our flow-domain is at rest, as only on the full course of the experiment a Stokesian background flow was found (see Appendix A). Concerning the time averaged cell count over the height h of the domain, we find that the cell concentration profile is less smooth due a less available number of data points. We end this section to continue to the mutant (mbo-1) experiment of Figure 3.1f and its concentration profile in Figure 3.2f. It is found that the mutant cells remain mostly to crowd the surface, which they remain immobile on the total course of the experiment. Since we find no interesting behavior in these experiment we discard them from the upcoming sections and only briefly discuss them in the next chapter. The remaining experiments with the mutant cells as where introduced in section 2.6 can be found in Appendix B.

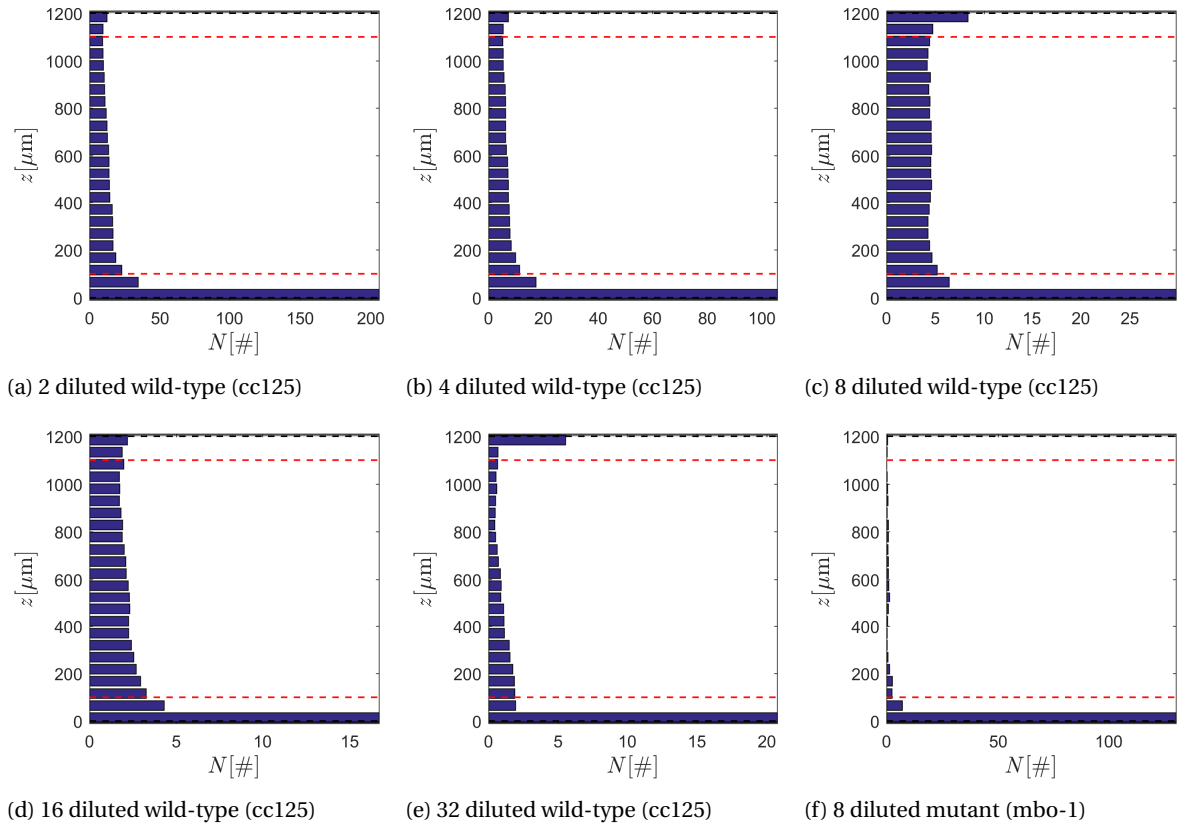


Figure 3.1: Cell count over the height z of the fluid domain. The boundary region is indicated by the dashed red lines. a-e) Cell density count for the wild-type cells. f) Cell density count for the mutant (mbo-1) cells.

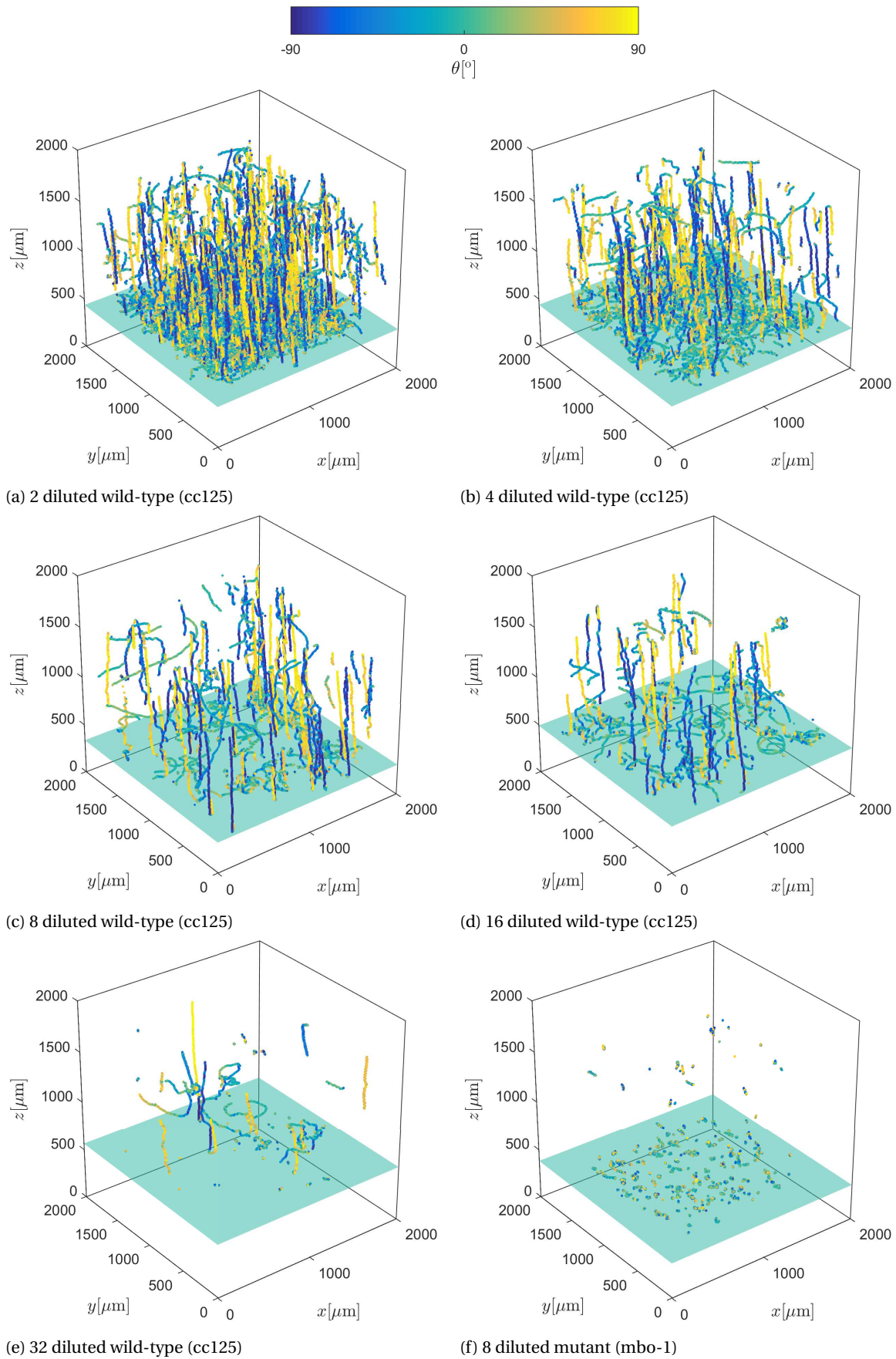


Figure 3.2: 10 second time shot of the triangulated trajectories. a-e) Reconstruction at halving the density, with on few cells in the most dilute case. f) Reconstruction for the mutant (mbo-1) cells mostly crowding the surface, with only few in the bulk. The color scheme denotes the orientation of the cells along their trajectories towards the surface $\in [-90^\circ, 90^\circ]$, mostly swimming up and down.

dilution	ϕ_{dens} [cells/ml]	t_{rec} [s] / proc.	t_{trk} [s]	$\varepsilon_{\text{ptri}}$ [μm]	ε_{sft} [μm]
1:base	$0.5 \cdot 10^6$	-	-	-	-
2	$0.1499 \pm 0.058 \cdot 10^6$	129.9 / 8	3.6 ± 3.8	3.66 ± 1.80	5.62 ± 1.15
4	$0.0882 \pm 0.0029 \cdot 10^6$	259.7 / 8	7.81 ± 8.28	3.67 ± 1.76	3.64 ± 0.81
8	$0.0360 \pm 0.0016 \cdot 10^6$	519.5 / 8	16.11 ± 17.68	3.73 ± 2.04	7.05 ± 2.69
16	$0.0215 \pm 0.0021 \cdot 10^6$	519.5 / 4	16.59 ± 29.91	3.60 ± 1.80	3.74 ± 1.35
32	$0.0194 \pm 0.0019 \cdot 10^6$	519.5 / 4	41.13 ± 50.38	3.94 ± 2.39	7.97 ± 9.82

Table 3.1: Experimental properties for the object reconstruction and tracking of wild-type (cc125) cells. Here ϕ_{dens} denotes the cell density, t_{rec} / proc. the recording, t_{trk} the overall object tracking, $\varepsilon_{\text{ptri}}$ the disparity distance, ε_{sft} the residual of the plane fit.

3.2. Swimming Kinematics in the Lagrangian Frame

In Figure 3.3 we have plotted several trajectories in case of the 16 \times diluted base suspension. On the top in Figure 3.3a we have included an algae clearly swimming up and down the top and bottom of the flow chamber for long times. It is found that the trajectories among the experiments are of typical helix shape (see the inset of Figure 3.4a). On the bottom of the page in Figure 3.3c we include a trajectory circling clockwise at the surface along a typical trajectory by the inset. In the middle of both figures in Figure 3.3b a trajectory of more complex shape can be found, which the organism is frequently changing its direction. This reorientation indicates that the organisms swimming gait can severely change character for short times. In the figures along the left column of Figure 3.3 the color code indicates the velocity V of the organism. We find in the experiments all together a typical velocity of $V \sim 106.63 \pm 35.17 [\mu\text{m/s}]$ not significant depending on the cell density. Going down along the left column of Figure 3.4 it can be found that the velocity increases, from $V \sim 100 [\mu\text{m/s}]$ in the bulk to $V \sim 150 [\mu\text{m/s}]$ at surface. This increase by 50[%] is significant towards measured squeeze of the flow domain, hence could be of physical interaction with the boundary. However this increase in the motility of the organism in the boundary region is not reflected when we compute mean velocity in the two regions separate as $V \sim 107.18 \pm 34.52 [\mu\text{m/s}]$ for the bulk, and $V \sim 106.53 \pm 36.64 [\mu\text{m/s}]$ for the boundary region (excluding stuck cells), hence might be only of occasional cause. In the figures of the right column of Figure 3.3 the color code indicates the rotation rate Ω and is found at an average absolute value of $|\Omega| \sim 10.00 \pm 8.14 [\text{s}^{-1}]$. On top of the right column in Figure 3.3 we observe that the trajectory is at negative rotation rate, which indicates a left-handed chirality of the helix shape. As we go down the column the left-handedness is found to be perturbed in line with the frequency of reorientation. In the bottom of Figure 3.3 we observe another different behavior for the surface circling of the organism. It is found that as the algae is circling along the surface it flips its rotation rate positive, hence in contrast to the bulk swimming at right-handed chirality for long times. We again ask the question whether these changes in the bulk and boundary are significant. In contrast with the velocity, we find that the absolute rotation rate is $|\Omega| \sim 8.34 \pm 6.35 [\text{s}^{-1}]$ in the bulk where 67.81 \pm 3.88[%] of the algae swim at left-handed chirality, whereas in the boundary region the rotation rate increases significant to $|\Omega| \sim 12.36 \pm 9.84 [\text{s}^{-1}]$ at 54.618 \pm 1.71[%] left-handed chirality among all experiments together. We therefore find for reasons yet unexplained a significant change in signature of rotation rate as the organism is in presence of the boundary.

To further interpret the shape of the typical helix trajectories we focus on the Lagrangian dynamics of the local frame defined by the trihedron to the trajectory of the organisms as introduced in subsection 2.5.3. We use the curvature κ and torsion τ to compute the radius R and pitch P of the helix. As the curvature and torsion are very sensitive measures we first smooth their time signal on a moving average stencil of $N_{\text{stn}} = 15$ points. After smoothing we discard values of $|\tau|, \kappa > 0.2 [\mu\text{m}^{-1}]$ as blown up derivatives, physically this means we do not take into account bending radii of curvature below 1/2 body-length. In similar vane as Lee et al. [52] who studied the likewise organism P. Minimum, we have interest how the velocity of the organism relates to the shape of its trajectory. In Figure 3.4 we plot the relative probability density (RD) of the radius vs. velocity, the pitch vs. velocity, and the pitch vs. radius. In Figure 3.4a the pitch and velocity scale in a linear fashion at negative pitch, i.e. left-handed chirality. In Figure 3.4b the radius as well tends to scale in a linear fashion with the velocity, however lacks definition in extending spread. In contrast we find in Figure 3.4c that the pitch and radius collapse that peak value of $P \sim 50 [\mu\text{m}]$ and radius of $R \sim 5 [\mu\text{m}]$. This indicates that the overall shape of helices by the algae can be understood in term of elongated helices with an aspect ratio of $R/P \sim 0.1$. Therefore the Darboux vector ω that is re-orienting the trihedron almost lines up with the velocity vector \mathbf{v} of the organism.

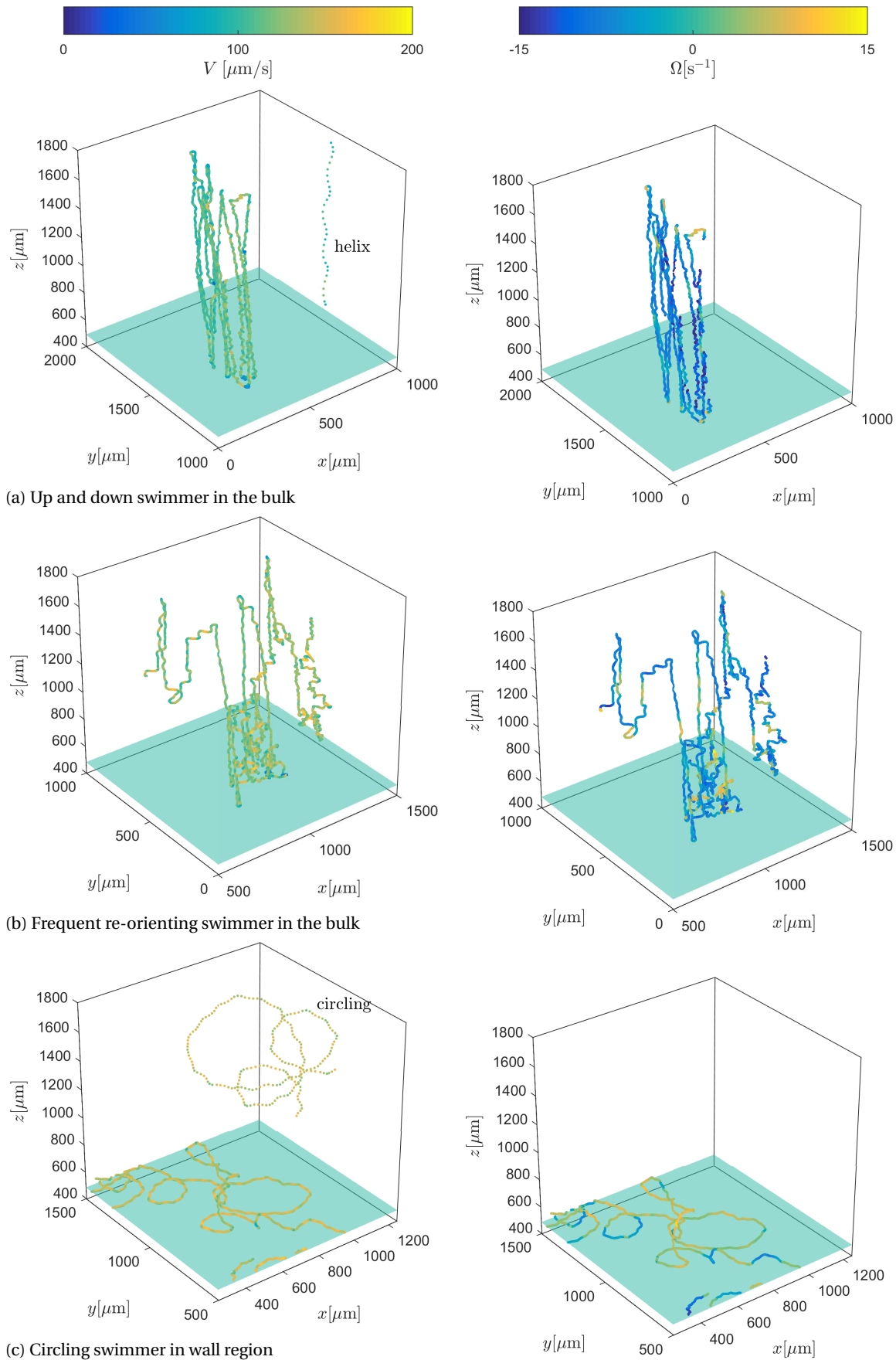


Figure 3.3: Typical trajectories that have been tracked for long times with indicate both the velocity V and rotation rate Ω in respectively the left and right column of the page. a) Typical trajectory of the up and down swimming behavior at $V \sim 100[\mu\text{m}/\text{s}]$ and $\Omega \sim -10[\text{s}^{-1}]$, i.e. left-handed chirality. b) A trajectory with frequent periods of re-orientation including velocity peaks at $V \sim 150[\mu\text{m}/\text{s}]$ and occasional flip in chirality by $\Omega \sim +10[\text{s}^{-1}]$. c) Wall-bound trajectory circling over the surface clockwise at significant higher velocity of $V \sim 150[\mu\text{m}/\text{s}]$, and flipping chirality by $\Omega \sim +10[\text{s}^{-1}]$.

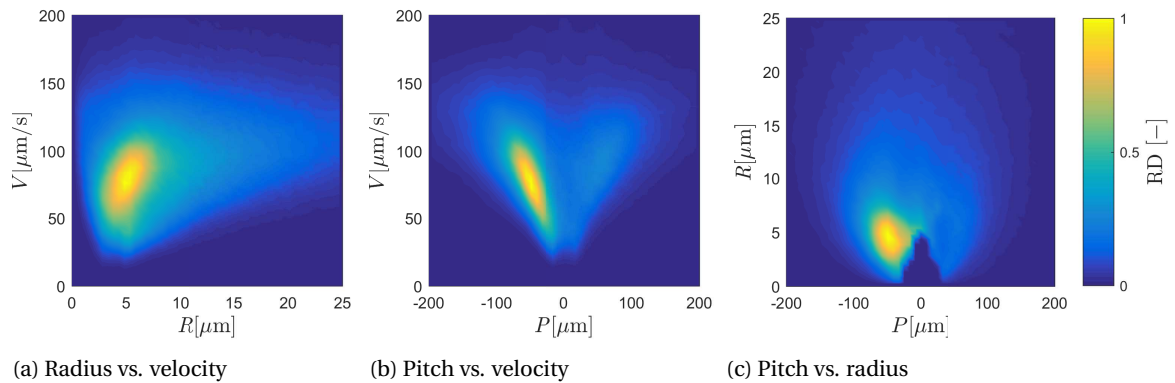


Figure 3.4: Relative probability density (RD) of helix path for the wild-type (cc125) cells. a) Velocity and radius at large spread. b) Velocity and pitch, which negative pitch indicating left-handed chirality. c) Shape of the helix in terms of radius and pitch.

3.3. Cell-Wall Interactions

We continue with the first goal of this thesis, which is to study how algae interact with physical boundaries in an unconfined geometry. We define interaction events only with the bottom boundary when the distance between the algae and boundary falls within a certain threshold length l_{trs} . We set this length to match with the observed boundary region at $l_{\text{trs}} = 100[\mu\text{m}]$, i.e. ~ 10 body lengths ($l_b \sim 10[\mu\text{m}]$) excluding the flagella ($l_f \sim 10[\mu\text{m}]$). Additionally we filter out events that did not pass this boundary with at least one body-length, this to circumvent instantaneous events as considered an threshold artifact. Once we record a event we map the trajectory in frame of the boundary, which we count a total number of $\mathcal{O}(10^4)$ events with similar behavior for all the individual experiments, therefore present as a whole. As a first approach we have focus on the orientation of the organism relative to the boundary by the incident and outgoing angles θ_i & θ_o , the minimum recorded distance l_{min} and residence time t_{res} at the surface. In this work we will not consider the detailed dynamics of the organisms as in the previous section, which yet remains beyond the scope of this work. We define the incoming and outgoing angles with respect to the physical boundary as the orientation towards the fitted plane definition using the angle between the tangent vector \mathbf{t} of the algae and the surface normal \mathbf{e}'_3 , as $\theta \equiv 90^\circ - \angle(\mathbf{t}, \mathbf{e}'_3) \in [-90^\circ, +90^\circ]$. This angular definition is a signed version of the work by Kantsler et al. [43], we smooth this signal by a first order polynomial on a stencil of $N_{\text{stn}} = 30$ frames to find the long time scale orientation of the helix path over approximately 2 periods of revolution.

In Figure 3.5 we present a series of typical results for individual trajectories of the algae that approach the boundary together with their time-series of height $z(t)$ relative to the surface, which the color code indicates the orientation of the algae towards the surface. Presented along the rows of Figure 3.5 we observe four distinct types of behavior in our experiment. On the top two rows (Figure 3.5a and Figure 3.5b) we present two cases of algae that crash into the surface and depart again, this we will refer to as reflection. On the bottom two rows (Figure 3.5c and Figure 3.5d) we find two typical examples of algae that remain at the surface, which is called wall-bound. We start to discuss Figure 3.5a in more detail. Here the algae comes in at steep angle and depart again at symmetric reflection, after having spend some residence time at the surface. During this scattering event we find that the algae come within reach of contact $l_c \sim 20[\mu\text{m}]$ with the surface indicated by the dashed red line. This region is identified to be within reach of contact by half the cell-body $l_b \sim 5[\mu\text{m}]$ plus flagella $l_f \sim 10[\mu\text{m}]$ including the accuracy of the experiment $\epsilon_{\text{exp}} \sim 5[\mu\text{m}]$, hence we refer to this regions as the contact region. As we continue to Figure 3.5b, we find another distinct type of reflection event. Here the algae comes in at a more moderate as well varying orientation, then shortly touches the surface within reach of contact, and depart the surface at much steeper orientation, as well indicated by the color code. There is large interest whether such a symmetric or steepening reflection is a universal boundary interaction, as will be studied in subsection 3.3.2. In Figure 3.5c find a typical case of co-planer clockwise circling (when viewed from above). As can be seen in time series next to the triangulated path, this organism did not escape the direct contact zone during circling as it remained co-planar. At the bottom row in Figure 3.5d, we present an example in which an considered surface bound algae escape the direct contact zone in a (quasi) periodic manner. This algae seems to perform much more complex "acrobatics" as it wobbles above the surface, we call this type of motion surface wobbling.

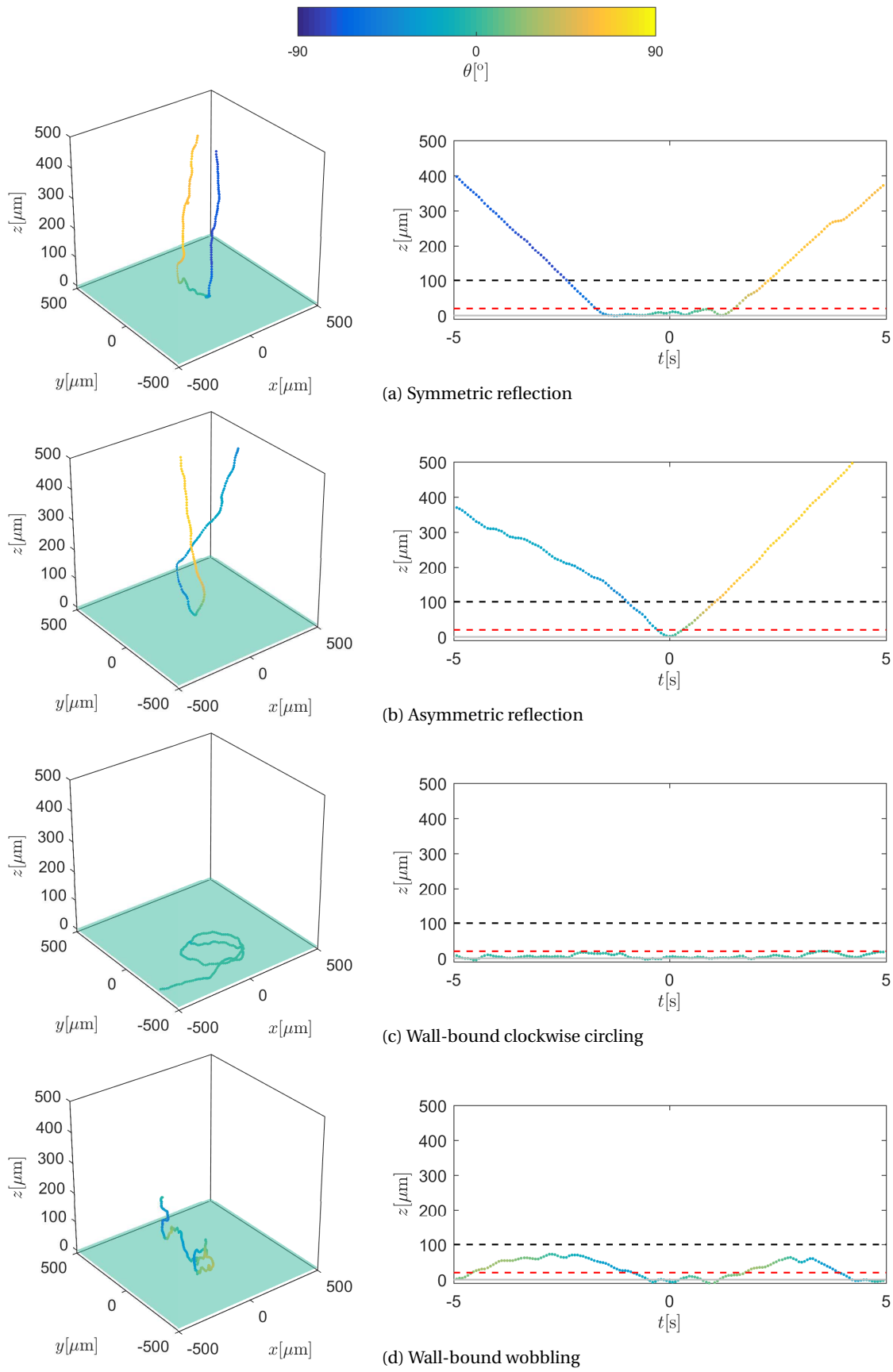


Figure 3.5: Typical surface trajectories in time span of 10 seconds as found in the $16\times$ diluted experiment. In red we denote the contact region l_c and in black the threshold length l_{trS} to define the surface region.

a clear peak at incident angle of $\theta_i \sim -70^\circ$ and outgoing angle of $\theta_o \sim +70^\circ$, with much similarity as what is observed in the flow-chamber of section 3.1. With contrast the wall-bound events in Figure 3.7a, there is in Figure 3.8a by the definition of the reflection events no overlap at the origin. In addition we find in Figure 3.8a that the incident angle is slightly more spread around $\theta_i \sim -70^\circ$, whereas the outgoing angle narrows its peak around $\theta_o \sim +70^\circ$ at departure. As before with the wall-bound cells, we find in Figure 3.8b the minimal distance falls within narrow range of contact $\sim 10[\mu\text{m}]$, rather than being distributed over the contact region up to $l_c = 20[\mu\text{m}]$. In Figure 3.8c the residence time counted for the cell that came within the contact region approach from and leaving to the bulk, peaks at a finite $t_{\text{res}} \sim 2[\text{s}]$ where-after it decays in a long tails including both our typical event of Figure 3.5a and Figure 3.5b. The peak value at $t_{\text{res}} \sim 2[\text{s}]$ indicates that the surface reflection is dominated by short touch to the surface as it takes about 2 second to approach and depart the surface.

We continue with the cells that reflected of the surface but not came within reach of contact. These event would be to high interest, as they could be of hydrodynamic origin and reveal hydrodynamic interactions. First we note that in our experiments we count much less events only within the order of hundreds $\mathcal{O}(10^2)$. This is could very well be due the majority of the cells swimming up and down the flow domain, and therefore approach the surface such that they will always impact it. In contrast with the contact region we find in Figure 3.8d that the reflection takes place spreading out from moderate angle. In Figure 3.8e the minimum length scale to the surface is found to be distributed more less uniform, hence indicating no specific region attraction. As we study the residence time in Figure 3.8f we find a significant drop below the previous surface approach and departure at $t_{\text{res}} \sim 2[\text{s}]$, this verify that most of the cells did not fully approach the surface.

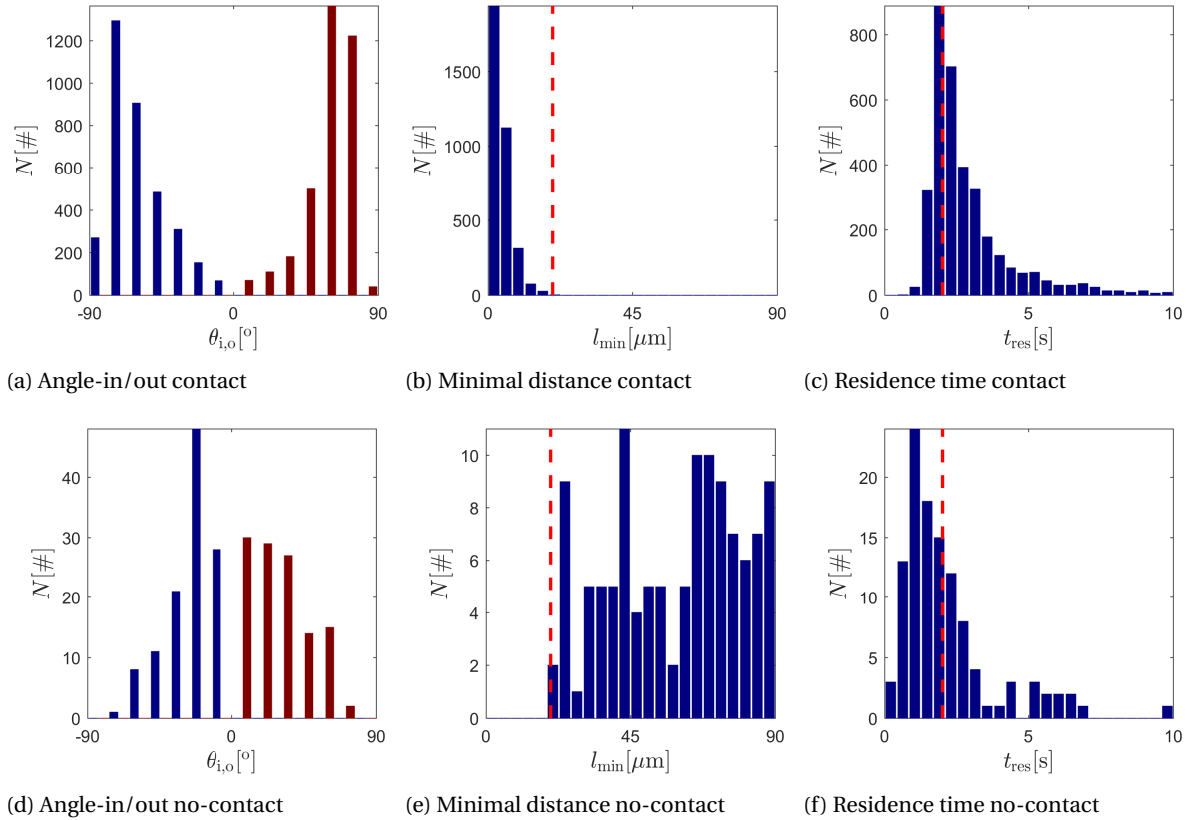


Figure 3.8: Filtered reflection events. a-c) Reflection with contact. d-f) Reflection with no contact. Along the columns of the figures grid we find from left right, the incident angle θ_i (blue) and outgoing angle θ_o (red), the minimum distance l_{min} with the contact region indicated by the red dashed line, the residence time in the surface region t_{res} with the red dashed line at 2[s].

In the typified reflection events we find much indication for a correspondence between the incidental and outgoing angle of orientation of the algae along its trajectory. We continue to study whether there would be such a mechanism of reorientation in more detail by asking whether there is a conditional relation between the incident and outgoing angle [11]. To do this we compute the conditional probability (CP) to the outgoing angle θ_o conditional to the absolute incoming angle $|\theta_i|$ denoted as $P(\theta_o | |\theta_i|)$. We do this again separately

for the contact and no-contact zone to later discuss possible discrepancies that could be of hydrodynamic origin. We start with the contact zone in Figure 3.9a, this figure should be read as: "How does the (absolute) incident angle map most likely to a outgoing one?". We find in Figure 3.9a that moderate incident angles $|\theta_i| < 45^\circ$ map to higher outgoing ones above the inset bisectrix (dashed red line) at $\theta_o \sim 50^\circ$. On the contrary we find that incident angle above $|\theta_i| > 70^\circ$ map back by a linear trend at lower θ_o . This indicates a specific boundary interaction where the outgoing orientation of the organisms mapped around $\theta_o \sim 70^\circ$. We continue to question whether there is relation between the minimal length-scale of the event and the deflection angle $\Delta\theta \equiv \theta_o - \theta_i$ as we plot the CP of $P(\Delta\theta|l_{\min})$ in Figure 3.9b. Within the contact region it can be found on the right that the most prominent re-orientation takes place within $l_{\min} \sim 10[\mu\text{m}]$, whereas less events were captured as it spread out to $l_c = 20[\mu\text{m}]$. Less prominent results are obtained for the length-scale outside the contact region $> l_c = 20[\mu\text{m}]$, since we have much less available data point. However we do find indication that in this region the reorientation mechanisms completely changes. Due less data point we increase the bin size and in Figure 3.9c find rough results that the outgoing angle has much less correlation with the (absolute) incident. More interesting is however that in Figure 3.9d the deflection angle is found to decrease with the minimal distance. This is much to of our interest, as in this region this would be due long range hydrodynamic forces.

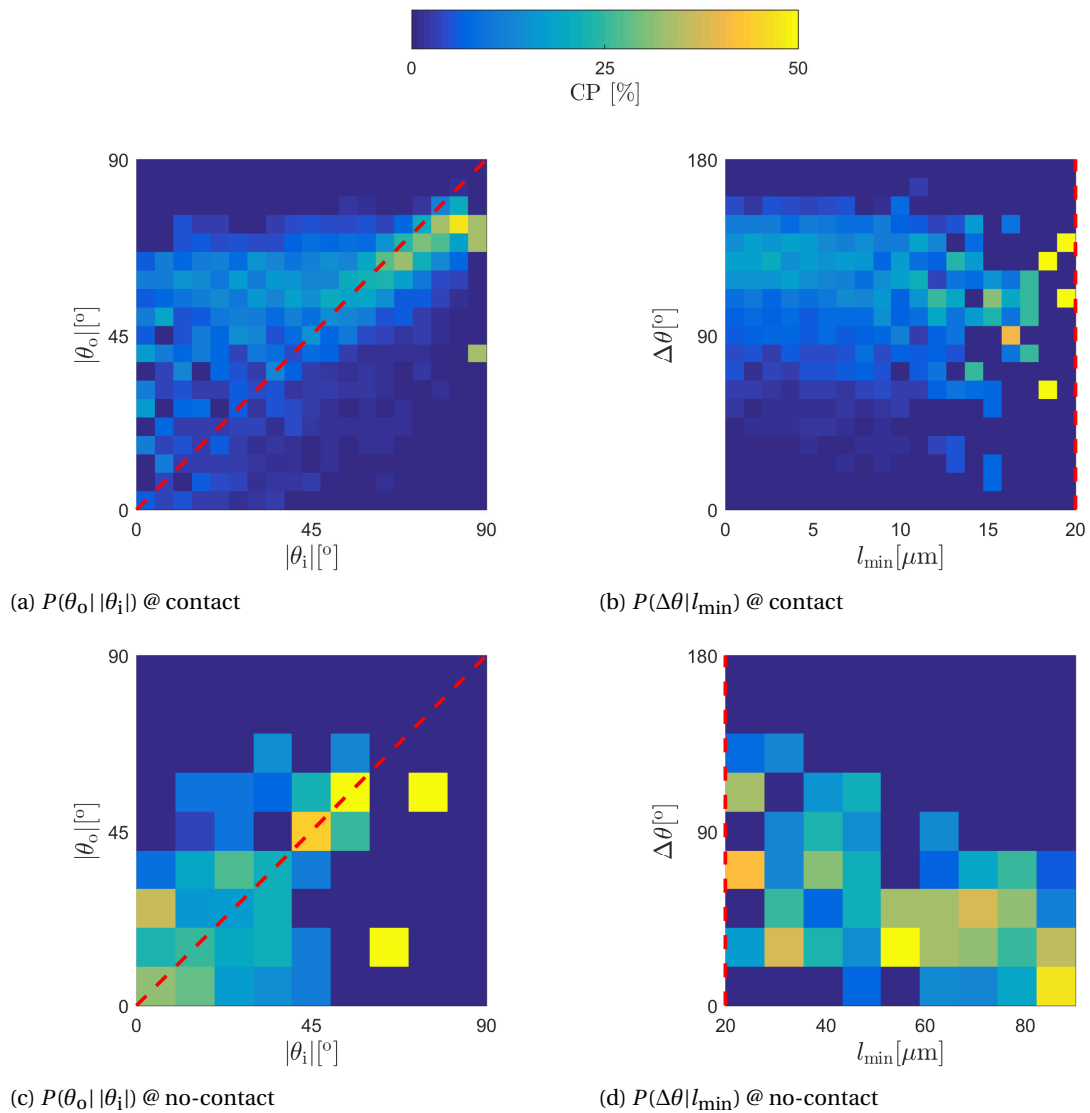


Figure 3.9: Conditional probabilities (CP) of reflection events. a) Angle-out θ_o to (absolute) angle-in $|\theta_i|$ at contact. b) Deflection $\Delta\theta$ to minimal distance l_{trS} at contact. c) With increased bin size due less data points, angle-out θ_o to (absolute) angle-in $|\theta_i|$ at no-contact. b) With increased bin size due less data points, deflection $\Delta\theta$ to minimal distance l_{trS} at no-contact.

3.4. Cell-Cell Interactions

We continue to the second objective of this thesis, which is set to study of interactions between the cells. We count cell-cell events looping over all the algae and ask which algae saw another one within relative distance between the cells below a certain threshold range l_{trs} . By this procedure it is clear that we count all events twice from either viewpoint of the individual micro-swimmer. We set the threshold as before with the cell-wall interactions to $l_{\text{trs}} \sim 100[\mu\text{m}]$ based on the boundary attraction region. This length scale lies well within a minimal mean free path of about $l_{\text{mfp}} \sim 200[\mu\text{m}]$ based on the most dense $2 \times$ diluted suspension, i.e. approximately $500[\text{cells}]$ in the flow domain of $2 \times 2 \times 1.2[\text{mm}]$. We count a overall number of event of $\mathcal{O}(10^4)$, which we limit our study only to the bulk, outside the boundary regions of the top and bottom glassware. In this section we stress that we only touch upon the complexity of the defined cell-cell events in light of the cell-wall events, where the cell-cell interactions add up to much degrees of freedom with respect to the fixed boundary as they are freely suspended in the fluid.

First we start to present 3 distinct typical cases which can be found in the first 3 rows on the page of Figure 3.11. In the figures in left column of Figure 3.11, the 3D trajectories are plotted with time as color-code to indicate the direction of swimming. In the figures in the right column of Figure 3.11 we include the relative distance corresponding to the 3D path as time series with the color-code as the relative angle of approach between the organisms. Here the relative angle between a track l and another track h is defined by their tangent vectors \mathbf{t} as $\theta \equiv \angle(\mathbf{t}^l, \mathbf{t}^h) \in [0^\circ, 180^\circ]$ as can be found in Figure 3.10.

In Figure 3.11a we find trajectories for which the algae meet each other in counter direction at $\theta \rightarrow 180^\circ$, this we will refer to as counter-swimming. We find in Figure 3.11a their trajectories only shortly touches within reach of 5 body-lengths, where after they quickly pass by. It can be seen that as the organisms comes within reach of 5 body-length, both the paths of the two organisms are found deflected, where after it departs at conserved angle. This is to much interest as it indicates some form of interaction without contact between the organisms, and apparently with no consequence to their relative orientation based on their tangent vectors. In Figure 3.11b we find a typical trajectory that crosses angle of $\theta \sim 90^\circ$, we will refer to this as cross-swimming. Again both organisms come within reach of ~ 5 body-lengths, and as well depart at conserved angle. We end with the last distinct type of interaction in Figure 3.11c. This yields a case which two organisms where more slowly approaching at moderate relative angle of $\theta \sim 20^\circ$ swimming in the same direction, this we will refer to as co-swimming. We find similar behavior which the previous discussed trajectories, whereas this case specific approaches up to $\sim 2 - 3$ body-lengths. Note that the co-swimming event they both deflect their path to the right (going down).

Introducing these three typical types of passing trajectories, we have excluded a much richer set of trajectories. Therefore, to indicate the complexity of the trajectories that come close, we have included in Figure 3.11d two trajectories that appears to be co-swimming to some extent, however in a much more complex 3D path. Here we find some form of randomization of the outgoing angle at the threshold length l_{trs} . Note that for hydrodynamic interactions such events would of large interest, asking whether these "acrobatics" would be due hydrodynamics in the farfield? In Appendix C we have included some more cell-cell events of higher complexity to give a wider impression of the diversity of events, as is encouraged to be explored.

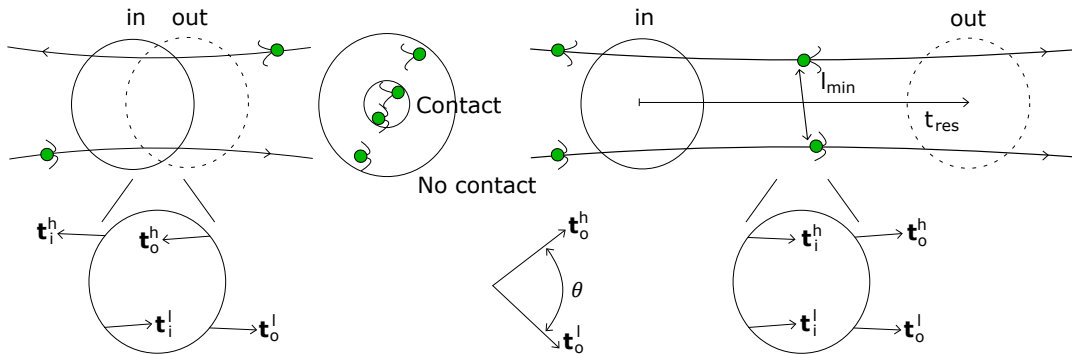


Figure 3.10: Schematics of the cell-cell events. On the left a case of counter-swimming is illustrated, and on the right a case of co-swimming. In the middle a sketch of the no-contact and contact regions are sketched, and on the bottom the angle definition of the cells with respect to each other is illustrated. l_{trs} is indicated as a circle surrounding both organisms. Note that this picture is much simplified.

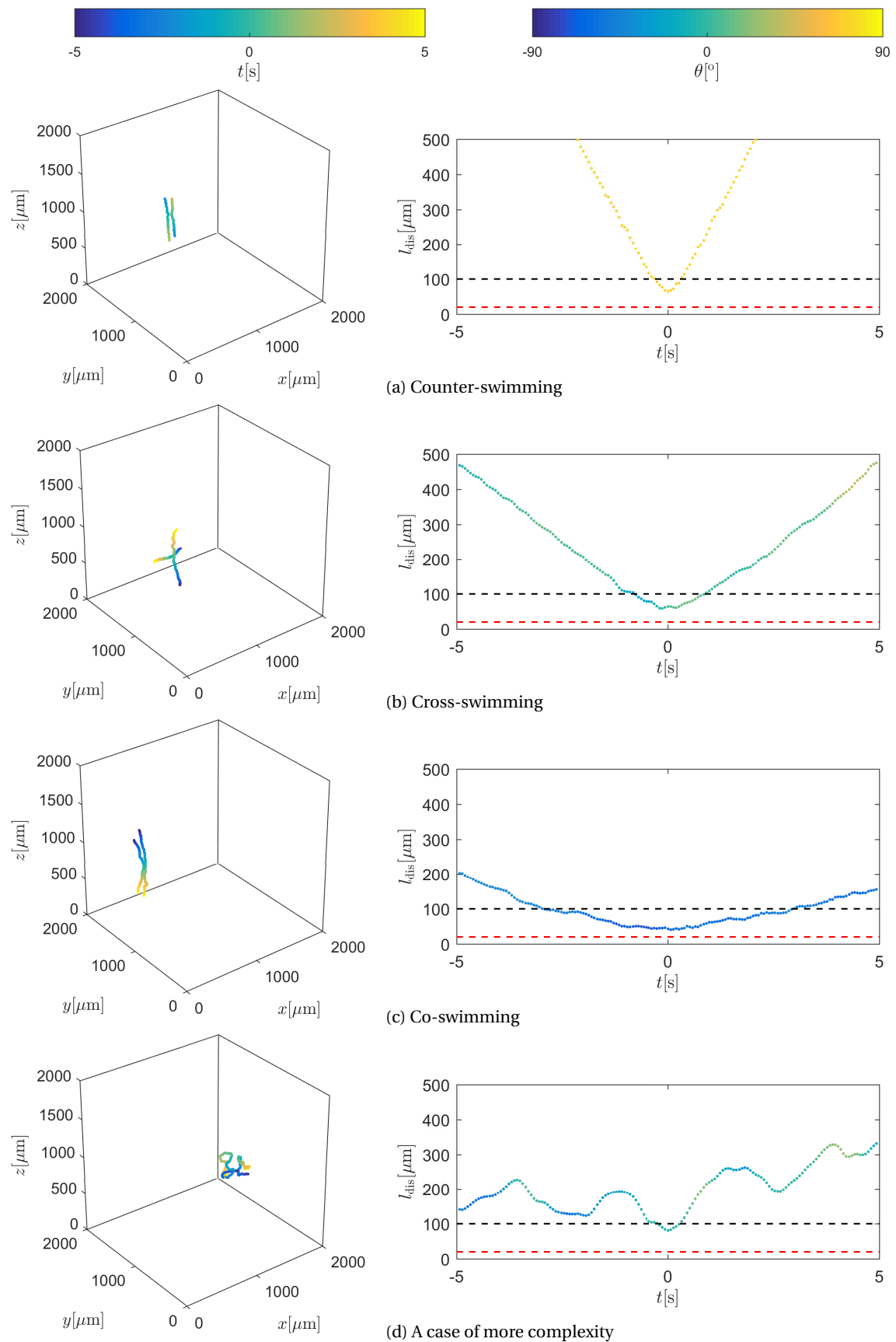


Figure 3.11: Typical cell-cell events in time span of 10 seconds as found in the $16\times$ diluted experiment. a) Counter-swimming characterized by large relative orientation $\theta \rightarrow 180^\circ$. b) Cross-swimming at $\theta \sim 90^\circ$. c) Co-swimming at moderate relative angle $\theta \rightarrow 0^\circ$. d) Complex co-directional case with synchronous behavior and quasi periodic drifting distance at the far-field. In red we denote the contact region and in black the threshold l_{trs} that define the events.

In the overall complexity of trajectories that come within reach of each other we attempt to schematize their event in Figure 3.10. We continue to use the subscript i, o for the incident and outgoing orientations between the organism respectively. In light of the cell-wall events we continue with similar definitions for the residence time t_{res} and minimal length-scale l_{min} , and record in the incident and outgoing angle at l_{trs} . Note that the schematics of Figure 3.10 do not include the dynamic evolution of the individual paths by the micro-organisms, therefore is much simplifying. This limit our access to these events as we cannot differentiate whether the event was of simple signature as in Figure 3.11a to Figure 3.11c, or of complex "acrobatic" form as in Figure 3.11d.

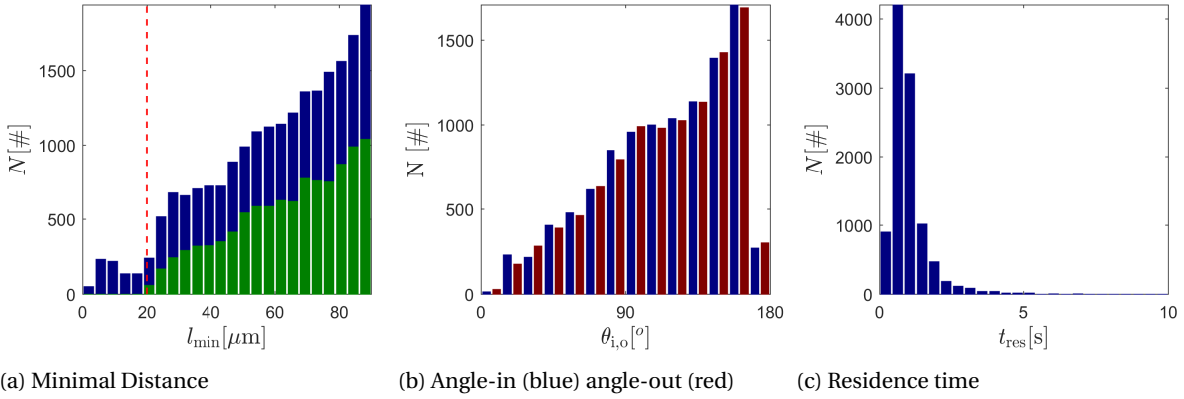


Figure 3.12: Cell-cell events. a) Histogram of the minimal distance of approach l_{min} , which only the green part is considered in the remainder as explained in the text. b) Relative angle of approach θ_i (blue) and departure θ_o (red), with linear increase up to domination by counter-swimming cells. c) Residence time t_{res} within of the events, with sharp peak at $t_{\text{res}} \sim 1[\text{s}]$.

As we study the different types of sketched behavior, we find wide range of different types of interactions, whereas in the cell-wall interaction we could already differentiate between reflecting cells and wall-bound cells. In Figure 3.12a we find, as the organisms come in reach with each other, that much less events were captured that approached within a range of contact with the cell body $l_c = 20[\mu\text{m}]$, i.e. $2 \times$ a half cell body plus flagella of either one of the organisms. When we study these events in more detail we find that they are affected by experimental artifacts presumably due long time exclusions that arise when the cells remain nearby, which the the algorithm of section 2.4 is not designed to deal with. For this reason we continue to only considered the no-contact data in our reconstruction trust worthy enough, and filter all data that remain outside the contact region. In addition we filter the trajectories that where tracked for sufficient time ($> 2[\text{s}]$) to exclude short term triangulation's, which are not revealing much information. Now we are left what is indicated by the green bars in Figure 3.12a, we find for both the blue and green bars a more-less linear trend increase at minimal separation length, outside the contact region. In the histogram of Figure 3.12b we find that there is a linear increase in event counts from co-swimming incident and outgoing orientation to counter-swimming of the organisms along their trajectories. The dominating events of counter-swimming is presumably best explained by the up and down swimming of the cells between the top and bottom glassware, which would increase the frequency of events with counter swimming cells. Note that this count not necessarily means that there less cells co-swimming. These cells could have had longer lasting events, therefore less frequently counted. As we turn to the residence times in Figure 3.12c we find that the residence times of the overall events fall mostly within the span of $t_{\text{res}} \sim 5[\text{s}]$, with a sharp peak at $t_{\text{res}} \sim 1[\text{s}]$. In case of co-swimming cells, we would expect to find long residence times, however this might be limited by the geometry of the flow-domain. Due the up and down swimming cells we would likely be limited to find cell-cell residence times within $t_{\text{res}} \sim 10[\text{s}]$ which would more less correspond with co-swimmers crossing the height of the domain.

So far we have not made any attempt to quantify how different considered variables $\theta_{i,o}$, l_{min} , t_{res} , could relate to each other. In a similar vane to the cell-wall interaction we continue to explore whether there are conditional relations between the variables, as explained and studied in the end of subsection 3.3.2 for the cell-wall events. We start with the question what typical outgoing angle θ_o we find at certain incident angles θ_i between the organisms that pass by each other. In Figure 3.13a we compute the conditional probability (CP) of $P(\theta_o|\theta_i)$. We find that the conservation of relative incident angle and outgoing one between the organisms as was found in Figure 3.11a to Figure 3.11c, is well reflected as most events follow the bisectrix indicated by the red dashed line as $\theta_o \propto \theta_i$ in Figure 3.13a. As we focus on the spread around the bisectrix we find at mod-

erate angles up to $\theta_i \sim 90^\circ$ to have some bias in spread that map higher relative outgoing angles between the organisms. This raise the question whether this would indicate a weak tendency to a divergent re-orientation as could be expected for puller type micro-swimmers [51]. However this could as well be a cause by the domain of the relative orientation angle of $\theta \in [0^\circ, 180^\circ]$, that allows no symmetric spread at moderate angles of $\theta < 90^\circ$ along the vertical direction in Figure 3.13a. At last in Figure 3.13b we do find that there is some correspondence between incident angle and residence time between the organisms, which co-swimming organisms remain longer together at moderate relative angles. This could as well explain the increase spread in Figure 3.13a as the organism could diffuse its orientation on a longer time-scale. We end to note that the conservation of angle is not necessary trivial consequence of cells ignoring each other, which such ignorance would be well illustrated by the cross-swimming cells of Figure 3.11b. As was shown in Figure 3.11a cells can deflect their paths in near reach of each other, or slowly turn in similar direction as was found Figure 3.11c, these cell not necessarily ignored each other, while they did conserve their relative orientation.

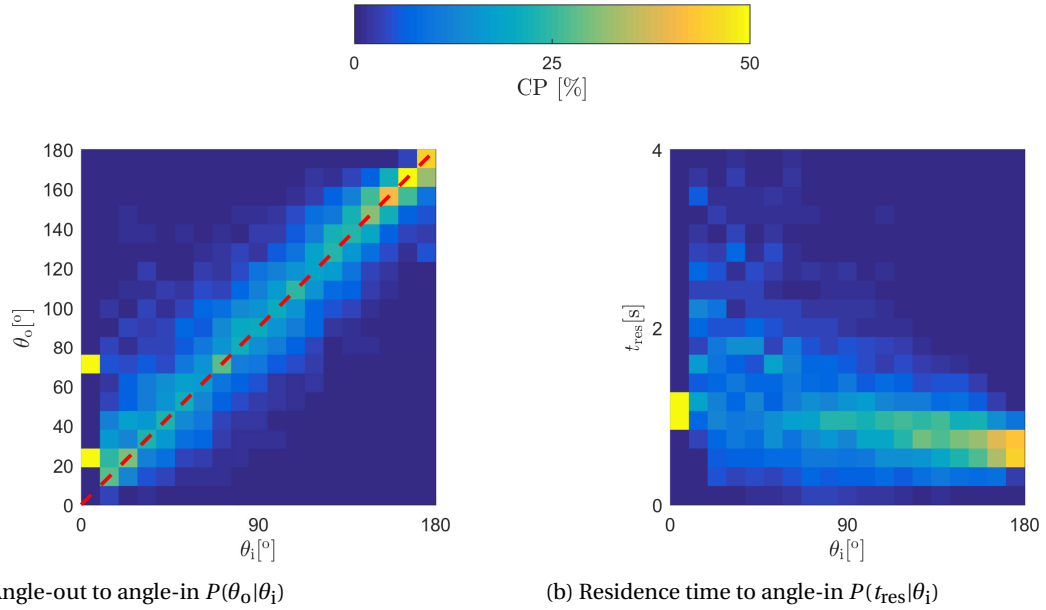


Figure 3.13: Conditional probability distribution to the no-contact zone of the cell-cell events. a) Outgoing angle to the incident angle, with overall conservation of angle $\theta_o \propto \theta_i$. b) Residence times conditional to the incoming angle showing a extended residence time at moderate incident angles $\theta_i < 90^\circ$.

4

Discussion

As was found in chapter 3, the wild-type cells unexpectedly explored the domain mostly swimming and down, whereas with the mutant cells mainly crowd the surface. This chapter continues to discuss on the physical results of chapter 3 obtained with our methods as described in chapter 2, and is structured as follows. First we will consider the dynamics of the individual micro-swimmers and discuss our results in both biological and fluid mechanics context to work by others. Second we will consider the cell-wall interactions, and compare our results in the unconfined fluid domain on similar studies done in the confined quasi 2D geometry [11, 43]. We propose that the results obtained by the cell-wall events can explain the up and down swimming in the bulk of the wild-type cells. The cell-cell interaction will only be considered shortly, since we are still in need for a better metric to study these events. We discuss our result up to the resolution of the experiment, i.e. limited to the positional information within the reconstruction uncertainty. Our discussion will only attempt to shed light on the actions of the flagella by use of work by others, as the shape of the algae is not captured in our experimental methods.

4.1. Individual Swimming Dynamics

In chapter 2 we found that the algae typically swim along helical paths, which we found three distinct types of trajectories, swimming up and down, swimming with frequent reorientation and circling at the surface. In this section we focus on the trajectories in the bulk to discuss the dynamics of the free swimming cells, as it was found that the presence of the surface influences the dynamics.

Crenshaw [16] first performed a 3 dimensional reconstruction on the motility of algae to study the mechanism of photo-taxis. In this study it was found that without significant light the algae swim in left-handed chiral helical trajectories, whereas in the presence of sufficient light it was found that the chirality changes to right-handedness. In the experiments of chapter 3 we find that $67.81 \pm 3.88\%$ of the algae swim at left-handed chirality in the bulk. In light of the work by Crenshaw [16] this would well explain that the majority of our cells do not respond to the LED illumination, whereas only a much smaller portion of the cells responds to the LED source by flipping its chirality. In addition to the long helices made by the cells that swim up and down, we as well find some trajectories to frequently reorient during their exploration of the domain. This could be due cells colliding frequent with other cells, however this we think is unlikely since we do as well observe long helices swimming up and down. A better explanation of this frequent reorientation would be found with the work by Polin et al. [69] who reported similar behavior as an eukaryotic version of the run and tumble mechanism for bacteria, that mediates periods of long runs with reorientation to explore the environment. In the work by Polin et al. [69] it was found that the algae reorient more frequent in the absence of light. As our lighting conditions are mild, this would allow some portion of the cells to be in search of light, and therefore more frequently reorienting. This would well explain the frequent reorienting behavior of some algae as we find it in line with the work by [69], however we do not continue to study this in more depth.

As reported well in the literature many microorganisms propel along helical trajectories, as we find as well for the experiments of chapter 3. In our experiments we find an overall swimming speed of $V = 106.63 \pm 35.17[\mu\text{m}/\text{s}]$ and a rotation rate of about $|\Omega| = 10.00 \pm 8.14[\text{s}^{-1}]$. This means that based on the size of the algae $l_b = 10[\mu\text{m}]$ the cell revolves and displaces 10 bodies a second. Lee et al. [52] recently studied the dynamics for the likewise dual flagellated microorganism *P. Minimum* that is a slightly larger micro-swimmer of $l_b =$

15[μm]. Our results go well in line with the work by Lee et al. [52], who found slightly slower speeds of about $V = 79.15 \pm 16.90[\mu\text{m}/\text{s}]$ and similar rotation rates of $\Omega = 7.43 \pm 3.10[\mu\text{m}/\text{s}]$. However in our results we find much more spread. This could be well explained due the tracking of many microorganisms at once, whereas Lee et al. [52] only followed a few cells for long times using a single camera imaging system. Despite the increased spread we do find clear peaks of radius at $R \sim 5[\mu\text{m}]$ and pitch $P \sim 50[\mu\text{m}]$ in our data. This would indicate that the algae swim along $2\times$ wider helical and more elongate trajectories compared to P. Minimum with radius $R = 3.61[\mu\text{m}]$ and pitch $P = 25[\mu\text{m}]$ [52], with a similar aspect ratio of the helix shape (R/P). In Figure 4.1 we have included our results on the pitch vs. velocity (Figure 4.1a) and a reprint of the work by Lee et al. [52] (Figure 4.1b) as comparison how the velocity scales with the pitch for two microorganisms. Here it is clear that we have as well contrast with the work by [52], which we find that the wild-type algae have a tendency to swim at left-handed chirality, whereas they report a equal probability of left and right handedness for P. Minimum. This might be explained as the microorganism P. minimum has no photo-receptor, which has been reported to influence chirality of the algae by Crenshaw [16] as explained at the beginning of this section.

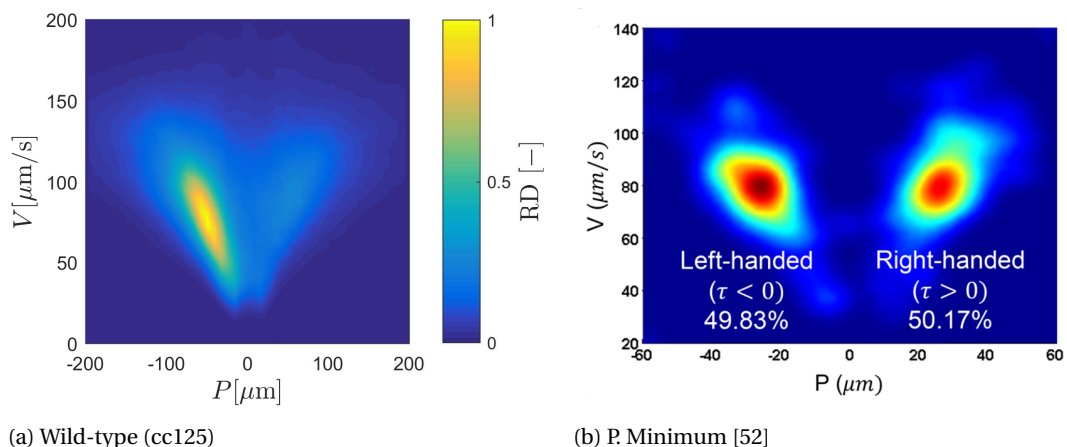


Figure 4.1: Comparison of the velocity versus pitch. a) The measured pitch and velocity for the wildtype (cc125). b) Reprint of the work by Lee et al. [52] on the likewise organism P. Minimum.

4.2. Cell-Wall Interactions

In the beginning of chapter 3 we find that the algae are distributed over a non-uniform concentration profile over the height of the domain. This concentration profile is of interest since the found increase in concentration at the boundaries of the domain indicate some form of boundary interaction. Based on the concentration profile we rationalized a characteristic length-scale of $l_{\text{bnd}} = 100[\mu\text{m}]$ over which the concentration increased towards the boundary. This overall concentration profile over the height of the domain is found to have much agreement with the work by Lee et al. [52] on the likewise microorganism P. Minimum, which the overall concentration profile as well extends up to $l_{\text{bnd}} = 100[\mu\text{m}]$. Similar cell concentration profiles have also been widely reported for spermatozoa and bacteria, and can be explained for bacteria by collision with the surface mediated by hydrodynamic forces [7, 56]. Due to the mechanical origins given to explain the surface accumulation, our results suggest that a similar mechanism is at stake for the algae.

As excluded in the previous section the dynamics of the cells were found to be perturbed by the presence of the boundary. In section 3.2 we found that our typical example of circling algae at the boundary was swimming faster, however we did not find an overall increase in the velocity, with $V \sim 107.18 \pm 34.52[\mu\text{m}/\text{s}]$ in the bulk and $V \sim 106.53 \pm 36.64[\mu\text{m}/\text{s}]$ in the surface region. On the contrary the rotation rate in the experiment increased to $|\Omega| \sim 12.36 \pm 9.84[\text{s}^{-1}]$ at the surface over $|\Omega| \sim 8.34 \pm 6.35[\text{s}^{-1}]$ in the bulk, whereas the chirality changed to almost equal division with left-handed chirality of $54.618 \pm 1.71[\%]$ over $67.8 \pm 3.88[\%]$ in the bulk. Our results in the boundary region contrast with the work by Lee et al. [52] for the likewise P. Minimum. In their work they found a mild increase in the velocity from $V \sim 79.15 \pm 16.90[\mu\text{m}/\text{s}]$ to $V \sim 85.60 \pm 14.14[\mu\text{m}/\text{s}]$, and a decrease in the rotation rate from $|\Omega| \sim 7.43 \pm 3.10[\text{s}^{-1}]$ in bulk to $|\Omega| \sim 7.46 \pm 3.17[\text{s}^{-1}]$ at the boundary, whereas they did not report any change on the chirality of the helix trajectory. Here our results for the velocity contrast with a hydrodynamic point of view, as it would be expected that the velocity near the boundary

would increase [51].

We find that the cells that remained at the surface for long times were found to circle at the surface within range of flagella contact. This circling behavior has been explained by the work of Lauga et al. [48] in terms of short range hydrodynamic forces for bacteria, due a force balance between the head and helical tail. Again due the mechanical origin of the hydrodynamic explanation [48], we could expect this to be as well responsible for the circling motion of the algae. However we did not capture the detailed action of the flagella in our experiments, hence we cannot rule out flagella contact, which as well could explain this behavior as the organism is within range of flagella contact. The flagella interaction with the boundary could as well perturb the overall chirality to $54.618 \pm 1.71\%$ and explain the increase in rotation rate as reported here. At last we found that most of the cells that remain near the boundary tend to swim co-planar to the boundary, this is in well agreement with the work by Lee et al. [52], who found the same similar behavior. We end to note that not all cells that come in contact with the boundary and remain near circle at the boundary, we found as well cells that quasi periodically touch the surface. Such complex surface interactions would interesting to further study in light of the work by [26] on the periodic waltzing of the much larger *Volvox* $l_b \sim 300[\mu\text{m}]$.

We continue to discuss the cells that approached the bottom surface of the flow domain from the bulk and left by reflection. Previous work by Kantsler et al. [43] in a quasi 2D Hele-Shaw cell of two closely packed plate at separation distance $\delta = 25[\mu\text{m}]$ showed the wildtype cells come to the boundary and can escape again, whereas the mutant cells do not escape after arrival. This would well explain why we find that the mutant (mbo-1) cell remain to crowd the surface. Here we propose that this could be due the reversed swimming stroke [43], where they mostly go to the surface due slight bottom heaviness [1], which would sink and orient the organism to the bottom boundary. For the wild-type (cc125) cells it was found by Kantsler et al. [43] that upon arrival most cells come in contact with the surface by their flagella. In the experiments presented in subsection 3.3.2 it was found that most of the algae indeed come within contact range below $l_c = 20[\mu\text{m}]$ at $10[\mu\text{m}]$. This would imply that the contact between the flagella indeed dominates as reported [43], however here we cannot differentiate whether this is direct contact or hydrodynamic lubrication with the flagella as was recently found to have different consequences by Contino et al. [11] for algae scattering of micro-pillars. In addition to the work by [43] we as well track the organisms at much longer time scales. In line with their work we find reflection events that only touch upon the surface with short duration of $\sim 0.5[\text{s}]$ when we compensate for the entrance and departure time of about $2[\text{s}]$. In contrast we find that the algae as well can spend a much wider range of residence times at the surface, as both seen in the typical examples of section 3.3 and the computed residence times of subsection 3.3.2. In case of incident and outgoing angle during the reflection event we as well find significant difference that much contrast the overall conclusions by [43]. Whereas Kantsler et al. [43] find a loss of memory of the incident angle and identifies a trapping mechanism, we find that the organism approaches and leaves the boundary at almost symmetric reflection mostly at $\theta_i \sim -70^\circ$, $\theta_o \sim +70^\circ$. As Kantsler et al. [43] find a trapping mechanism due the loss in information of the incident angle, we identify a most likely departure at $\theta_o \sim 70^\circ$, hence no trapping of the microorganism and identify a reflection mechanism. To some extend this difference can be explained by different definitions of the cell-wall event. Whereas the work by Kantsler et al. [43] focuses on the very near wall region at 2 body-lengths away from and 5 body-lengths along the boundary, our experiments zoom out to much less confined region up to atleast 10 body-lengths in all directions. This suggest that experiments by Kantsler et al. [43] could have only partially captured our definition of the wall event, as we as well report much longer residence times near the surface during reflection event. Here it remains to debate what is a better definition of a cell-wall event. On the other hand this could as well be due the confined environment of the experiments by [43], which much restricts the motion of the organism, whereas our experiments do not do this.

Additionally to the work by [43] we identify, within the definition of our events, that their is strong correspondence between the incoming and outgoing angle for the reflecting cells from the bulk. This is to much interest how cells interact with physical boundaries, as we have studied as the end of subsection 3.3.2 in form of conditional probability. For the cells that come withing contact reach to the boundary, we find that moderate absolute incoming angles are mapped at high outgoing angles. On the other hand, increased absolute incoming angles map to the outgoing angles that scale along a linear trend that crosses the bisectrix both at $|\theta_i| \& \theta_o \sim 70^\circ$. Such a trend was not found for the algae that come in range with the boundary at no contact, however so far we can only notice the discrepancy between the two as the no-contact zone had only few counts. We reprint the results at the end of subsection 3.3.2 all together for the contact and no-contact region in Figure 4.2a, and continue to discuss why this is to our interest. We propose this mechanism can well explain why the algae swim up and down in our flow domain in terms of a fixed point operation when we take into account the overall aspect ratio of the flow chamber. The overall aspect ratio of the flow chamber

is about $h/D \sim 0.1$, with h the height and D the diameter. This forces the frequency of collision with the top and bottom boundary separated at h higher than the extending sides of the domain separated at D . In term of a statistical sampling process this would yield a recursion between the top and bottom boundary as,

$$\theta^{n+1} = f_{io}(\theta^n).$$

This recursion process is sketched in Figure 4.2b. Here we typify the mapping between θ_i and θ_o by a coarse model as the green line in Figure 4.2a and Figure 4.2b as,

$$f_{io}(\theta_i) = 45^\circ + 0.33|\theta_i| \text{ with } \theta_i \in [-90^\circ, 0^\circ].$$

The details of this action at the boundary remain to debate as we do not have detailed information to the action of the flagella at the boundary. Similar approach was taken done by Contino et al. [11] for micro-algae scattering of micro-pillars of diameter $d \sim 25[\mu\text{m}]$. As we compare the conditional probability of $P(\theta_o | |\theta_i|)$ with the work of [11] we find much difference, with special care to the angle definitions. Whereas moderate collision with the pillar they report a moderate outgoing angle with less occurrence of contact, we report a steepened angle of departure, and where they report high incident angles mapping to moderate departures of $+40^\circ$, we find a reflecting events at $+70^\circ$. This discrepancy in the mechanisms of interaction with physical boundaries is highly like due the completely different geometry of the pillar and the plane physical boundary. In an engineering point of view this is interesting as there is freedom to design specific geometries to manipulate the boundary action with the cells.

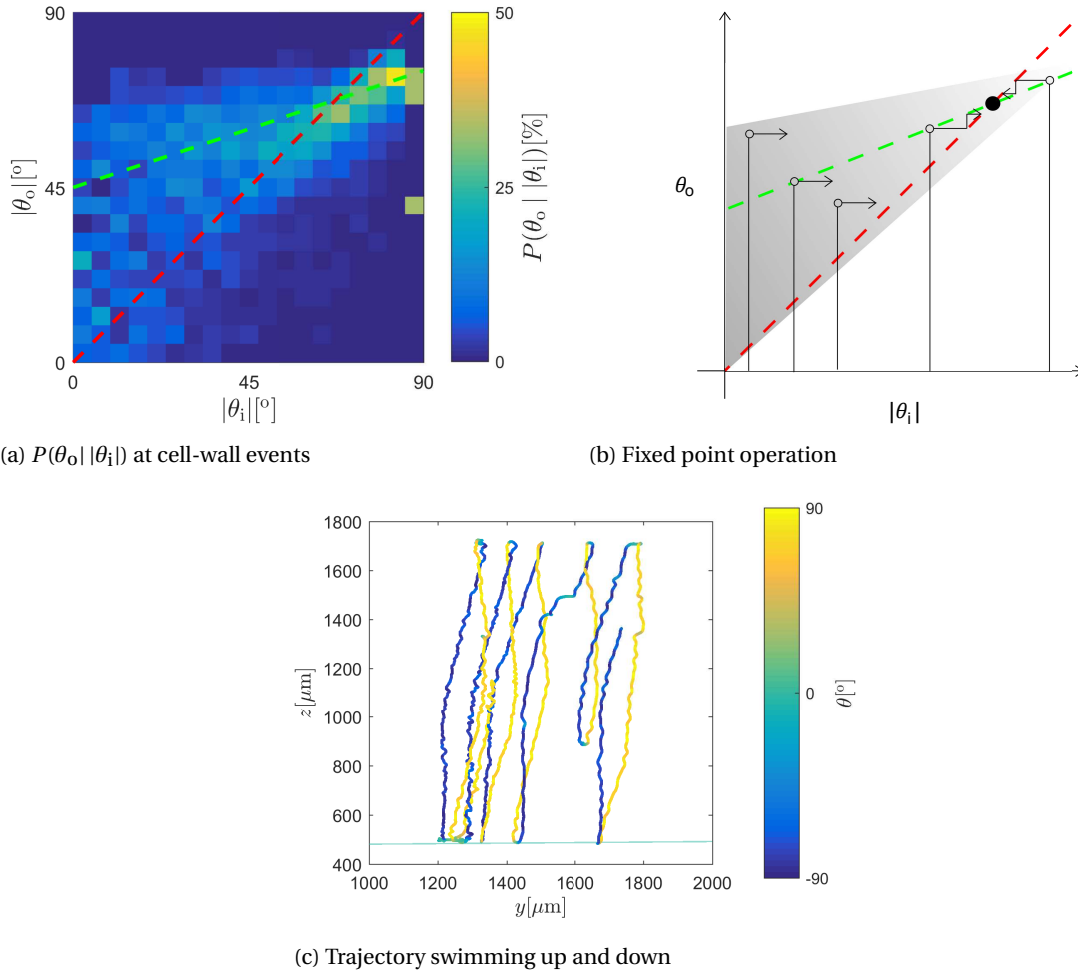


Figure 4.2: Recursion process in the flow domain geometry due the boundary action. a) The measured conditional probability distribution. b) Fixed point operation between the top and bottom glassware. c) Result of a trajectory swimming up and down between the top and bottom glassware of the fluid domain.

4.3. Cell-Cell Events

The cell-cell interactions are much more complex, since they have much more degrees of freedom than the cell-wall events as they are freely suspended in the bulk. In light of the cell-wall interaction we have only attempt to touch upon the complexity of the cell-cell events, which we continue to discuss the results of section 3.4 towards the current literature.

We start with the distinctive events that we identified at varying angle of approach. We found for the presented typical events in section 3.4 that the trajectories come within reach of about 5 body-lengths. This is interesting since the hydrodynamic domain of influence as discussed for bacteria ($l_b \sim 2[\mu\text{m}]$) extends significant over 2 body-lengths where after it decay in noise of the environment [28]. Due the mechanical origins of the hydrodynamic domain of influence, this could very well be generalized to the flow cause by algae [27], where algae might suffer less from noise in the environment due their larger size and could extend this hydrodynamic influence over 5 body-lengths. We find that as the cells come close and then depart again at conserved angle. This is not necessarily due the cells ignoring the presence of each other, as individual path are found to show some deflection either shortly at minimal separation or for longer times swimming together. Such a conservation of the angle of approach has as well been reported in the theoretical work by Pooley et al. [70] and Alexander et al. [3]. In their in plane numerical study on three-link swimmers approaching each other, it was found that this conservation of angle is due to the swimming gaits of the three-link swimmer as being a direct consequence of time reversibility between the shapes of the three-link swimmers. Despite the indication that such interactions could exist by our experiments, it be would oversimplifying to relate the shape transition of algae to the three-link swimmer, as the algae has a much more complex shape and time dependent flow field [36, 46].

Studying all the events together, we found that the cells in the bulk can come within close reach of each other up to a length scale that would allow contact between the cell bodies at $l_c = 20[\mu\text{m}]$. However we found this is much less frequent, where most cells remain within distance of no-contact with an increasing count of events at larger minimal separation. The only experimental work that has been mentioned in this thesis on the interaction of two microorganisms away from boundaries, has been carried out for two much larger Paramecia [41] in the confined geometry. Here it was reported that the Paramecia only interact in near the contact range by reorientation. However since our introduced track matching algorithm of section 2.4 has not been designed to deal with long time occlusion of the particle images in the camera plane, we had to exclude these events that were counted at contact between the cells, as these events could be affected by tracking artifacts. Therefore, unfortunately, this work cannot further discuss the near field interactions towards what was found with Paramecia [41]. Limiting the events as described in section 3.4 we did not found much indication of distinct types of events like with the cell-wall interactions. We therefore directly continued to see whether we could trace some form of conditional relations between the variables of interest. We found that indeed most cell pass each other at conserved relative angle, which at moderate incident angles the cells were found to have increased residence time. We found that at moderate angles of approach the distribution of the outgoing angles increases by some spread in the conditional probability at larger deflection. In light of the work of by Lauga and Powers [51] this deflection to larger outgoing angle could be due divergent reorientation based on the overall flow signature of the wild-type cells, which can be identified as a puller. However since at moderate angles the residence time as well increases, this could as well be due to reorientation of the organism itself on longer timescales.

Unlike with the typical events that were identified at range of angle of approach, as well a case of much more complex interaction was shown. Many complex behaviors of cell interactions (e.g. [8]) can be thought that could find unexplained mechanisms of interactions that have not been captured by our study of the experiments here. In light of the numerical work by [40] we end to note that we did find that indeed the interactions of cells with each other can be very complex.

5

Conclusions

Using the methodology of chapter 2 we have been able to reconstruct and track multiple algae in a 3 dimension fluid domain. By use of synthetic data we found that tracking algorithm as described in section 2.4 in the ideal case either marks the Pareto frontier or follows its truncation. As we evaluated the experimental reconstruction as well towards the Pareto frontier, we found results that we could rationalize to expectation based on the synthetic data. We found an overall triangulation efficiency of $\eta_{\text{rec}} \sim 0.7$ for the wild-type cells and much lower $\eta_{\text{rec}} \sim 0.5$ for the mutant cells due the high localized density at the bottom boundary.

Unexpectedly our experiments where found to be dominated by up down swimming between the top and bottom glassware in the fluid domain for the wild-type cells. Dependent on the cell density we did not find much different behavior, hence we do not report any phase change of the suspension in range of $\phi_{\text{dens}} \sim \mathcal{O}(10^3 - 10^4)$, being as well to interest beforehand the carried out experiments. As reported among many microorganisms as well as for algae [16, 18] we find in overall that the algae swim along elongated helical trajectories in the bulk, here mostly up and down the fluid domain. As well do we find that a small portion frequently reorients, which we subscribe to behavior reported by Polin et al. [69]. We found that the algae swim at likewise characteristics as their likewise organism *P. Minimum* as studied by Lee et al. [52], however with $2\times$ increase in size of their helical path. In contrast with the work by [52] we find that algae have tendency to swim at right handed chirality in the bulk, instead of equal probability as reported for *P. Minimum* [52]. This would be well explained by the work of [16, 18], which the algae in our experiments respond to the mild LED illumination.

We find similar concentration profiles over the height of the domain as reported by Lee et al. [52]. Within characteristic length-scale of this concentration profile to the boundary we find that most algae come in contact, and the algae that remain near the boundary tend to align their direction co-planar to the boundary which is as well reported for *P. Minimum* [52]. Such concentration profiles and typical behavior have as well been found among bacteria and spermatozoa, which can be explained as a consequence of hydrodynamic forces mediated by collision [7, 56]. We find unlike the results by Lee et al. [52] no significant overall increase of speed of the organism at the boundary, as could be expected from hydrodynamic theory [51]. As expected from the literature on bacteria, the algae as well swim along clockwise circles at the boundary, this has been well explained by the work of Lauga et al. [48] in terms of short range hydrodynamic forces between the head and tail of the bacteria. Here we follow this explanation, however we have no insight of the detailed action of the flagella at the boundary, therefore with the different shape of the algae the details of this similarity with bacteria as far as discussed remains unclear. As well do we find that in our experiments that the chirality was found to be influenced by the boundary at increased rotation rate of the organisms. Short range hydrodynamics forces or flagella contact could very well explain this behavior, however we have no information on the flagella and therefore we did not identify the responsible mechanism. Another type of wall interaction is found for algae that typically touch the wall in a quasi periodic manner. This could resemble some complex bound state as has been reported for larger *Volvox* near the boundaries in the unconfined geometry [26].

We turn to the cells that approach from the bulk to the boundary and departed at reflection. Kantsler et al. [43] reported that flagellar contact dominates cell-wall interactions. We extend these findings to the unconfined geometry which we measure that the majority of the cells come within close range to the boundary which we cannot rule out flagella contact. However, in light of the work by Contino et al. [11] it remains to debate whether the flagella came in direct contact or hydrodynamic lubrication, as we cannot tell from our

methodology. In continuation we find much contrasting results with the work done by Kantsler et al. [43] in the confined quasi 2D geometry. Whereas they find a trapping mechanism of the cells at close range to the boundary, we find a reflection at the boundary with extending residence times. This discrepancy can partially be explained by the difference in the definition of the event. As we capture events over a larger spatial domains and record for much long residence times, the work by Kantsler et al. [43] is limited to capture only a part of the event we describe. On the other hand, this discrepancy in results could as well be of physical cause, since the experiments of Kantsler et al. [43] were carried out in the confined geometry, hence could limit the motion of the organism. Unlike Kantsler et al. [43] we not report a loss of information of the incident angle, as we find that there is correspondence between the absolute incident angle to the outgoing one. We find that at moderate absolute incident angles the outgoing angle increases, whereas at higher absolute incident angle the outgoing angle collapses on a linear trend that crosses the bisectrix in the $|\theta_i|, \theta_o$ -plane. We find that this correspondence can well explain why the algae are mainly swimming up and down in our flow domain. We propose that due to the high aspect ratio of the flow domain the frequency of cells swimming up and down is higher and therefore the boundary interaction yields a fixed point operation at $\theta \sim \pm 70^\circ$ between the top and bottom of the flow chamber.

We end our conclusions with the cell-cell interactions, which were found to be at much higher complexity. The only experimental work that has been mentioned in this thesis, is on the interaction of two microorganisms away from boundaries has been carried out for two much larger *Paramecia* [41] in the confined geometry, which were reported to only interact in near the contact range. However here we limited our study only to the events that did not come in close contact, since our methodology does not deal with long term occlusions of the particle images in the camera plane. We find that the frequency of the events of the cells that are in counter orientation have higher occurrence, this would be best explained as our data is dominated by up and down swimming cells, which co-swimming is counted with less occurrence. Despite we still have a sufficient number of event that are co-swimming. We find that the overall conservation of relative angle of three typical results as identified in the data, is well reflected in the conditional probability distribution of relative orientation angle out to the incoming one. Such a conservation relative orientation has been reported in the theoretical literature on the in plane motion of three-link swimmers [3, 70]. However it is hard to relate the three-link model used to the algae in this experimental work, and therefore we draw no conclusions between theory and experiments. In addition we discussed that divergent reorientation as expected from hydrodynamic theory [51] and experimentally identified hydrodynamic domains of influence [27, 28] could not be identified. At this point we rather stay in line with the conclusion of the numeric work by Ishikawa et al. [41] who as mentioned that the 3D case of interacting spherical squirmers can be of high complexity, as is as well found for the algae. We conclude that we have not yet found the right metric to access the complexity of the cell-cell events in fair detail.

6

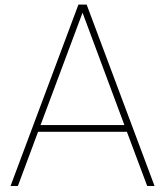
Outlook and Recommendations

The methodology developed for this thesis can be seen as a simplified version of recent work by Attanasi et al. [4], which has been to much inspiration as well to references therein. To simplify the algorithm we did not deal with occlusions during the matching of trajectories among different camera planes. This had consequence to the extent we could study the cell-cell interactions, as we unfortunately had to exclude the results that came in reach of contact due long time occlusions. Therefore it would be advisory to deal with occlusions during the matching of tracks among cameras, this could be done by additional temporal constraints and relaxation of the matching constraints [4, 96]. Another improvement could be made in the definition of the cost function. In this work we matched tracks by projecting the epipolar line using a numeric procedure similar to the triangulation of the tracked physical object. Here we could as well directly have used the residual in the triangulation of some candidate match as a trifocal distance less sensitive to ambiguities [4]. Additional, since the triangulation of the object is a continuous unknown, a mixed continuous integer optimization could further centralize the consecutive steps in our algorithm. For such problem there exist efficient methods, such as mixed integer linear programming (MILP) and quadratic programming methods (QP), and would be advisory to study further. At last during the optimization some form of time-marching could be used to predict location of objects to improve the rather simple approach of radial search around the particle images in the camera plane to define tracks.

Based on the experimental results obtained in this work, we recommend that further studies should be carried out in even more unconfined geometries that would not cause directional bias of up and down swimming due the aspect ratio of the flow-chamber. In larger fluid domains it might as well be of interest to improve the lighting conditions by laser sheet illumination, which could improve the image quality by increased contrast. For the processing of the cell-wall and cell-cell interaction, there as well remain many interesting dynamics to be explored. For example as reported on the scatter of micro-pillars [11], algae have different speed on approach and decrease velocity on departure of a micro-pillar. Such a more detailed study of the dynamics of individual organisms could as well likely be observed for boundary interaction in unconfined geometries as we studied here. Such approaches of more detail could as well shed new light on the cell-cell interactions, as we concluded to not yet have found the right metric to study these events. Next to the triangulation of the algae, it might as well be interesting to seed the flow with sufficient small tracers to reconstruct the velocity field around them by tomography, or perform tomography to exploit the detailed shape of the flagella interacting with boundaries, obstacles or even other cells.

Second we can put the boundary interaction in a more engineering question as: "How can we manipulate different flows of microorganisms depending on the boundary shape?". It would be nice to study how algae interact with convex and concave surfaces, as well as patterned surfaces and suspended obstacles in the unconfined geometry. This will presumably will shed new light on the work done in the confined geometry [11, 43], which is as well relevant to other microorganisms due the mechanical actuation [20, 23, 31, 33, 67], Such a study could have as well large impact to new insight to bio-film formation [68].

At last we have only considered a Newtonian fluid in the cell suspension, whereas many microorganisms live in a non-Newtonian environment, e.g. mucus in the stomach wall. Not much experimental work has focused on non-Newtonian fluids, which could yield many new types of behavior, whereas the literature is mainly of theoretical study [49]. Such a study could shed new light on the dynamics of the motility of microorganisms in different natural environments, here with much relevance to e.g. medical industries.



Stokesian Background Flow

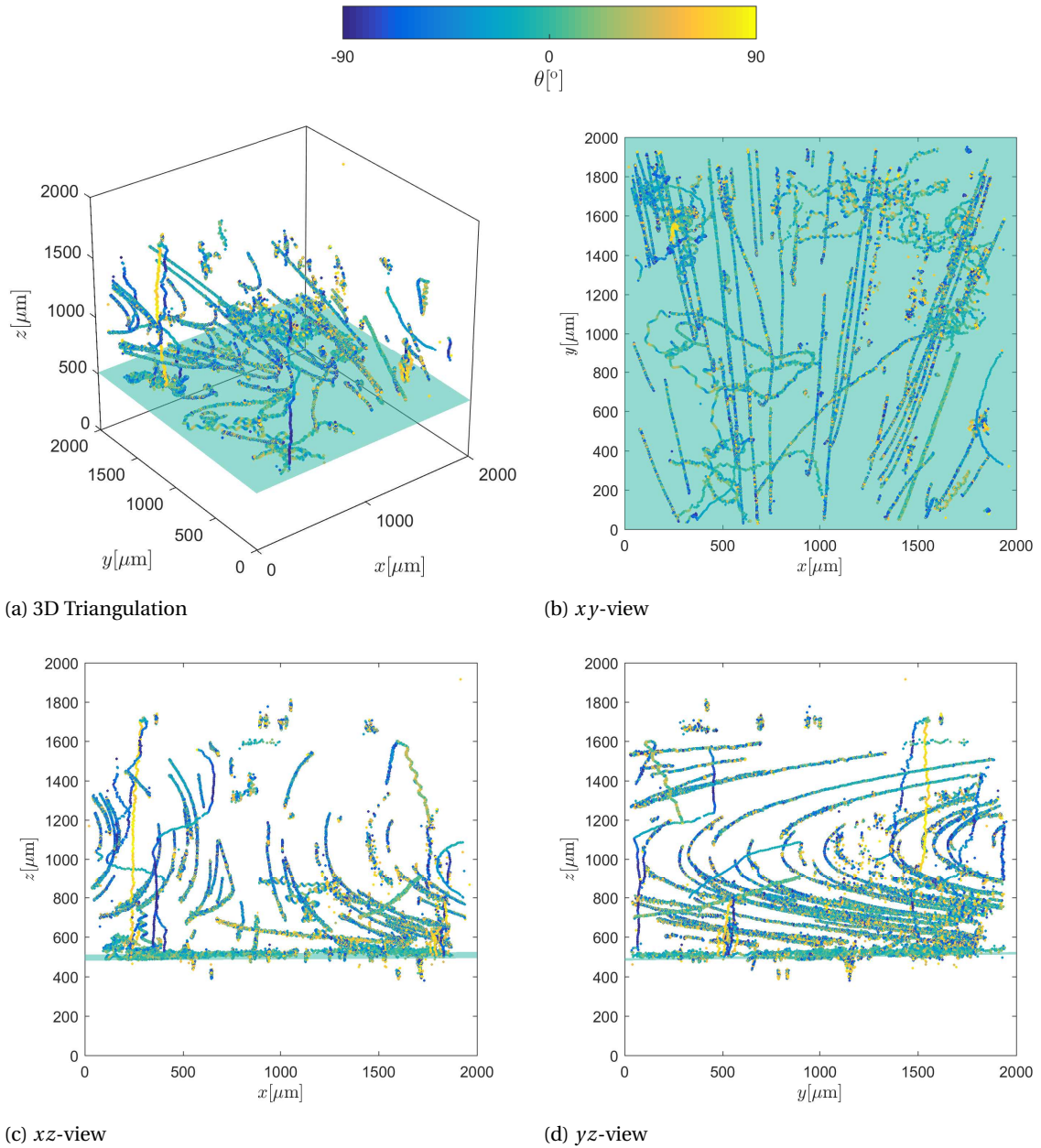


Figure A.1: Approximately 1 minute time capture of an experiment with only few active cells, we recognize a slowly creeping background flow which we qualify of Stokesian signature. As well can be seen that the reconstruction can poses artifacts like noisy triangulated particles, here in summation over 1000 frames.

B

Triangulation of the Mutant Experiments

C

Complex Cell-Cell Interactions

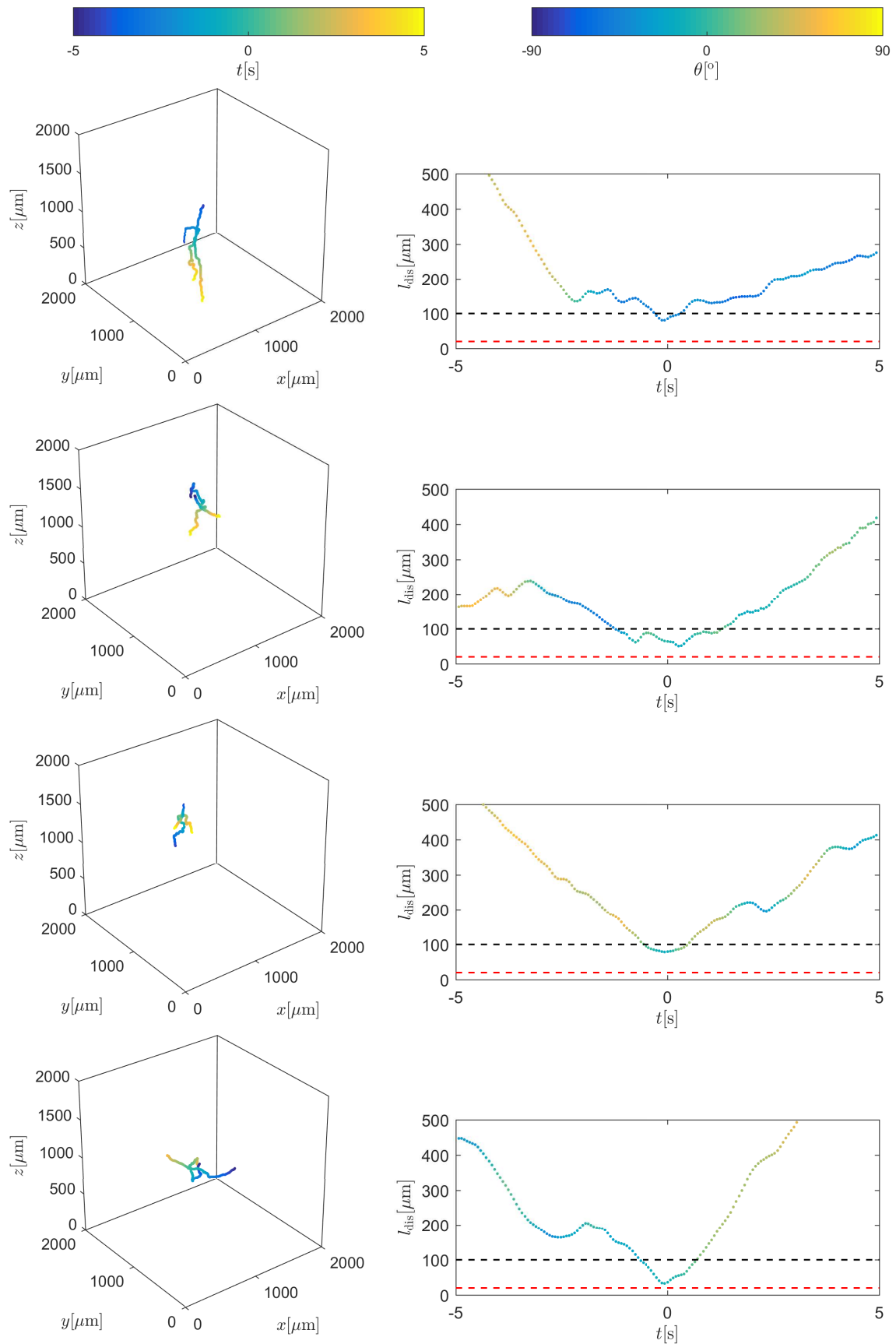


Figure C.1: Cell-cell events of higher complexity which remain to be classified and explored in future work.

Bibliography

- [1] In Elizabeth H. Harris, David B. Stern, and George B. Witman, editors, *The Chlamydomonas Sourcebook (Second Edition)*. Academic Press, London, second edition edition, 2009. ISBN 978-0-12-370873-1. doi: <http://dx.doi.org/10.1016/B978-0-12-370873-1.00059-9>.
- [2] Ronald J. Adrian and Jerry Westerweel. *Particle Image Velocimetry*. Cambridge Aerospace series. Cambridge University Press, Cambridge, New York, 2011. ISBN 978-0-521-44008-0.
- [3] G. P. Alexander, C. M. Pooley, and J. M. Yeomans. Scattering of low-Reynolds-number swimmers. *Physical Review E*, 78(4):045302, 2008. ISSN 1539-3755. doi: 10.1103/PhysRevE.78.045302.
- [4] Alessandro Attanasi, Andrea Cavagna, Lorenzo Del Castello, Irene Giardina, Asja Jelić, Stefania Melillo, Leonardo Parisi, Fabio Pellacini, Edward Shen, Edmondo Silvestri, and Massimiliano Viale. GReTA-A Novel Global and Recursive Tracking Algorithm in Three Dimensions. *IEEE Transactions on Pattern Analysis and Machine Intelligence*, 37(12):2451–2463, 2015. ISSN 01628828. doi: 10.1109/TPAMI.2015.2414427.
- [5] Shoji A. Baba, Shoko Inomata, Mayumi Ooya, Yoshihiro Mogami, and Akemi Izumi-Kurotani. Three-dimensional recording and measurement of swimming paths of micro-organisms with two synchronized monochrome cameras. *Review of Scientific Instruments*, 62(2):540–541, 1991. ISSN 10897623. doi: 10.1063/1.1142103.
- [6] Howard C. Berg. How to track bacteria. *Review of Scientific Instruments*, 42(6):868–871, 1971. ISSN 00346748. doi: 10.1063/1.1685246.
- [7] Allison P. Berke, Linda Turner, Howard C. Berg, and Eric Lauga. Hydrodynamic attraction of swimming microorganisms by surfaces. *Physical Review Letters*, 101(3):1–4, 2008. ISSN 00319007. doi: 10.1103/PhysRevLett.101.038102.
- [8] Douglas R. Brumley, Kirsty Y. Wan, Marco Polin, and Raymond E. Goldstein. Flagellar synchronization through direct hydrodynamic interactions. *eLife*, 2014(3):1–15, 2014. ISSN 2050084X. doi: 10.7554/eLife.02750.001.
- [9] Anwar Chengala, Miki Hondzo, and Jian Sheng. Microalga propels along vorticity direction in a shear flow. *Physical Review E - Statistical, Nonlinear, and Soft Matter Physics*, 87(5):1–7, 2013. ISSN 15393755. doi: 10.1103/PhysRevE.87.052704.
- [10] Fook Chiong Cheong, Chui Ching Wong, Yunfeng Gao, Mui Hoon Nai, Yidan Cui, Sungsu Park, Linda J. Kenney, and Chwee Teck Lim. Rapid, High-Throughput Tracking of Bacterial Motility in 3D via Phase-Contrast Holographic Video Microscopy. *Biophysical Journal*, 108(5):1248–1256, 2015. ISSN 15420086. doi: 10.1016/j.bpj.2015.01.018.
- [11] Matteo Contino, Enkeleida Lushi, Idan Tuval, Vasily Kantsler, and Marco Polin. Microalgae Scatter off Solid Surfaces by Hydrodynamic and Contact Forces. *Physical Review Letters*, 115(25):1–5, 2015. ISSN 10797114. doi: 10.1103/PhysRevLett.115.258102.
- [12] G. Corkidi, B. Taboada, C. D. Wood, A. Guerrero, and A. Darszon. Tracking sperm in three-dimensions. *Biochemical and Biophysical Research Communications*, 373(1):125–129, 2008. ISSN 0006291X. doi: 10.1016/j.bbrc.2008.05.189.
- [13] H C Crenshaw. Kinematics of helical motion of microorganisms capable of motion with four degrees of freedom. *Biophysical Journal*, 56(5):1029–1035, 1989. ISSN 00063495. doi: 10.1016/S0006-3495(89)82748-1.

- [14] Hugh C Crenshaw. Orientation By Helical Motion - III. Microorganisms can orient to stimuli by changing the direction of their rotational velocity. *Bulletin of Mathematical Biology*, 55(1):231–255, 1993. doi: 10.1016/S0092-8240(05)80071-0.
- [15] Hugh C. Crenshaw. Orientation by Helical Motion - I. Kinematics of the Helical Motion of Organisms With Up To Six Degrees of Freedom. *The American Naturalist*, 55(1):197–212, 1993.
- [16] Hugh C. Crenshaw. A New Look at Locomotion in Microorganisms: Rotating and Translating. *American Zoology*, 36(6):608–618, 1996. ISSN 1540-7063. doi: 10.1093/icb/36.6.608.
- [17] Hugh C. Crenshaw and Leah Edelstein-Keshet. Orientation by helical motion-II. Changing the direction of the axis of motion. *Bulletin of Mathematical Biology*, 55(1):213–230, 1993. ISSN 00928240. doi: 10.1007/BF02460303.
- [18] Hugh C Crenshaw, Charles N Ciampaglio, Matthew M C Henry, and M McHenry. Analysis of the three-dimensional trajectories of organisms: estimates of velocity, curvature and torsion from positional information. *The Journal of experimental biology*, 203(Pt 6):961–982, 2000. ISSN 0022-0949.
- [19] András Czirók, Eshel Ben-Jacob, Inon Cohen, and Tamás Vicsek. Formation of complex bacterial colonies via self-generated vortices. *Physical Review E*, 54(2):1791–1801, 1996. ISSN 1063-651X. doi: 10.1103/PhysRevE.54.1791.
- [20] P Denissenko, V Kantsler, D J Smith, and J Kirkman-Brown. Human spermatozoa migration in microchannels reveals boundary-following navigation. *Proc Natl Acad Sci U S A*, 109(21):8007–8010, 2012. ISSN 1091-6490. doi: 10.1073/pnas.1202934109.
- [21] R. Di Leonardo, L. Angelani, D. Dell’Arciprete, G. Ruocco, V. Iebba, S. Schippa, M. P. Conte, F. Mecarini, F. De Angelis, and E. Di Fabrizio. Bacterial ratchet motors. *Proceedings of the National Academy of Sciences*, 107(21):9541–9545, 2010. ISSN 0027-8424. doi: 10.1073/pnas.0910426107.
- [22] R. Di Leonardo, D. Dell’Arciprete, L. Angelani, and V. Iebba. Swimming with an image. *Physical Review Letters*, 106(3):1–4, 2011. ISSN 00319007. doi: 10.1103/PhysRevLett.106.038101.
- [23] Willow R DiLuzio, Linda Turner, Michael Mayer, Piotr Garstecki, Douglas B Weibel, Howard C Berg, and George M Whitesides. Escherichia coli swim on the right-hand side. *Nature*, 435(7046):1271–1274, 2005. ISSN 0028-0836. doi: 10.1038/nature03660.
- [24] D H Doh, D H Kim, K R Cho, Y B Cho, W J Lee, T Saga, and T Kobayashi. Development of genetic algorithm based 3D-PTV technique. *Journal of Visualization*, 5(3):243–254, 2002. ISSN 1343-8875. doi: 10.1007/BF03182332.
- [25] Knut Drescher, Kyriacos C. Leptos, and Raymond E. Goldstein. How to track protists in three dimensions. *Review of Scientific Instruments*, 80(1):1–7, 2009. ISSN 00346748. doi: 10.1063/1.3053242.
- [26] Knut Drescher, Kyriacos C. Leptos, Idan Tuval, Takuji Ishikawa, Timothy J. Pedley, and Raymond E. Goldstein. Dancing volvox: Hydrodynamic bound states of swimming algae. *Physical Review Letters*, 102(16):1–4, 2009. ISSN 00319007. doi: 10.1103/PhysRevLett.102.168101.
- [27] Knut Drescher, Raymond E. Goldstein, Nicolas Michel, Marco Polin, and Idan Tuval. Direct measurement of the flow field around swimming microorganisms. *Physical Review Letters*, 105(16):1–4, 2010. ISSN 00319007. doi: 10.1103/PhysRevLett.105.168101.
- [28] Knut Drescher, Jörn Dunkel, Luis H. Cisneros, Sujoy Ganguly, and Raymond E. Goldstein. Fluid dynamics and noise in bacterial cell – cell and cell – surface scattering. *Proceedings of the National Academy of Sciences*, 108(27):10940–10945, 2011. doi: 10.1073/pnas.1019079108/-/DCSupplemental.www.pnas.org/cgi/doi/10.1073/pnas.1019079108.
- [29] Rémi Dreyfus, Jean Baudry, Marcus L Roper, Marc Fermigier, Howard a Stone, and Jérôme Bibette. Microscopic artificial swimmers. *Nature*, 437(7060):862–865, 2005. ISSN 0028-0836. doi: 10.1038/nature04090.

- [30] Jorn Dunkel, Sebastian Heidenreich, Knut Drescher, Henricus H. Wensink, Markus Bär, and Raymond E. Goldstein. Fluid dynamics of bacterial turbulence. *Physical Review Letters*, 110(22):1–5, 2013. ISSN 00319007. doi: 10.1103/PhysRevLett.110.228102.
- [31] S Elizabeth Hulme, Willow R DiLuzio, Sergey S Shevkoplyas, Linda Turner, Michael Mayer, Howard C Berg, and George M Whitesides. Using ratchets and sorters to fractionate motile cells of *Escherichia coli* by length. *Lab on a chip*, 8(11):1888–1895, 2008. ISSN 1473-0197. doi: 10.1039/b809892a.
- [32] E.a. Gaffney, H. Gadêlha, D.J. Smith, J.R. Blake, and J.C. Kirkman-Brown. Mammalian Sperm Motility: Observation and Theory. *Annual Review of Fluid Mechanics*, 43(1):501–528, 2011. ISSN 0066-4189. doi: 10.1146/annurev-fluid-121108-145442.
- [33] Peter Galajda, Juan Keymer, Paul Chaikin, and Robert Austin. A wall of funnels concentrates swimming bacteria. *Journal of Bacteriology*, 189(23):8704–8707, 2007. ISSN 00219193. doi: 10.1128/JB.01033-07.
- [34] Y Ge, S S Cha, and J H Park. Study of particle tracking algorithms based on neural networks for stereoscopic tracking velocimetry. *Optics and Lasers in Engineering*, 44(6):623–636, 2006. ISSN 01438166. doi: 10.1016/j.optlaseng.2005.06.007.
- [35] Raymond E. Goldstein. Green Algae as Model Organisms for Biological Fluid Dynamics. *Annual Review of Fluid Mechanics*, 47(1):343–375, 2015. ISSN 0066-4189. doi: 10.1146/annurev-fluid-010313-141426.
- [36] Jeffrey S. Guasto, Karl A. Johnson, and J. P. Gollub. Oscillatory flows induced by microorganisms swimming in two dimensions. *Physical Review Letters*, 105(16):18–21, 2010. ISSN 00319007. doi: 10.1103/PhysRevLett.105.168102.
- [37] Jeffrey S. Guasto, Roberto Rusconi, and Roman Stocker. Fluid Mechanics of Planktonic Microorganisms. *Annual Review of Fluid Mechanics*, 44(1):373–400, 2012. ISSN 0066-4189. doi: 10.1146/annurev-fluid-120710-101156.
- [38] M. Heydt, A. Rosenhahn, M. Grunze, M. Pettitt, M. E. Callow, and J. A. Callow. Digital In-Line Holography as a Three-Dimensional Tool to Study Motile Marine Organisms During Their Exploration of Surfaces. *The Journal of Adhesion*, 83(5):417–430, 2007. ISSN 0021-8464. doi: 10.1080/00218460701377388.
- [39] M. Heydt, P. Divós, M. Grunze, and A. Rosenhahn. Analysis of holographic microscopy data to quantitatively investigate three-dimensional settlement dynamics of algal zoospores in the vicinity of surfaces. *European Physical Journal E*, 30(2):141–148, 2009. ISSN 12928941. doi: 10.1140/epje/i2009-10459-9.
- [40] Takuji Ishikawa and Masateru Hota. Interaction of two swimming Paramecia. *The Journal of experimental biology*, 209(Pt 22):4452–4463, 2006. ISSN 0022-0949. doi: 10.1242/jeb.02537.
- [41] Takuji Ishikawa, M. P. Simmonds, and T. J. Pedley. Hydrodynamic interaction of two swimming model micro-organisms. 568:119, 2006. ISSN 0022-1120. doi: 10.1017/S0022112006002631.
- [42] Raphaël Jeanneret, Vasily Kantsler, and Marco Polin. Entrainment dominates the interaction of microalgae with micron-sized objects. pages 1–8, 2016. ISSN 2041-1723. doi: 10.1038/ncomms12518.
- [43] V. Kantsler, J. Dunkel, M. Polin, and R. E. Goldstein. Ciliary contact interactions dominate surface scattering of swimming eukaryotes. *Proceedings of the National Academy of Sciences*, 110(4):1187–1192, 2013. ISSN 0027-8424. doi: 10.1073/pnas.1210548110.
- [44] Hyungsoo Kim, Jerry Westerweel, and Gerrit E. Elsinga. Comparison of Tomo-PIV and 3D-PTV for microfluidic flows. *Measurement Science and Technology*, 24(2):24007, 2013. ISSN 0957-0233. doi: 10.1088/0957-0233/24/2/024007.
- [45] Min Jun Kim and Kenneth S. Breuer. Microfluidic pump powered by self-organizing bacteria. *Small*, 4(1):111–118, 2008. ISSN 16136810. doi: 10.1002/smll.200700641.
- [46] Gary S. Klindt and Benjamin M. Friedrich. Flagellar swimmers oscillate between pusher- and puller-type swimming. *Physical Review E - Statistical, Nonlinear, and Soft Matter Physics*, 92(6):1–6, 2015. ISSN 15502376. doi: 10.1103/PhysRevE.92.063019.

- [47] Donald L Koch and Ganesh Subramanian. Collective Hydrodynamics of Swimming Microorganisms: Living Fluids. *Annual Review of Fluid Mechanics*, 43(1):637–659, 2011. ISSN 0066-4189. doi: 10.1146/annurev-fluid-121108-145434.
- [48] E Lauga, W R DiLuzio, G M Whitesides, and H A Stone. Swimming in circles: motion of bacteria near solid boundaries. *Biophys J*, 90(2):400–412, 2006. ISSN 0006-3495. doi: 10.1529/biophysj.105.069401.
- [49] Eric Lauga. Life at high Deborah number. *EPL (Europhysics Letters)*, 86(6):64001, 2009. ISSN 0295-5075. doi: 10.1209/0295-5075/86/64001.
- [50] Eric Lauga. Bacterial Hydrodynamics. *Annual Review of Fluid Mechanics*, 48(1):105–130, 2016. ISSN 0066-4189. doi: 10.1146/annurev-fluid-122414-034606.
- [51] Eric Lauga and Thomas R Powers. The hydrodynamics of swimming microorganisms. *Reports on Progress in Physics*, 72(9):096601, 2009. ISSN 0034-4885. doi: 10.1088/0034-4885/72/9/096601.
- [52] Sang Joon Lee, Taesik Go, and Hyeokjun Byeon. Three-dimensional swimming motility of microorganism in the near-wall region. *Experiments in Fluids*, 57(2):26, 2016. ISSN 0723-4864. doi: 10.1007/s00348-016-2113-0.
- [53] Antony Van Leewenhoek. Observations, Communicated to the Publisher by Mr. Antony van Leewenhoek, in a Dutch Letter of the 9th of Octob. 1676. Here English'd: concerning Little Animals by Him Observed in Rain-Well-Sea. and Snow Water; as Also in Water Wherein Pepper Had Lain In. *Philosophical Transactions of the Royal Society of London B*, 12:821–831, 1676. doi: 10.1098/rstl.1677.0003.
- [54] Laurence Lemelle, Jean François Paliere, Elodie Chatre, and Christophe Place. Counterclockwise circular motion of bacteria swimming at the air-liquid interface. *Journal of Bacteriology*, 192(23):6307–6308, 2010. ISSN 00219193. doi: 10.1128/JB.00397-10.
- [55] Kyriacos C. Leptos, Jeffrey S. Guasto, J. P. Gollub, Adriana I. Pesci, and Raymond E. Goldstein. Dynamics of Enhanced Tracer Diffusion in Suspensions of Swimming Eukaryotic Microorganisms. *Physical Review Letters*, 103(19):1–4, 2009. ISSN 00319007. doi: 10.1103/PhysRevLett.103.198103.
- [56] Guanglai Li, James Besson, Liana Nisimova, Daniel Munger, Panrapee Mahautmr, Jay X. Tang, Martin R. Maxey, and Yves V. Brun. Accumulation of swimming bacteria near a solid surface. *Physical Review E - Statistical, Nonlinear, and Soft Matter Physics*, 84(4):1–8, 2011. ISSN 15393755. doi: 10.1103/PhysRevE.84.041932.
- [57] James Lighthill. Flagellar hydrodynamics*. *SIAM*, 18(2):161–230, 1976. doi: 10.1137/1018040.
- [58] M. J. Lighthill. On the Squirring Motion of Nearly Spherical Deformable Bodies through Liquids at Very Small Reynolds Numbers. *Communications on Pure and Applied Mathematics*, 5(2):109–118, 1952. ISSN 00103640. doi: 10.1002/cpa.3160050201.
- [59] Ye Liu, Hui Li, and Yan Qiu Chen. Automatic tracking of a large number of moving targets in 3D. *Lecture Notes in Computer Science (including subseries Lecture Notes in Artificial Intelligence and Lecture Notes in Bioinformatics)*, 7575 LNCS(PART 4):730–742, 2012. ISSN 03029743. doi: 10.1007/978-3-642-33765-9_52.
- [60] Enkeleida Lushi, Hugo Wioland, and Raymond E Goldstein. Fluid flows created by swimming bacteria drive self-organization in confined suspensions. *Proceedings of the National Academy of Sciences of the United States of America*, 111(27):9733–9738, 2014. ISSN 1091-6490. doi: 10.1073/pnas.1405698111.
- [61] H G Maas, a Gruen, and D Papantoniou. Particle tracking velocimetry in 3-dimensional flows. 1. Photogrammetric determination of partacle coordinates. *Experiments in Fluids*, 15(2):133–146, 1993. ISSN 0723-4864. doi: 10.1007/BF00190953.
- [62] Sébastien Michelin and Eric Lauga. The long-time dynamics of two hydrodynamically-coupled swimming cells. *Bulletin of Mathematical Biology*, 72(4):973–1005, 2010. ISSN 00928240. doi: 10.1007/s11538-009-9479-6.

- [63] Mehdi Molaei and Jian Sheng. Imaging bacterial 3D motion using digital in-line holographic microscopy and correlation-based de-noising algorithm. *Optics express*, 22(26):32119–37, 2014. ISSN 1094-4087. doi: 10.1364/OE.22.032119.
- [64] Kazuo Ohmi. SOM-Based particle matching algorithm for 3D particle tracking velocimetry. *Applied Mathematics and Computation*, 205(2):890–898, 2008. ISSN 00963003. doi: 10.1016/j.amc.2008.05.101.
- [65] Nicholas T. Ouellette, Haitao Xu, and Eberhard Bodenschatz. A quantitative study of three-dimensional Lagrangian particle tracking algorithms. *Experiments in Fluids*, 40(2):301–313, 2006. ISSN 07234864. doi: 10.1007/s00348-005-0068-7.
- [66] Sanjeeb Prasad Panday, Kazuo Ohmi, and Kazuo Nose. An ant colony optimization based stereoscopic particle pairing algorithm for three-dimensional particle tracking velocimetry. *Flow Measurement and Instrumentation*, 22(1):86–95, 2011. ISSN 09555986. doi: 10.1016/j.flowmeasinst.2010.12.009.
- [67] Sungsu Park, Peter M Wolanin, Emil a Yuzbashyan, Hai Lin, Nicholas C Darnton, Jeffrey B Stock, Pascal Silberzan, and Robert Austin. Influence of topology on bacterial social interaction. *Proceedings of the National Academy of Sciences of the United States of America*, 100(24):13910–13915, 2003. ISSN 0027-8424. doi: 10.1073/pnas.1935975100.
- [68] Alexandre Persat, Carey D. Nadell, Minyoung Kevin Kim, Francois Ingremeau, Albert Siryaporn, Knut Drescher, Ned S. Wingreen, Bonnie L. Bassler, Zemer Gitai, and Howard A. Stone. The mechanical world of bacteria. *Cell*, 161(5):988–997, 2015. ISSN 10974172. doi: 10.1016/j.cell.2015.05.005.
- [69] Marco Polin, Idan Tuval, Knut Drescher, J. P. Gollub, and Raymond E. Goldstein. Chlamydomonas Swims with Two. *Science*, 325(2009):487, 2009. doi: 10.1126/science.1172667.
- [70] C. M. Pooley, G. P. Alexander, and J. M. Yeomans. Hydrodynamic interaction between two swimmers at low reynolds number. *Physical Review Letters*, 99(22):1–4, 2007. ISSN 00319007. doi: 10.1103/PhysRevLett.99.228103.
- [71] E.M. Purcell. Life at the low Reynolds number. *American Journal of Physics*, 45(3):3–11, 1976. doi: 10.1119/1.10903.
- [72] Greta Quaranta, Marie Eve Aubin-Tam, and Daniel Tam. Hydrodynamics Versus Intracellular Coupling in the Synchronization of Eukaryotic Flagella. *Physical Review Letters*, 115(23):1–5, 2015. ISSN 10797114. doi: 10.1103/PhysRevLett.115.238101.
- [73] Sriram Ramaswamy. The mechanics and statistics of active matter. *Annual Review of Condensed Matter Physics*, 1(1):323–345, 2010. ISSN 1947-5454. doi: 10.1146/annurev-conmatphys-070909-104101.
- [74] Ingmar H. Riedel, Karsten Kruse, and Jonathon Howard. A Self-Organized Vortex Array of Hydrodynamically Entrained Sperm Cells. *Science*, 309(5732):300–303, 2005. ISSN 1095-9203. doi: 10.1126/science.1110428.
- [75] Alfred Shapere and Frank Wilczek. Gauge Kinematics of Deformable Bodies. *American Journal of Physics*, 57(514):449–460, 1989. doi: 10.1119/1.15986.
- [76] Alfred Shapere and Frank Wilczek. Geometry of self-propulsion at low Reynolds number. *Journal of Fluid Mechanics*, 198:557, 1989. ISSN 0022-1120. doi: 10.1017/S002211208900025X.
- [77] Andrey Sokolov, Mario M Apodaca, Bartosz a Grzybowski, and Igor S Aranson. Swimming bacteria power microscopic gears. *Proceedings of the National Academy of Sciences of the United States of America*, 107(3):969–974, 2010. ISSN 0027-8424. doi: 10.1073/pnas.0913015107.
- [78] H A Stone, A D Stroock, and A Ajdari. ENGINEERING FLOWS IN SMALL DEVICES: Microfluidics Toward a Lab-on-a-Chip. *Annual Review of Fluid Mechanics*, 36(1):381–411, 2004. ISSN 0066-4189. doi: 10.1146/annurev.fluid.36.050802.122124.
- [79] Ting-Wei Su, Liang Xue, and Aydogan Ozcan. Re: High-throughput lensfree 3D tracking of human sperms reveals rare statistics of helical trajectories. *Proceedings of the National Academy of Sciences*, 109(40):16018–16022, 2012. ISSN 03022838. doi: 10.1073/pnas.1212506109.

- [80] Beata Sweryda-Krawiec, Halagowder Devaraj, George Jacob, and James J. Hickman. A New Interpretation of Serum Albumin Surface Passivation. *Langmuir*, 20(6):2054–2056, 2004. ISSN 07437463. doi: 10.1021/la034870g.
- [81] Daisuke Takagi, Adam B. Braunschweig, Jun Zhang, and Michael J. Shelley. Dispersion of self-propelled rods undergoing fluctuation-driven flips. *Physical Review Letters*, 110(038301):1–5, 2013. ISSN 00319007. doi: 10.1103/PhysRevLett.110.038301.
- [82] K M Taute, S Gude, S J Tans, and T S Shimizu. High-throughput 3D tracking of bacteria on a standard phase contrast microscope. *Nat Commun*, 6(May):1–9, 2015. ISSN 2041-1723. doi: 10.1038/ncomms9776.
- [83] Geoffrey Taylor. Analysis of the Swimming of Microscopic Organisms. *Proceedings of the Royal Society of London. Series A. Mathematical and Physical Sciences*, 209(1099):447–461, 1951. ISSN 1364-5021. doi: 10.1098/rspa.1951.0218.
- [84] Roland Thar, Nicholas Blackburn, and Michael Kühl. A new system for three-dimensional tracking of motile microorganisms. *Applied and Environmental Microbiology*, 66(5):2238–2242, 2000. ISSN 00992240. doi: 10.1128/AEM.66.5.2238-2242.2000.
- [85] Tamas Vicsek. A question of scale. *Nature*, 411:421, 2001. ISSN 02687615. doi: 10.1038/35078161.
- [86] Tamás Vicsek, András Czirók, Eshel Ben-Jacob, Inon Cohen, and Ofer Shochet. Novel Type of Phase Transition in a System of Self-Driven Particles. 75(6):1226–1229, 1995. doi: 10.1103/PhysRevLett.75.1226.
- [87] Margot A S Vigeant, Micheal Wagner, Lukas K. Tamm, and Roseanne M. Ford. Nanometer Distances between Swimming Bacteria and Surfaces Measured by Total Internal Reflection Aqueous Fluorescence Microscopy. *Langmuir*, 17(7):2235–2242, 2001. ISSN 07437463. doi: 10.1021/la0012539.
- [88] H. H. Wensink, J. Dunkel, S. Heidenreich, K. Drescher, R. E. Goldstein, H. Lowen, and J. M. Yeomans. Meso-scale turbulence in living fluids. *Proceedings of the National Academy of Sciences*, 109(36):14308–14313, 2012. ISSN 0027-8424. doi: 10.1073/pnas.1202032109.
- [89] Jochen Willneff and Armin Gruen. A New Spatio-Temporal Matching Algorithm For 3D-Particle Tracking Velocimetry. *The 9th of International Symposium on Transport Phenomena and Dynamics of Rotating Machinery*, pages 1–7, 2002.
- [90] Hugo Wioland, Francis G. Woodhouse, Jörn Dunkel, and Raymond E. Goldstein. Ferromagnetic and antiferromagnetic order in bacterial vortex lattices. *Arxiv*, 2016. ISSN 1745-2481. doi: 10.1038/nphys3607.
- [91] Hai Shan Wu, Qi Zhao, Danping Zou, and Yan Qiu Chen. Acquiring 3D motion trajectories of large numbers of swarming animals. *2009 IEEE 12th International Conference on Computer Vision Workshops, ICCV Workshops 2009*, pages 593–600, 2009. doi: 10.1109/ICCVW.2009.5457649.
- [92] Hai Shan Wu, Qi Zhao, Zou Danping, and Chen Yan Qiu. Automated 3D trajectory measuring of large numbers of moving particles. *OPTICS EXPRESS*, 19(8):7646–7663, 2011. ISSN 03701573.
- [93] Mingming Wu, John W. Roberts, and Mark Buckley. Three-dimensional fluorescent particle tracking at micron-scale using a single camera. *Experiments in Fluids*, 38(4):461–465, 2005. ISSN 07234864. doi: 10.1007/s00348-004-0925-9.
- [94] Mingming Wu, John W. Roberts, Sue Kim, Donald L. Koch, and Matthew P. DeLisa. Collective bacterial dynamics revealed using a three-dimensional population-scale defocused particle tracking technique. *Applied and Environmental Microbiology*, 72(7):4987–4994, 2006. ISSN 00992240. doi: 10.1128/AEM.00158-06.
- [95] Zheng Wu, Nickolay I. Hristov, Thomas H. Kunz, and Margrit Betke. Tracking-reconstruction or reconstruction-tracking? comparison of two multiple hypothesis tracking approaches to Interpret 3D Object Motion from Several Camera Views. *2009 Workshop on Motion and Video Computing, WMVC '09*, 2009. doi: 10.1109/WMVC.2009.5399245.

-
- [96] Zheng Wu, Thomas H. Kunz, and Margrit Betke. Efficient track linking methods for track graphs using network-flow and set-cover techniques. *Proceedings of the IEEE Computer Society Conference on Computer Vision and Pattern Recognition*, pages 1185–1192, 2011. ISSN 10636919. doi: 10.1109/CVPR.2011.5995515.
- [97] Zheng Wu, Nickolay I. Hristov, Tyson L. Hedrick, Thomas H. Kunz, and Margrit Betke. Tracking a large number of objects from multiple views. *2009 IEEE 12th International Conference on Computer Vision, (Iccv):1546–1553*, 2009. ISSN 1550-5499. doi: 10.1109/ICCV.2009.5459274.
- [98] Danping Zou, Qi Zhao Qi Zhao, Hai Shan Wu Hai Shan Wu, and Yan Qiu Chen Yan Qiu Chen. Reconstructing 3D motion trajectories of particle swarms by global correspondence selection. *Computer Vision, 2009 IEEE 12th International Conference on*, 1(Iccv):1578–1585, 2009. ISSN 1550-5499. doi: 10.1109/ICCV.2009.5459358.

